ABSTRACT

XIONG, MING. Investigation of Transport Phenomena in the Presence of Interfaces: Forced Convection in Composite Porous/Fluid Domains, Solidification with a Mushy Region, and Meniscus Formation in Dip Coating Processing (Under the direction of Andrey V. Kuznetsov)

Transport phenomena play an important role in many practical applications. Every time a new technology is developed, analysis of transport processes is crucial for its success. Numerical and analytical investigations of transport processes in forced convection in composite porous/fluid domains, solidification of binary alloys, and meniscus formation in dip coating process are performed. These processes include mass, momentum, and energy transport across interfaces. For forced convection in composite porous/fluid domains, the validity of single-domain approach is investigated via comparisons between the numerical and exact solutions. An analytical solution for fluid flow described by the Brinkman-Forchheimer-Darcy equation is obtained by utilizing the boundary layer approximation. Solidification of binary alloys is studied by utilizing a porous medium approach for modeling transport processes in the mushy zone. A three-phase model is developed to predict microporosity formation during this process. Solute redistribution during this process is modeled by using the Scheil and lever rules to describe solute transport at the local scale. The investigations show that initial hydrogen concentration is an important factor affecting microporosity formation. Also, some effective ways of controlling microporosity formation are suggested based on these investigations. Another process studied in this dissertation is the dip coating with liquid carbon dioxide used as a solvent. This is a new deposition technique

developed in recent years. A model accounting for evaporation during this process is obtained based on the classical free meniscus theory. Numerical results agree well with experimental data. These results show that the dry film thickness increases with the increase of evaporation rate and initial solute concentration.

INVESTIGATION OF TRANSPORT PHENOMENA IN THE PRESENCE OF INTERFACES: FORCED CONVECTION IN COMPOSITE POROUS/FLUID DOMAINS, SOLIDIFICATION WITH A MUSHY REGION, AND MENISCUS FORMATION IN DIP COATING PROCESSING

by

MING XIONG

A dissertation submitted to the Graduate Faculty of

North Carolina State University

in partial fulfillment of the

requirements for the degree of

Doctor of Philosophy

MECHANICAL ENGINEERING

Raleigh

2001

APPROVED BY:

Co-chair of Advisory Committee	Co-chair of Advisory Committee

To my parents, sister, brother

and husband

BIOGRAPHY

Ming Xiong was born in Xinjiang, P.R. China in 1974. She received the B.S. and M.S. degrees in thermal engineering from Tsinghua University, Beijing, P.R. China, in 1995 and 1998, respectively. From 1998 to 2001, she studied in the Department of Mechanical and Aerospace Engineering, North Carolina State University, Raleigh, NC.

ACKNOWLEDGEMENTS

The author is grateful to Dr. Kuznetsov, her advisor and director of her thesis, for giving her the opportunity to work in his group, for his guidance and encouragement during the years that the present research was conducted. His enthusiasm in research also inspired the author to work harder.

The author extends her appreciation to the members of her thesis committee, Dr. Robert E. White, Dr. William L. Roberts, and Dr. James C. Mulligan. Their time, patience, and help are greatly appreciated.

The author also extends her thanks to Dr. Carbonell and Brian J. Novick in the Chemical Engineering Department of North Carolina State University. Their direction and collaboration on dip coating process greatly helped the author.

Sincere thanks to her family, friends, and officemates. Their concern, encouragement, and support are greatly appreciated.

Table of Contents

LIST OF TABLES

LIST OF FIGURES

1 INTRODUCTION

Transport phenomena play a major role in many areas of science and engineering. There are a great number of practical applications that involve these processes. In this dissertation, transport phenomena in three processes, forced convection in composite porous/fluid domains, solidification of binary alloys, and meniscus formation in advanced coating processing, are investigated. A common feature of these processes is that in all three of them there is an interface across which the exchange of mass, momentum and energy takes place. Because transport phenomena across interfaces are common in many industrial applications and processes, extensive studies in this area have been performed and numerous theories have been developed. A brief review of previous research on these three processes is given below.

1.1 TRANSPORT PHENOMENA IN COMPOSITE POROUS/FLUID DOMAINS

Investigation of transport phenomena in porous media is an important subject of research because of the increasing number of applications of porous media in energy related and geophysical engineering problems [1]. There is extensive literature available in this field [1-22]. Studies in this field gradually progress towards more complex models. For small filtration velocity, a simple Darcy law gives reasonably good agreement with experiments. For large filtration velocity, inertial forces become important and the Forchheimer correction to the Darcy law must be utilized. Finally, if boundary or interfacial effects need to be

considered, the Brinkman extension of the Darcy law must be invoked. During the last decade, it became common to utilize the so-called Brinkman-Forchheimer-extended Darcy equation, which accounts for, in addition to the Darcian resistance to the flow, both the inertial (Forchheimer) and boundary (Brinkman) effects. The problem becomes even more complicated when there is an interface between a homogeneous fluid and porous medium. Beavers and Joseph [4] first investigated boundary conditions at the porous/fluid interface and numerous subsequent studies have followed their classical research [5-14]. Currently, the most commonly accepted form of the interfacial conditions is that suggested by Ochoa-Tapia and Whitaker [11, 12]. These conditions assume continuity of the filtration velocity and a jump in the shear stress at the interface. Utilizing these conditions introduces a new experimental constant which controls the magnitude of the jump in the shear stress. To avoid numerical difficulties arising from utilizing these complicated boundary conditions, the single-domain approach is widely utilized [15-22]. However, no study has been done before to investigate the validity and limitations of this approach. In this dissertation the implicit boundary conditions imposed at the porous/fluid interface by utilization of the single-domain approach are investigated.

Numerical simulations are often necessary because the more complex the model is, the more difficult it is to obtain an analytical solution. Often an analytical solution becomes possible if a number of additional physically sound approximations can be introduced. Vafai and Kim [23, 24] introduced the boundary layer approach into the field of forced convection in porous media and obtained an analytical solution for fluid flow in the interfacial region. Several studies have been performed following their work [25-27]. In this dissertation a Couette flow

in a composite duct is investigated by utilizing the boundary layer approximation. Thermal dispersion and non-Darcian effects are accounted for. Finally, the effect of thermal dispersion on forced convection in a circular duct partly filled with a saturated porous medium is investigated numerically. A numerical method of solution is required because so far it is impossible to obtain an exact solution for this complicated forced convection flow case.

1.2 TRANSPORT PHENOMENA DURING BINARY ALLOY SOLIDIFICATION

The solidification problem has received increasing interest in recent years because of its relevance to many fields, such as metallurgy, materials processing, purification of metals, crystal growth, and casting processes [28]. Considerable work has been done in this area [28-39]. The complexity of modeling this process results from the phase change that occurs in the mushy zone where the solid, liquid and gas phases coexist simutaneously. So far, the majority of models of microporosity formation describe the mushy zone as consisting of only solid and liquid phases, which means microporosity formation in the mushy zone is neglected. Microporosity formation is an important physical phenomenon during solidification and often can not be neglected. Microporosity is a common microstructural defect present in castings which considerably affects the properties of a material. Correct prediction of microporosity formation during solidification is necessary for finding ways of controlling microporosity and improving the quality of castings. This dissertation presents a three-phase model to simulate a unidirectional solidification process, which describes the

mushy zone as consisting of three phases (solid, liquid, and gas phases). The microporosity formation during solidification under different gravity conditions is investigated by utilizing this model and some valuable insight into this process is obtained. This investigation is important for the development of future processing technologies for human operations on extraterrestrial surfaces such as those on the Moon or Mars. It is also important for utilization of the microgravity environment to better understand the physics of microporosity formation. The effects of other factors, such as initial hydrogen concentration, models describing solute transport at the local scale, and solute concentration, are investigated.

1.3 TRANSPORT PHENOMENA IN DIP COATING PROCESS

Liquid coating techniques are widely used in industrial processes to deposit thin films on the surface of a wafer. Dip coating is one of the most commonly utilized deposition techniques. It is used to produce photographic films, protective or cosmetic coatings, solid reflective coatings on glass windows and many other types of coatings [40-42]. Carbon dioxide is chosen as a solvent because of its unique physical properties near the critical point, such as sensitivity to temperature and pressure variations, low viscosity, and low surface tension. Although considerable work has been done on modeling dip coating processes [43-49], there are few works on dip coating that consider evaporation, which is a crucial phenomenon in this deposition process. This dissertation extends the classical free meniscus theory to account for evaporation effects. Numerical investigations of the dip coating process with

liquid carbon dioxide as the solvent are carried out. Theoretical predictions agree well with experimental results.

REFERENCES

1. Nield, D.A. and Bejan, A., *Convection in Porous Media*, Springer-Verlag, New York Inc., 1992

2. Vafai, K. and Tien, C.L., Boundary and inertia effects on flow and heat transfer in porous media, *International Journal of Heat and Mass Transfer*, 24:195-203, 1981

3. Lage, J.L., The fundamental theory of flow through permeable media from Darcy to turbulence, *Transport Phenomena in Porous Media*, Ingham, D.B. and Pop, I., Editors, Pergamon, Oxford, pp.1-30, 1998

4. Beavers, G.S. and Joseph, D.D., Boundary condition at a naturally permeable wall, *Journal of Fluid Mechanics*, 30:197-207, 1967

5. Saffman, P., On the boundary condition at the interface of a porous medium, *Studies in Applied Mathematics*, 50:93-101 1971

6. Levy, T. and Sanchez-Palencia, E., On boundary conditions for fluid flow in porous media, *International Journal of Engineering Science*, 13(11):923-940, 1975

7. Larson, R.E. and Higdon, JJL, Microscopic flow near the surface of two-dimensional porous media - I. Axial flow, *Journal of Fluid Mechanics*, 166:449-472, 1987

8. Larson, R.E. and Higdon, JJL, Microscopic flow near the surface of two-dimensional porous media - II. Transverse flow, *Journal of Fluid Mechanics*, 178:119-136, 1987

9. Vafai, K. and Kim, S.J., Fluid mechanics of ther interface region between a porous medium and a fluid layer - an exact solution, *International Journal of Heat and Fluid Flow*, 11(3): 254-256, 1990

10. Vafai, K. and Kim, S.J., On the limitation of the Brinkman-Forchheimer-extended Darcy equation, *International Journal of Heat and Fluid Flow*, 16(1):11-15, 1995

11. Ochoa-Tapia, J.A. and Whitaker, S., Momentum transfer at the boundary between a porous medium and a homogeneous fluid - I. Theoretical development, *International Journal of Heat and Mass Transfer*, 38:2635-2646, 1995

12. Ochoa-Tapia, J.A. and Whitaker, S., Momentum transfer at the boundary between a porous medium and a homogeneous fluid - II. Comparison with experiment, *International Journal of Heat and Mass Transfer*, 38:2647-26, 1995

13. Kuznetsov, A.V., Analytical investigation of the fluid flow in the interface region between a porous medium and a clear fluid in channels partially filled with a porous medium, *Applied Scientific Research*, 56:53-67, 1996

14. Kuznetsov, A.V., Influence of the stress jump condition at the porous-medium/clear-fluid interface on a flow at a porous wall, *International Communications in Heat and Mass Transfer*, 24(3):401-410, 1997

15. W.D. Bennon and F.P. Incropera, A continuum model for momentum, heat and species transport in binary solid-liquid phase change systems - II. Application to solidification in

a rectangular cavity, *International Journal of Heat and Mass Transfer*, 30:2171-2187, 1987

16. M.C. Schneider and C. Beckermann, A numerical study of the combined effects of microsegregation, mushy zone permeability and flow, caused by volume contraction and thermosolutal convection, on macrosegregation and eutectic formation in binary alloy solidification, *International Journal of Heat and Mass Transfer*, 38:3455-3473, 1995
17. H. Yoo and R. Viskanta, Effect of anisotropic permeability on the transport process during solidification of a binary mixture, *International Journal of Heat and Mass Transfer*, 35:2335-2346, 1992
18. V.R. Voller and C. Prakash, A fixed grid numerical modeling methodology for convection-diffusion mushy region phase-change problems, *International Journal of Heat and Mass Transfer*, 30:1709-1719, 1987
19. K. Vafai and S.J. Kim, Analysis of surface enhancement by a porous substrate, *ASME Journal of Heat Transfer*, 112:700-706, 1990
20. P.C. Huang and K. Vafai, Flow and heat transfer control over an external surface using a porous block arrangement, *International Journal of Heat and Mass Transfer*, 36:4019-4032, 1993
21. S.J. Kim, C.Y. Choi, Convective heat transfer in porous and overlying fluid layers heated from below, *International Journal of Heat and Mass Transfer*, 39:319-329, 1996
22. A. Hadim, Forced convection in a porous channel with localized heat sources, *ASME Journal of Heat Transfer*, 116:465-472, 1994

23. Vafai, K. and Kim, S.J., Forced convection in a channel filled with a porous medium: an exact solution, *ASME Journal of Heat Transfer*, 111:1103-1106, 1989

24. Vafia, K. and Kim, S.J., Discussion of the paper by A. Hadim "Forced convection in a porous channel with localized heat sources", *ASME Journal of Heat Transfer*, 117:1097-1098, 1995

25. Nakayama, A., Non-Darcy Couette flow in a porous medium filled with an inelastic non-Newtonian fluid, *ASME Journal of Fluids Engineering*, 114:642-647, 1992

26. Kuznetsov, A.V., Analytical investigation of Couette flow in a composite channel partially filled with a porous medium and partially with a clear fluid, *International Journal of Heat Mass Transfer*, 41(16):2556-2560, 1998

27. Kuznetsov, A.V., Fluid mechanics and heat transfer in the interface region between a porous medium and a fluid layer: a boundary layer solution, *Journal of Porous Media*, 2:309-321, 1999

28. Viswanath, R. and Jaluria, Y., Numerical study of conjugate transient solidification in an enclosed region, *Numerical Heat Transfer, Part A*, 27:519-536, 1995

29. Poirier, D.R. and Yeum, K; Maples, AL, A thermodynamic prediction for microporosity formation in aluminum-rich Al-Cu alloys, *Metallurgical Transactions*, 18A:1979-1988, 1987

30. Bennon, W.D. and Incropera, F.P., Numerical analysis of binary solid-liquid phase change using a continuum model, *Numerical Heat Transfer*, 13:277-296, 1988

31. Voller, V.R., Brent, A.D., and Prakash, C., The modeling of heat, mass and solute transport in solidification systems, *International Journal of Heat and Mass Transfer*, 32:1719-1731, 1989

32. Ampuero, J., Hoadley, A.F.A., and Rappaz, M., Numerical and experimental study of microporosity evolution during the solidification of metallic alloys, *Modeling of Casting, Welding and Advanced Solidification Processes V*, pp. 449-454, 1991

33. Emadi, D., Gruzleski, J.E., and Toguri, J.M., The effect of Na and Sr modification on surface tension and volumetric shrinkage of A356 alloy and their influence on porosity formation, *Metallurgical Transactions*, 24B:1055-1063, 1993

34. Kuznetsov, A.V. and Vafai, K., Development and investigation of three-phase model of the mushy zone for analysis of porosity formation in solidifying castings. *International Journal of Heat and Mass Transfer*, 38: 2557-2567, 1995

35. Poirier, D.R., Phenomena related to the formation of microporosity in castings. *Modeling of Casting, Welding and Advanced Solidification Processes VIII*, pp. 837-848, 1998

36. Ganesan, S. and Poirier, D.R., Conservation of mass and momentum for the flow of interdendritic liquid during solidification, *Metallurgical Transactions, Part B*, 21:173-181, 1990

37. Ni, J. and Incropera, F.P., Extension of the continuum model for transport phenomena occurring during metal alloy solidification - I. The conservation equations, *International Journal of Heat and Mass Transfer*, 38:1271-1284, 1995

38. Ni, J. and Incropera, F.P., Extension of the continuum model for transport phenomena occurring during metal alloy solidification - II. Microscopic considerations, *International Journal of Heat and Mass Transfer*, 38:1285-1296, 1995

39. Ni, J. and Beckermann, C., A volume-averaged two-phase model for transport phenomena during solidification, *Metallurgical Transactions, Part B*, 22:349-361, 1991

40. Deryagin, B.V. and Levi, S.M., *Film Coating Theory*, London: Focal Press, 1964

41. Rosenberg, L.D. and Beiter, R.L., Impact of new technology and changing practices in the automotive coatings business, *AIChE Symposium Series on New Polymer Technology for Auto Body Exteriors*, pp. 33-36, 1989

42. Dislich, H., Thin films from the sol-gel process, In *Sol-Gel Technology for Thin Films, Fibers, Preforms, Electronics, and Special Shapes*, ed. L.C. Klein. pp. 50-79, Park Ridge, NJ: Noyes, 1988

43. Landau, L. and Levich, B., Dragging of a liquid by a moving Plate, *ACTA PHYSICOCHIMIC URSS.*, 17:42-54, 1942

44. Tallmadge, J.A. and Gutfinger, C., Entrainment of liquid films drainage, withdrawal, and removal, *Industrial and Engineering Chemistry*, 59(11):19-35, 1967

45. Tallmadge, J.A. and Lee, C.Y., Dynamic meniscus profiles in free coating III, predictions based on two dimensional flow fields, *AIChE Journal*, 20(6):1079-1086, 1974

46. Esmail, M.N. and Hummel, R.L., The effect of angle on free coating of a surface, *Chemical Engineering Science*, 34(1):125-129, 1979

47. Pendergrass, J., General analysis for free drainage of non-Newtonian films from flat plates when inertial and surface tension forces and normal stresses are negligible, *AIChE Journal*, 21(3):487-494, 1975

48. Reglat, O., Labrie, R. and Tanguy, P.A., A new free surface model for the dip coating process, *Journal of Computational Physics*, 109:238-246, 1993

49. Gellman, A.J., Lubricants and overcoats for magnetic storage media, *Current Opinion in Colloid and Interface Science*, 3:368-372, 1998

2 ON THE LIMITATIONS OF THE SINGLE-DOMAIN APPROACH FOR COMPUTATION OF CONVECTION IN COMPOSITE CHANNELS

ABSTRACT

In this chapter, comparisons between the numerical solutions for forced convective flow in composite channels, partly occupied by a homogeneous (clear) fluid and partly by a fluid saturated porous medium, and the exact solutions for the same problems are carried out. This is done to establish limitations of the single-domain approach utilized to obtain the numerical solutions. These limitations result from the assumptions that are implicitly invoked once the single-domain approach is utilized to model fluid flow in the interface region between the porous medium and a clear fluid. It is shown that the single-domain approach results in correct matching of the shear stress at the porous/fluid interface only if the adjustable coefficient in the representation for the excess stress equals to zero and also if the effective viscosity of the porous medium equals to the fluid viscosity.

2.1 INTRODUCTION

Convection in composite domains partly occupied by a homogeneous (clear) fluid and partly by a fluid saturated porous medium is a subject of permanent interest for researchers. This

interest is due to many important engineering applications relevant to this problem. Solid matrix heat exchangers, the use of porous materials for heat transfer enhancement, fault zones in geothermal systems and solidification of binary alloys are a few to mention in this respect.

The single-domain approach has recently become very popular for numerical solution of convection problems in composite channels. In this approach, a single set of governing equations is formulated in such a way that equations reduce to the correct limits in both the porous and the clear fluid regions. To obtain the correct limits, values of certain coefficients in the single-domain version of the governing equations jump when crossing the interface. Since in the single-domain approach one set of governing equations is uniformly valid in both fluid and porous regions, there is no need to explicitly utilize any boundary conditions at the porous/fluid interface, and matching of variable values is inherent in the formulation itself. Boundary conditions have to be explicitly treated only at the external boundaries of the computational domain. The single-domain approach is especially beneficial for the problems related to solidification of binary alloys. In general, during solidification of a binary alloy, the computational domain consists of three regions, namely, the solid, the two-phase (mushy) and the liquid (melt) regions. In solidification problems positions of the solid/mushy and the mushy/liquid interfaces are not fixed, the interfaces move with time and their geometrical shape changes. If the single-domain approach is utilized to obtain a numerical solution of the solidification problem, there is no need to track explicitly the geometrical shape of the three regions as well as positions of the solid/mushy and the mushy/liquid interfaces.

The single-domain approach was successfully utilized in Beckermann and Viskanta [1], Bennon and Incropera [2], Schneider and Beckermann [3], Yoo and Viskanta [4], Voller and Prakash [5], Vafai and Kim [6], Huang and Vafai [7], Kim and Choi [8], Hadim [9], and in many other papers. Because of the popularity of the single-domain approach, it is important to analyze what boundary conditions are implicitly imposed at the porous/fluid interface when this approach is utilized. To analyze this problem, we will compare numerical solutions of three test problems obtained utilizing the single-domain approach with exact analytical solutions of the same problems.

Obtaining an analytical solution requires explicit imposing of boundary conditions at the porous/fluid interface. The problem of boundary conditions at the interface was analyzed in Ochoa-Tapia and Whitaker [10, 11]. In these papers, Ochoa-Tapia and Whitaker, by means of complicated volume averaging analysis of the momentum equations in the interface region, have shown that matching the Brinkman-Darcy and Stokes equation retains continuity of velocity, but produces a jump in the shear stress.

The schematic of the problem considered in this investigation is displayed in Fig. 1. Hydrodynamically fully developed flow in a composite channel whose central part is filled with a homogeneous (clear) fluid and whose peripheral part is filled with a fluid saturated porous medium is considered. Because of the symmetry of the problem only half of the channel is displayed in Fig. 1. Numerical and analytical solutions are compared for three different geometrical configurations of the composite channel: 1) Parallel-plate channel, porous layers of uniform porosity are attached to the walls of the channel; 2) Parallel-plate channel, porous layers of variable porosity are attached to the walls of the channel; 3)

Axisymmetric channel, a cylindrical porous layer of uniform porosity is attached to the wall of the channel.

Figure 1 Schematic diagram of the problem

2.2 PARALLEL-PLATE CHANNEL PARTLY FILLED WITH A POROUS MEDIUM OF UNIFORM POROSITY

2.2.1 Exact Solution

The equations governing the fluid flow in this case take the following form:

$$-\frac{d\tilde{p}}{d\tilde{x}} + \mu \frac{d^2\tilde{u}_f}{d\tilde{y}^2} = 0 \qquad 0 \le \tilde{y} \le s \qquad (1)$$

$$-\frac{d\tilde{p}}{d\tilde{x}} + \mu_{eff} \frac{d^2\tilde{u}_f}{d\tilde{y}^2} - \frac{\mu_f}{K}\tilde{u}_f = 0 \qquad s \le \tilde{y} \le H \qquad (2)$$

where H is half the distance between the plates, K is the permeability of the porous medium, $\tilde{p}$ is the pressure, s is half the thickness of the clear fluid region, $\tilde{u}_f$ is the filtration (seepage) velocity, $\tilde{x}$ is the streamwise coordinate, $\tilde{y}$ is the transverse coordinate, μ_f is the fluid viscosity, μ_{eff} is the effective viscosity in the Brinkman term for the porous region. Equation (1) describes the fully developed flow in the clear fluid region while Eq. (2) describes the fully developed fluid flow in the porous region. The third term in Eq. (2) is the traditional Darcy term while the second term is the so-called Brinkman term which accounts for viscous forces and makes it possible to impose the no-slip boundary condition at the solid wall. The effective viscosity in the Brinkman term, μ_{eff}, is in general distinct from the fluid viscosity, μ_f.

Eqs. (1) and (2) must be solved subject to the following boundary conditions:

$$\left.\frac{\partial \tilde{u}_f}{\partial \tilde{y}}\right|_{\tilde{y}=0} = 0 \tag{3}$$

$$\tilde{u}\big|_{\tilde{y}=s-0} = \tilde{u}\big|_{\tilde{y}=s+0} \tag{4}$$

$$\mu_{eff}\left.\frac{\partial \tilde{u}_f}{\partial \tilde{y}}\right|_{\tilde{y}=s+0} - \mu_f \left.\frac{\partial \tilde{u}_f}{\partial \tilde{y}}\right|_{\tilde{y}=s-0} = \beta \frac{\mu_f}{K^{1/2}} \tilde{u}_f\big|_{\tilde{y}=s} \tag{5}$$

where β is dimensionless adjustable coefficient in the representation for the excess stress at the interface,

$$\tilde{u}_f\big|_{\tilde{y}=H} = 0 \tag{6}$$

Eqs. (4) and (5) present boundary conditions suggested in [10, 11]: Eq. (4) presents continuity of the filtration velocity, and Eq. (5) presents a jump condition for the shear stress at the porous/fluid interface. Continuity of the filtration velocity at the interface was utilized in many works on porous media. Probably the best physical interpretation of this condition is given in Nield [12]. Nield [12] considered the interface of the porous medium that contains both pores and solid particles. In the pores, the fluid velocity in the porous medium matches with the fluid velocity outside the medium. Over the solid portion of the interface, the velocity is zero both in the medium (no motion in the solid phase) and in the neighboring clear fluid (because of the no-slip condition). The average velocity in the porous medium thus matches with the average velocity in the neighboring fluid. Nield [12] also provides a good physical explanation of the jump condition for the shear stress at the porous/fluid interface. According to Nield [12], over the pore section of the interface, the velocity shear is continuous, however, this is not the case over the solid section. In the solid the velocity shear is identically zero, but in the adjacent clear fluid it can have some nonzero value. Therefore, the averaged velocity shears do not necessarily match at the interface.

Though Eqs. (4) and (5) were obtained in [10, 11] by a strict volume averaging procedure, they include an adjustable coefficient in the representation for the excess stress at the interface, β, whose value must be determined experimentally. Physically, coefficient β accounts for the possible nonzero value of the velocity shear in the clear fluid adjacent to the solid portion of the interface. Estimations carried out in [10,11] have shown that $-1 \le \beta \le 1$. The boundary conditions at the interface in the form given by Eqs. (4) and (5) were utilized in [13, 14].

Since there are no reliable experimental estimates of the coefficient β for different porous media, many papers utilize direct matching of the shear stress at the interface instead of the jump condition given by Eq. (5). If we use $\beta=0$ in Eq. (5), this equation takes the following form:

$$\mu_{eff} \left.\frac{\partial \tilde{u}_f}{\partial \tilde{y}}\right|_{\tilde{y}=s+0} = \mu_f \left.\frac{\partial \tilde{u}_f}{\partial \tilde{y}}\right|_{\tilde{y}=s-0} \qquad (7)$$

which implies that the shear stress is continuous at the interface. Equation (7) was utilized, for example, in Poulikakos and Kazmierczak [15] and in Vafai and Kim [16]. Probably for many practical situations it gives a reasonable compromise which can be used until reliable experimental data for estimation of the value of the coefficient β are available. However, as it is shown in [11], for some porous media using $\beta=0$ results in very large disagreement with experimental data, and using the jump in the shear stress condition given by Eq. (5) is really necessary.

Following [13], the exact solution of Eqs. (1)-(2) along with boundary conditions given by Eqs. (3)-(6) can be presented in the following dimensionless form:

$$u = u_i + \frac{1}{2}(S^2 - y^2) \qquad 0 \le y \le S \qquad (8)$$

$$u = C\exp(-\frac{1-y}{\gamma\sqrt{Da}}) + D\exp(\frac{1-y}{\gamma\sqrt{Da}}) + Da \qquad S \le y \le 1 \qquad (9)$$

where the dimensionless velocity at the porous/fluid interface is given by the following equation:

$$u_i = \frac{-2\mathrm{Da}\gamma - (-S\sqrt{\mathrm{Da}} + \beta\,\mathrm{Da})[\exp(\sigma) - \exp(-\sigma)]}{(\gamma+\beta)\exp(\sigma) + (\gamma-\beta)\exp(-\sigma)} + \mathrm{Da} \tag{10}$$

and integration constants in Eqs. (8) and (9) are given by the following equation:

$$C = \frac{-\mathrm{Da}(\gamma+\beta)\exp(\sigma) + (-S\sqrt{\mathrm{Da}} + \beta\,\mathrm{Da})}{(\gamma+\beta)\exp(\sigma) + (\gamma-\beta)\exp(-\sigma)} \tag{11}$$

$$D = -\frac{\mathrm{Da}(\gamma-\beta)\exp(-\sigma) + (-S\sqrt{\mathrm{Da}} + \beta\,\mathrm{Da})}{(\gamma+\beta)\exp(\sigma) + (\gamma-\beta)\exp(-\sigma)} \tag{12}$$

where

$$\sigma = \frac{1-S}{\gamma\sqrt{\mathrm{Da}}} \tag{13}$$

The dimensionless parameters and variables in Eqs. (8)-(13) are defined as follows:

$$\mathrm{Da} = \frac{K}{H^2}, \qquad u = \frac{\tilde{u}_f \mu_f}{GH^2}, \qquad y = \frac{\tilde{y}}{H}, \qquad S = \frac{s}{H}, \qquad \gamma = \left[\frac{\mu_{\mathrm{eff}}}{\mu_f}\right]^{1/2} \tag{14}$$

where

$$G = -\frac{d\tilde{p}}{d\tilde{x}} \tag{15}$$

is the applied pressure gradient.

2.2.2 Numerical Solution

For the single-domain numerical solution, Eqs. (1) and (2) are combined into one equation which is valid in both porous and clear fluid regions:

$$-\frac{d\tilde{p}}{d\tilde{x}} + \Psi_1 \grave{\imath}_f \frac{d^2\tilde{u}_f}{d\tilde{y}^2} - \Psi_2 \frac{\mu_f}{K}\tilde{u}_f = 0 \qquad 0 \le \tilde{y} \le H \qquad (16)$$

where

$$\Psi_1 = 1, \qquad \Psi_2 = 0 \qquad 0 \le \tilde{y} \le s \qquad (17)$$

$$\Psi_1 = \mu_{eff}/\mu_f, \ \Psi_2 = 1 \qquad s \le \tilde{y} \le H \qquad (18)$$

No boundary conditions at $\tilde{y} = s$ are required for the numerical solution of Eq. (16). Boundary conditions are required only at the external boundaries of the computational domain, that is at $\tilde{y} = 0$ and $\tilde{y} = H$. These boundary conditions are given by Eqs. (3) and (6), respectively.

2.2.3 Comparison Between Exact and Numerical Solutions

Figure 2a presents the comparison between the exact and numerical solutions computed for Da=0.01, S=0.5 and β=0 for three different values of the coefficient γ while Fig. 2b presents the comparison between the exact and numerical computed for Da=0.01, S=0.5 and γ=1 for three different values of the coefficient β. The curves depicting the exact solution for the case β=0 and γ=1 do not have a kink at the interface, at y=0.5. For any other value of β and γ the "exact" curves have a kink. This kink in the velocity distribution at the interface occurs

because if $\beta \neq 0$ or $\gamma \neq 1$, then, according to Eq. (5), $\left.\frac{\partial \tilde{u}_f}{\partial \tilde{y}}\right|_{\tilde{y}=s+0} \neq \left.\frac{\partial \tilde{u}_f}{\partial \tilde{y}}\right|_{\tilde{y}=s-0}$, that is the derivative of velocity is not continuous at the interface. This kink is not very well visible in Fig. 2b in the curve which depicts the exact solution for β=0.5. This is because the kink for this case is small. However, if the interface region is shown on a magnified scale (Fig. 3), the presence of the kink in this curve is very well visible.

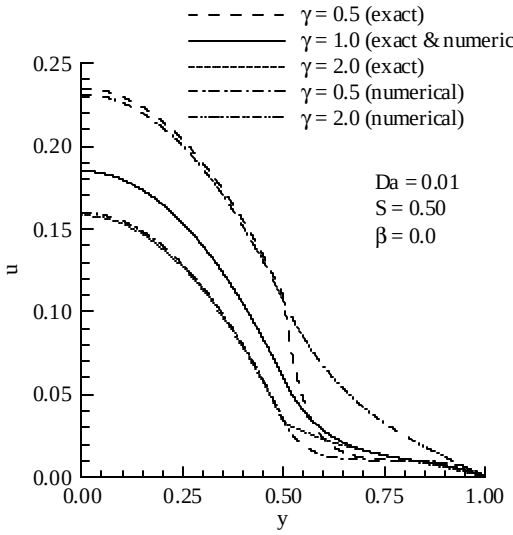

Figure 2a

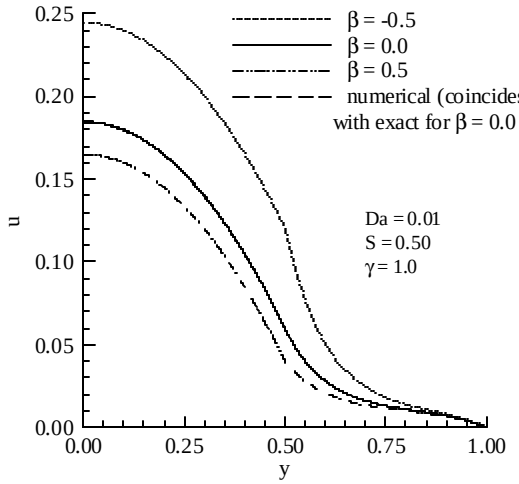

Figure 2b

Figure 2 Comparison between the exact and numerical solutions for a parallel-plate composite channel with porous layers of a uniform porosity attached to the walls for different values of (a) the coefficient γ and (b) the coefficient β

From Figs. 2a and 2b it follows that the numerical solutions obtained utilizing the single-domain do not produce any kink in the curve depicting velocity distribution at the interface.

These figures show that the numerical solution coincides with the exact solution only if $\beta=0$ and $\gamma=1$. The numerical curves for $\gamma=0.5$ and $\gamma=2$ in Fig. 2a are significantly distinct from the curves which depict the exact solution. It should be noted that the single-domain formulation does not allow for any explicit imposing of boundary conditions at the porous/fluid interface, therefore parameter β can not be included into the numerical solution. Figure 2b shows that variation of parameter β results in considerable variation of the velocity distribution in the channel, however, for the reason explained above, the numerical solution does not reflect this variations.

It means that utilization of the single-domain approach implicitly imposes the following boundary conditions at the porous/fluid interface:

$$u\big|_{\tilde{y}=s-0} = u\big|_{\tilde{y}=s+0} \tag{19}$$

$$\left.\frac{\partial \tilde{u}_f}{\partial \tilde{y}}\right|_{\tilde{y}=s+0} = \left.\frac{\partial \tilde{u}_f}{\partial \tilde{y}}\right|_{\tilde{y}=s-0} \tag{20}$$

This conclusion was tested by comparing numerical results obtained by utilizing the single-domain approach with an analytical solution of Eqs. (1)-(2) along with boundary conditions given by Eqs. (3), (4), (6) and (20). If the boundary condition given by Eq. (5) is replaced with the boundary condition given by Eq. (20), numerical and analytical solutions coincide for any values of γ and β (the latter is obvious because in case of Eq. (20) the analytical solution does not depend on β at all).

In other words, from the results obtained it follows that utilization of the single-domain approach is justified only if there is no jump in the shear stress at the interface and simultaneously if the effective viscosity of the porous medium, μ_{eff}, equals to the fluid viscosity, μ_f. The latter requirement is the especially serious limitation. For example, in recent experimental work by Givler and Altobelli [17] a water flow through a tube filled with an open-cell rigid foam of high porosity has been investigated. It has been obtained that for this flow $\mu_{eff} = \left(7.5^{+3.4}_{-2.4}\right)\mu_f$.

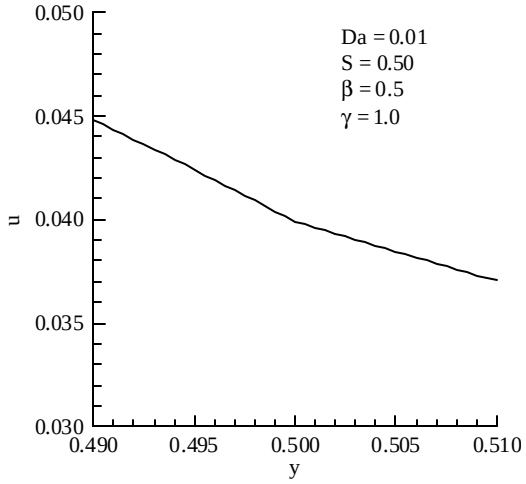

Figure 3 "Exact" velocity distribution near porous/fluid interface for $\beta = 0.5$ of uniform porosity

2.3 PARALLEL-PLATE CHANNEL PARTLY FILLED WITH A POROUS MEDIUM OF VARIABLE POROSITY

2.3.1 Exact Solution

The governing equations and boundary condition are the same as those for the former case and are given by Eqs. (1)-(6). The only difference is that the permeability coefficient in Eqs. (2) and (5) is assumed to be a quadratic function of the coordinate y:

$$K = c(H - \tilde{y})^2 \tag{21}$$

This means that the Darcy number defined in Eq. (14) is also a quadratic function of the coordinate y:

$$Da = c(1 - y)^2 \tag{22}$$

Eqs. (21) and (22) show that in this case the permeability changes from its maximum value at the interface (and this corresponds to the maximum porosity) to zero at the solid wall (this corresponds to the zero porosity).

The exact solution of Eqs. (1)-(6) accounting for Eqs. (21)-(22) can be presented in the following dimensionless form:

$$u = u_i + \frac{1}{2}(S^2 - y^2) \qquad 0 \le y \le S \tag{23}$$

$$u = A(1 - y)^{(1+\sqrt{1+4/(\gamma^2 c)})/2} - \frac{c(1-y)^2}{2\gamma^2 c - 1} \qquad S \le y \le 1 \tag{24}$$

where the dimensionless velocity at the porous/fluid interface can be determined from the following equation:

$$u_i = \frac{(1-S)[2\gamma^2 c - S - \frac{\gamma^2 c}{2}(1+\sqrt{1+\frac{4}{\gamma^2 c}})(1-S)]}{(2\gamma^2 c-1)[\frac{\beta}{\sqrt{c}} + \frac{\gamma^2}{2}(1+\sqrt{1+\frac{4}{\gamma^2 c}})]} \tag{25}$$

and integration constants A and B can be determined from the following equations:

$$A = \frac{\beta\sqrt{c}(1-S) + 2\gamma^2 c - S}{(2\gamma^2 c-1)(1-S)^{(\sqrt{1+4/(\gamma^2 c)}-1)/2}[\frac{\beta}{\sqrt{c}} + \frac{\gamma^2}{2}(1+\sqrt{1+\frac{4}{\gamma^2 c}})]} \tag{26}$$

$$B = \frac{S^2}{2} + \frac{(1-S)[2\gamma^2 c - S - \frac{\gamma^2 c}{2}(1+\sqrt{1+\frac{4}{\gamma^2 c}})(1-S)]}{(2\gamma^2 c-1)[\frac{\beta}{\sqrt{c}} + \frac{\gamma^2}{2}(1+\sqrt{1+\frac{4}{\gamma^2 c}})]} \tag{27}$$

2.3.2 Numerical Solution and Comparison with the Exact Solution

For the single-domain approach numerical procedure for this case Eqs. (16)-(18) have to be solved accounting for variable permeability given by Eq. (21). Figures 4a and 4b depict the comparison between the exact and numerical solutions. The curves depicted in Fig. 4a are computed for c=0.01, S=0.5 and β=0 for three different values of the coefficient γ while the curves depicted in Fig. 4b are computed for c=0.01, S=0.5 and γ=1 for three different values of the coefficient β. Similar to Figs. 2a and 2b, the exact and numerical solutions coincide

only for β=0 and γ=1. This shows that in this case utilization of the single-domain approach results in implicit imposing at the porous/fluid interface the boundary conditions given by Eqs. (19) and (20). This conclusion was again tested by comparing the numerical solution with a modified analytical solutions obtained for the case when Eq. (5) was replaced with Eq. (20). This comparison has shown that the numerical solution coincides with the modified analytical solution for any values of β and γ.

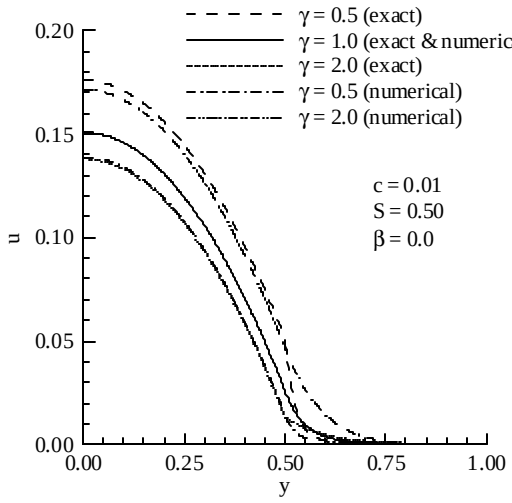

Figure 4a

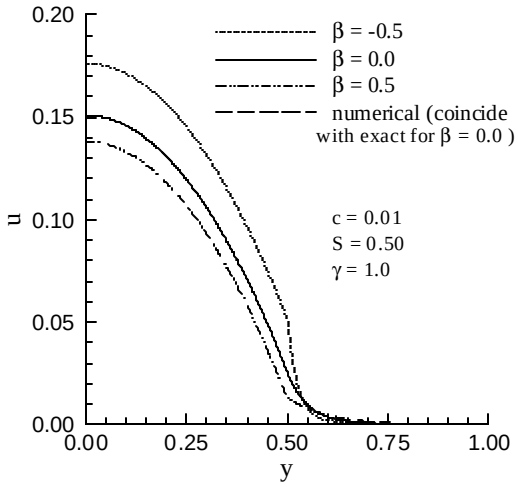

Figure 4b

Figure 4 Comparison between the exact and numerical solutions for a parallel-plate composite channel with porous layers of a variable porosity attached to the walls for different values of (a) the coefficient γ and (b) the coefficient β

2.4 AXISYMMETRIC CHANNEL PARTLY FILLED WITH A POROUS MEDIUM OF UNIFORM POROSITY

2.4.1 Exact Solution

The equations governing the fluid flow in this case take the following form:

$$-\frac{d\tilde{p}}{d\tilde{x}}+\mu_f\left(\frac{d^2\tilde{u}_f}{d\tilde{r}^2}+\frac{1}{\tilde{r}}\frac{d\tilde{u}_f}{d\tilde{r}}\right)=0 \qquad 0\le\tilde{r}\le s \qquad (28)$$

$$-\frac{d\tilde{p}}{d\tilde{x}}+\mu_{eff}\left(\frac{d^2\tilde{u}_f}{d\tilde{r}^2}+\frac{1}{\tilde{r}}\frac{d\tilde{u}_f}{d\tilde{r}}\right)-\frac{\mu_f}{K}\tilde{u}_f=0 \qquad s\le\tilde{r}\le H \qquad (29)$$

where $\tilde{r}$ is the radial coordinate and $\tilde{r}=s$ is the position of the interface.

Equations (28) and (29) must be solved subject to the following boundary conditions:

$$\left.\frac{\partial\tilde{u}_f}{\partial\tilde{r}}\right|_{\tilde{r}=0}=0 \qquad (30)$$

$$\tilde{u}\big|_{\tilde{r}=s-0}=\tilde{u}\big|_{\tilde{r}=s+0} \qquad (31)$$

$$\mu_{eff}\left.\frac{\partial\tilde{u}_f}{\partial\tilde{r}}\right|_{\tilde{r}=s+0}-\mu_f\left.\frac{\partial\tilde{u}_f}{\partial\tilde{r}}\right|_{\tilde{r}=s-0}=\beta\frac{\mu_f}{K^{1/2}}\tilde{u}_f\big|_{\tilde{r}=s} \qquad (32)$$

$$\tilde{u}_f\big|_{\tilde{r}=H}=0 \qquad (33)$$

The exact solution of Eqs. (28)-(29) along with boundary conditions given by Eqs. (30)-(33) can be presented in the following dimensionless form:

$$u=u_i+\frac{1}{4}(S^2-r^2) \qquad 0\le r\le S \qquad (34)$$

$$u = C_1 I_0\left(\frac{r}{\gamma\sqrt{Da}}\right) + D_1 K_0\left(\frac{r}{\gamma\sqrt{Da}}\right) + Da \qquad S \le r \le 1 \qquad (35)$$

where $r = \tilde{r}/H$ and I_ν and K_ν are modified Bessel functions of the order ν.

The dimensionless velocity at the porous/fluid interface is given by the following equation:

$$\begin{aligned} u_i = \{ & Da \times [K_0(\frac{1}{\gamma\sqrt{Da}}) - K_0(\frac{S}{\gamma\sqrt{Da}})][\gamma I_1(\frac{S}{\gamma\sqrt{Da}}) - \beta I_0(\frac{S}{\gamma\sqrt{Da}})] \\ & + Da \times [I_0(\frac{1}{\gamma\sqrt{Da}}) - I_0(\frac{S}{\gamma\sqrt{Da}})][\gamma K_1(\frac{S}{\gamma\sqrt{Da}}) + \beta K_0(\frac{S}{\gamma\sqrt{Da}})] \\ & + [I_0(\frac{1}{\gamma\sqrt{Da}})K_0(\frac{S}{\gamma\sqrt{Da}}) - I_0(\frac{S}{\gamma\sqrt{Da}})K_0(\frac{1}{\gamma\sqrt{Da}})](\frac{S\sqrt{Da}}{2} - \beta Da)\} \\ & \times \{K_0(\frac{1}{\gamma\sqrt{Da}})[\gamma I_1(\frac{S}{\gamma\sqrt{Da}}) - \beta I_0(\frac{S}{\gamma\sqrt{Da}})] + I_0(\frac{1}{\gamma\sqrt{Da}})[\gamma K_1(\frac{S}{\gamma\sqrt{Da}}) + \beta K_0(\frac{S}{\gamma\sqrt{Da}})]\}^{-1} \end{aligned} \qquad (36)$$

and integration constants in Eqs. (34) and (35) are given by the following Equations:

$$\begin{aligned} C_1 = -\{ & Da \times [\gamma K_1(\frac{S}{\gamma\sqrt{Da}}) + \beta K_0(\frac{S}{\gamma\sqrt{Da}})] + K_0(\frac{1}{\gamma\sqrt{Da}})(\frac{S\sqrt{Da}}{2} - \beta Da)\} \\ & \times \{K_0(\frac{1}{\gamma\sqrt{Da}})[\gamma I_1(\frac{S}{\gamma\sqrt{Da}}) - \beta I_0(\frac{S}{\gamma\sqrt{Da}})] + I_0(\frac{1}{\gamma\sqrt{Da}})[\gamma K_1(\frac{S}{\gamma\sqrt{Da}}) + \beta K_0(\frac{S}{\gamma\sqrt{Da}})]\}^{-1} \end{aligned} \qquad (37)$$

$$\begin{aligned} D_1 = \{ & -Da \times [\gamma I_1(\frac{S}{\gamma\sqrt{Da}}) - \beta I_0(\frac{S}{\gamma\sqrt{Da}})] + I_0(\frac{1}{\gamma\sqrt{Da}})(\frac{S\sqrt{Da}}{2} - \beta Da)\} \\ & \times \{K_0(\frac{1}{\gamma\sqrt{Da}})[\gamma I_1(\frac{S}{\gamma\sqrt{Da}}) - \beta I_0(\frac{S}{\gamma\sqrt{Da}})] + I_0(\frac{1}{\gamma\sqrt{Da}})[\gamma K_1(\frac{S}{\gamma\sqrt{Da}}) + \beta K_0(\frac{S}{\gamma\sqrt{Da}})]\}^{-1} \end{aligned} \qquad (38)$$

2.4.2 Numerical Solution and Comparison with the Exact Solution

For the single-domain numerical solution, Eqs. (28) and (29) are combined into one equation which is valid in both porous and clear fluid regions, similar to Eq. (16):

$$-\frac{d\tilde{p}}{d\tilde{x}}+\Psi_1\mu_f\left(\frac{d^2\tilde{u}_f}{d\tilde{r}^2}+\frac{1}{\tilde{r}}\frac{d\tilde{u}_f}{d\tilde{r}}\right)-\Psi_2\frac{\mu_f}{K}\tilde{u}_f=0 \qquad 0\le\tilde{r}\le H \tag{39}$$

where

$$\Psi_1=1, \qquad \Psi_2=0 \qquad 0\le\tilde{r}\le s \tag{40}$$

$$\Psi_1=\mu_{eff}/\mu_f, \ \Psi_2=1 \qquad s\le\tilde{r}\le H \tag{41}$$

Again, no boundary conditions at $\tilde{r}=s$ are required for the numerical solution of Eq. (39). Boundary conditions are required only at the external boundaries of the computational domain, that is at $\tilde{r}=0$ and $\tilde{r}=H$. These boundary conditions are given by Eqs. (30) and (33), respectively.

Figures 5a and 5b depict the comparison between the exact and numerical solutions. The curves depicted in Fig. 5a are computed for Da=0.01, S=0.5 and β=0 for three different values of the coefficient γ while the curves depicted in Fig. 5b are computed for Da=0.01, S=0.5 and γ=1 for three different values of the coefficient β. Similar to Figs. 2a and 2b and to Figs. 4a and 4b, the exact and numerical solutions coincide only for β=0 and γ=1. This shows that in this case utilization of the single-domain approach again results in implicit imposing at the porous/fluid interface not the "exact" boundary conditions given by Eqs. (31) and (32), but the boundary conditions which require continuity of both the filtration velocity and its first derivative with respect to the transverse coordinate:

$$\tilde{u}\big|_{\tilde{r}=s-0}=\tilde{u}\big|_{\tilde{r}=s+0} \tag{42}$$

$$\left.\frac{\partial \tilde{u}_f}{\partial \tilde{r}}\right|_{\tilde{r}=s+0} = \left.\frac{\partial \tilde{u}_f}{\partial \tilde{r}}\right|_{\tilde{r}=s-0} \qquad (43)$$

This conclusion was again tested by comparing the numerical solution with a modified analytical solution obtained for the case when Eq. (32) was replaced with Eq. (43). This comparison has shown that the numerical solution coincides with the modified analytical solution for any values of β and γ.

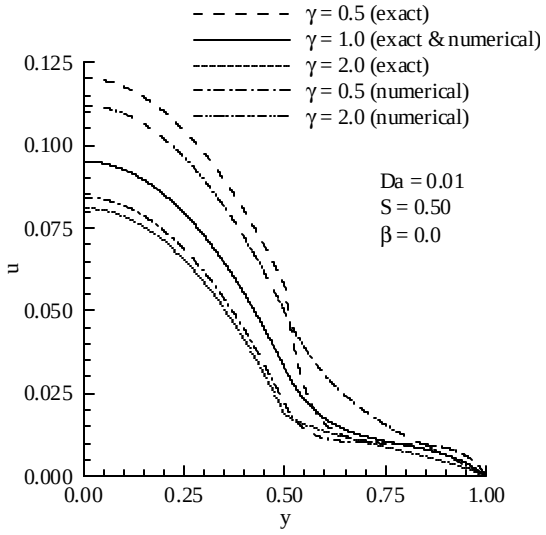

Figure 5a

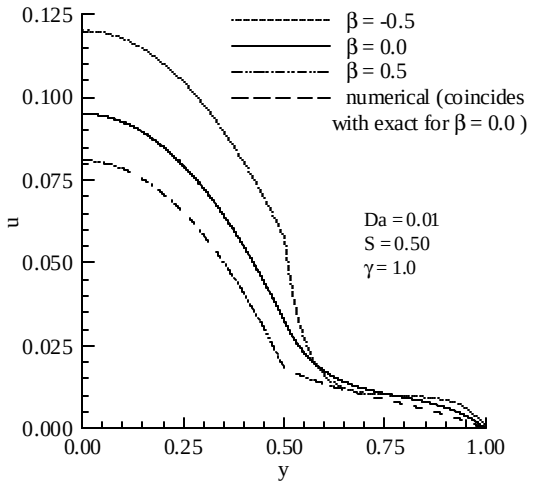

Figure 5b

Figure 5 Comparison between the exact and numerical solutions for an axisymmetric composite channel with a porous layer of a uniform porosity attached to the wall for different values of (a) the coefficient γ and (b) the coefficient β

2.5 CONCLUSIONS

The main objective of this chapter is to establish what boundary conditions are implicitly imposed at the porous/fluid interface when the convective problem in a composite channel is numerically solved utilizing the single-domain approach. To do this, comparisons between the single-domain numerical solutions and the exact solutions are carried out for three different geometrical configurations of a composite channel. It is established that utilization of the single-domain approach results in implicit imposing at the interface the condition of continuity of the filtration velocity and also the condition of continuity of its first derivative with respect to the transverse coordinate. This means that the single-domain approach is applicable to the fluid flow problems in composite configurations only if there is no jump in the shear stress at the interface and if simultaneously the effective viscosity of porous medium equals to the fluid viscosity.

REFERENCES

1. Beckermann, C. and Viskanta, R., Double-diffusive convection during dendritic solidification of a binary mixture, *PhysicoChemical Hydrodynamics*, 10:195-213, 1988

2. Bennon, W.D. and Incropera, F.P., A continuum model for momentum, heat and species transport in binary solid-liquid phase change systems - II. Application to solidification in a rectangular cavity, *International Journal of Heat and Mass Transfer*, 30:2171-2187, 1987

3. Schneider, M.C. and Beckermann, C., A numerical study of the combined effects of microsegregation, mushy zone permeability and flow, caused by volume contraction and thermosolutal convection, on macrosegregation and eutectic formation in binary alloy solidification, *International Journal of Heat and Mass Transfer*, 38:3455-3473, 1995

4. Yoo, H. and Viskanta, R., Effect of anisotropic permeability on the transport process during solidification of a binary mixture, *International Journal of Heat and Mass Transfer*, 35:2335-2346, 1992

5. Voller, V.R. and Prakash, C., A fixed grid numerical modeling methodology for convection-diffusion mushy region phase-change problems, *International Journal of Heat and Mass* Transfer, 30:1709-1719, 1987

6. Vafai, K. and Kim, S.J., Analysis of surface enhancement by a porous substrate, *ASME Journal of Heat Transfer*, 112:700-706, 1990

7. Huang, P.C. and Vafai, K., Flow and heat transfer control over an external surface using a porous block arrangement, *International Journal of Heat and Mass Transfer*, 36:4019-4032, 1993

8. Kim, S.J. and Choi, C.Y., Convective heat transfer in porous and overlying fluid layers heated from below, *International Journal of Heat and Mass Transfer*, 39:319-329, 1996

9. Hadim, A., Forced convection in a porous channel with localized heat sources, *ASME Journal of Heat Transfer*, 116:465-472, 1994

10. Ochoa-Tapia, J.A. and Whitaker, S., Momentum transfer at the boundary between a porous medium and a homogeneous fluid - I. Theoretical development, *International Journal of Heat and Mass Transfer*, 38:2635-2646, 1995

11. Ochoa-Tapia, J.A. and Whitaker, S., Momentum transfer at the boundary between a porous medium and a homogeneous fluid - II. Comparison with experiment, *International Journal of Heat and Mass Transfer*, 38:2647-2655, 1995

12. D.A. Nield, The limitations of the Brinkman-Forchheimer equation in modeling flow in a saturated porous medium and at an interface, *Int. J. Heat and Fluid Flow*, vol. 12, pp. 269-272, 1991

13. Kuznetsov, A.V., Analytical investigation of the fluid flow in the interface region between a porous medium and a clear fluid in channels partially filled with a porous medium, *Applied Scientific Research*, 56:53-67, 1996

14. Kuznetsov, A.V., Influence of the stress jump boundary condition at the porous-medium/clear-fluid interface on a flow at a porous wall, *International Communications in Heat and Mass Transfer*, 24:401-410, 1997

15. Poulikakos, D. and Kazmierczak, M., Forced convection in a duct partially filled with a porous material, *ASME Journal of Heat Transfer*, 109:653-662, 1987

16. Vafai, K. and Kim, S.J., Fluid mechanics of the interface region between a porous medium and a fluid layer - an exact solution, *International Journal of Heat and Fluid Flow*, 11:254-256, 1990

17. Givler, R.C. and Altobelli, S.A., A determination of the effective viscosity for the Brinkman-Forchheimer flow model, *Journal of Fluid Mechanics*, 258:355-370, 1994

3 FORCED CONVECTION IN A COUETTE FLOW IN A COMPOSITE DUCT: AN ANALYSIS OF THERMAL DISPERSION AND NON-DARCIAN EFFECTS

ABSTRACT

An analysis of fluid flow and heat transfer in a fully developed Couette flow through a composite channel that is partly filled with a clear fluid and partly with a fluid saturated porous medium is presented. The porous medium is attached to a fixed plate and uniform heat fluxes of different intensities are imposed on both plates. The momentum transport is described by the Brinkman-Forchheimer-Darcy equation and the effect of transverse thermal dispersion is accounted for in the energy equation for the porous region. An analytical solution for the fluid flow is obtained utilizing the boundary layer technique. The temperature field and the Nusselt numbers at the upper and lower plates are obtained by direct numerical integration. The dependence of the Nusselt numbers on the thickness of the porous region, the ratio of heat fluxes on both plates, and the Darcy number, is investigated.

3.1 INTRODUCTION

A number of investigations of transport phenomena in composite channels that are filled with both a porous medium and a clear fluid have recently been conducted. Poulikakos and Kazmierczak [1] analytically investigated pressure-driven forced convection in composite

ducts partly filled with a Brinkman-Darcy porous medium. Vafai and Kim [2] obtained the first exact solution for fluid flow in the interface region. A perturbation analysis of fluid flow and heat transfer in the interface region between a clear fluid and a Brinkman-Forchheimer porous medium was presented in Vafai and Thiyagaraja [3]. The groundbreaking works of Vafai and Kim [4, 5] demonstrated that by utilizing the boundary layer approach it is possible to obtain an analytical solution for the forced convection problem in a channel filled with a fluid saturated porous medium.

The problem of boundary conditions at the fluid/porous interface was first investigated by Beavers and Joseph [6] and Beavers et al. [7]. Proceeding from the results of an experimental investigation, a slip-flow boundary condition at the fluid/porous interface was suggested in these references. According to this boundary condition, the velocity gradient on the fluid side of the interface is proportional to the slip velocity at the interface. Further insight into this problem was gained in Ochoa-Tapia and Whitaker [8, 9], who by means of complicated volume averaging analysis of the momentum equations in the interface region have shown that matching the Brinkman-Darcy and Stokes equation retains continuity of velocity, but produces a jump in the shear stress.

Although the Couette flow is one of the most important and fundamental flow situations, investigations of forced convection in the Couette flow through a porous channel have been rather limited. Bhargava and Sacheti [10] and Daskalakis [11] numerically investigated heat transfer in Couette flows through a porous medium by using the Brinkman-Darcy equation. Nakayama [12] presented analytical solutions for the momentum transport in a Couette flow described by the Brinkman-Forchheimer-Darcy equation. Kuznetsov [13] adopted the

approach of Vafai and Kim [4, 5] and obtained an analytical solution for the fluid flow and heat transfer of Couette flows in a composite channel. However, in Kuznetsov [13] no thermal dispersion was considered and one of the two parallel plates was treated as adiabatic. Figure 6 depicts the schematic diagram of the problem investigated in this chapter. Incompressible, steady, fully developed, laminar flow under constant pressure gradient in a composite channel bounded by two infinite parallel plates is considered. The lower part of the channel is filled with a clear fluid and the upper part is filled with a fluid saturated isotropic porous medium of uniform porosity. The upper plate and the porous medium are fixed and the lower plate moves with a constant velocity, $\tilde{u}_w$. Uniform heat fluxes q_1'' and q_2'' are imposed on the fixed plate and the moving plate, respectively.

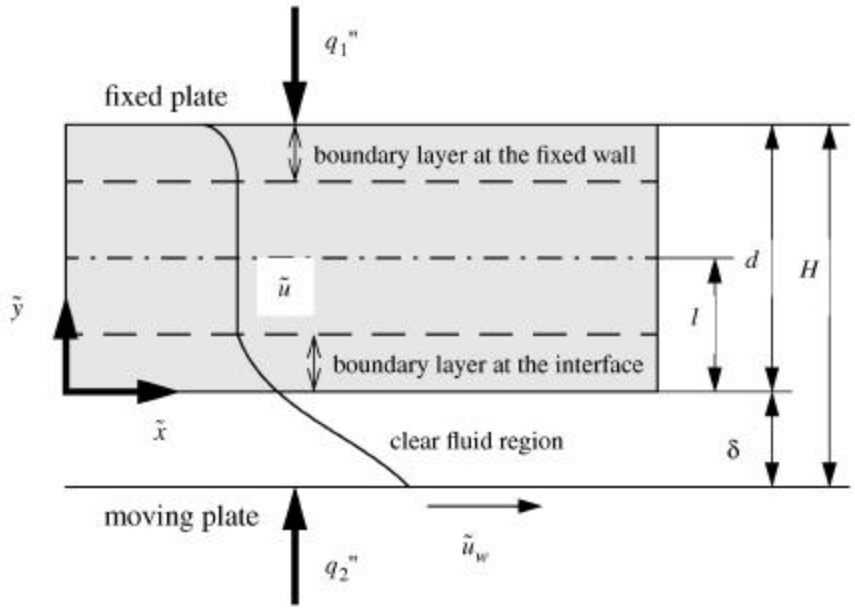

Figure 6 Schematic diagram of the problem

3.2 PROBLEM FORMULATION

The governing equations for this problem can be presented as:

$$-\frac{d\tilde{p}}{d\tilde{x}}+\mu_f\frac{d^2\tilde{u}_f}{d\tilde{y}^2}=0 \qquad -\delta\le\tilde{y}\le 0 \qquad (1)$$

$$-\frac{d\tilde{p}}{d\tilde{x}}+\mu_{eff}\frac{d^2\tilde{u}_f}{d\tilde{y}^2}-\frac{\mu_f}{K}\tilde{u}_f-\frac{\rho F}{K^{1/2}}\tilde{u}_f^{\,2}=0 \qquad 0\le\tilde{y}\le d \qquad (2)$$

$$\rho_f c_f\tilde{u}_f\frac{\partial\tilde{T}}{\partial\tilde{x}}=k_f\frac{\partial^2\tilde{T}}{\partial\tilde{y}^2} \qquad -\delta\le\tilde{y}\le 0 \qquad (3)$$

$$\rho_f c_f\tilde{u}_f\frac{\partial\tilde{T}}{\partial\tilde{x}}=\frac{\partial}{\partial\tilde{y}}\left[\left(k_m+Ck_f\,\mathrm{Pr}\frac{\rho_f\tilde{u}_f d_p}{\mu_f}\right)\frac{\partial\tilde{T}}{\partial\tilde{y}}\right] \qquad 0\le\tilde{y}\le d \qquad (4)$$

where C is the dimensionless experimental constant, c_f is the specific heat capacity of the fluid, d is the thickness of the porous region, d_p is the average particle diameter in the porous region, F is the Forchheimer coefficient, K is the permeability of the porous medium, k_f is the thermal conductivity of the fluid, k_m is the stagnant thermal conductivity of the porous medium, $\tilde{T}$ is the fluid temperature, $\tilde{u}_f$ is the filtration velocity, $\tilde{x}$ is the streamwise coordinate, $\tilde{y}$ is the transverse coordinate, μ_{eff} is the effective viscosity of the porous medium, μ_f is the fluid viscosity, ρ_f is the fluid density, and δ is the width of the gap between the porous medium and the moving plate.

Eqs. (1) and (2) are the momentum equations for the clear fluid region and the porous region, respectively. For the porous region, this is the Brinkman-Forchheimer-extended Darcy

equation. Eqs. (3) and (4) are the energy equations for the clear fluid and porous regions, respectively. Longitudinal heat conduction is neglected in the energy equations and in Eq. (4) the local thermal equilibrium assumption between the fluid and solid phases is utilized. The longitudinal thermal dispersion is also neglected, which is valid for large Peclet numbers. This is because for large Peclet numbers $\partial^2\tilde{T}/\partial\tilde{x}^2$ is negligible in comparison with $\partial^2\tilde{T}/\partial\tilde{y}^2$, which means longitudinal conduction is negligible [14]. The contribution from longitudinal dispersion is then automatically negligible since it is multiplied by a negligible term; therefore only the effect of transverse thermal dispersion is included in the energy equation for the porous region.

Equations (1)-(4) must be solved subject to the following boundary conditions:

$$\tilde{u}_f\big|_{\tilde{y}=-\delta} = \tilde{u}_w, \qquad -k_f \left.\frac{\partial\tilde{T}}{\partial y}\right|_{\tilde{y}=-\delta} = q_2'' \tag{5}$$

$$\tilde{u}_f\big|_{\tilde{y}=-0} = \tilde{u}_f\big|_{\tilde{y}=+0}, \qquad \mu_{eff}\left.\frac{\partial\tilde{u}_f}{\partial\tilde{y}}\right|_{\tilde{y}=+0} - \mu_f\left.\frac{\partial\tilde{u}_f}{\partial\tilde{y}}\right|_{\tilde{y}=-0} = \beta\frac{\mu_f}{K^{1/2}}\tilde{u}_f\big|_{\tilde{y}=0} \tag{6a}$$

$$\tilde{T}\big|_{\tilde{y}=-0} = \tilde{T}\big|_{\tilde{y}=+0}, \qquad \left(k_m + Ck_f\,\mathrm{Pr}\frac{\rho_f\tilde{u}_f d_p}{\mu_f}\right)\left.\frac{\partial\tilde{T}}{\partial\tilde{y}}\right|_{\tilde{y}=+0} = k_f\left.\frac{\partial\tilde{T}}{\partial\tilde{y}}\right|_{\tilde{y}=-0} \tag{6b}$$

$$\tilde{u}_f\big|_{\tilde{y}=d} = 0, \qquad \left(k_m + Ck_f\,\mathrm{Pr}\frac{\rho_f\tilde{u}_f d_p}{\mu_f}\right)\left.\frac{\partial\tilde{T}}{\partial\tilde{y}}\right|_{\tilde{y}=d} = q_1'' \tag{7}$$

where β is the dimensionless adjustable coefficient describing the jump in the shear stress at the interface of the clear fluid and the porous medium [8, 9].

The governing equations and boundary conditions can be recast into dimensionless form by introducing the following dimensionless parameters:

$$u = \frac{\tilde{u}_f}{\tilde{u}_w}, \qquad U = \frac{\tilde{U}_m}{\tilde{u}_w}, \qquad T = \frac{\tilde{T} - \tilde{T}_1}{\tilde{T}_m - \tilde{T}_1}, \qquad y = \frac{\tilde{y}}{H}, \tag{8a}$$

$$\gamma = \left[\frac{\mu_{eff}}{\mu_f}\right]^{1/2}, \quad G = -\frac{\left(\frac{d\tilde{p}}{d\tilde{x}}\right)H^2}{\mu_f \tilde{u}_w}, \qquad Da = \frac{K}{H^2} \tag{8b}$$

where Da is the Darcy number, G is the dimensionless applied pressure gradient, $H = d + \delta$ is the height of the channel, Re_H is the Reynolds number, $\tilde{T}_1$ is the temperature at the fixed wall, $\tilde{T}_m = \frac{1}{\tilde{U}_m H}\int_{-\delta}^{d} \tilde{u}_f \tilde{T} d\tilde{y}$ is the mean temperature of the flow, and $\tilde{U}_m = \frac{1}{H}\int_{-\delta}^{d} \tilde{u}_f d\tilde{y}$ is the mean flow velocity.

According to Bejan [15], the First Law of Themodynamics results in the following relationship:

$$\frac{\partial \tilde{T}}{\partial \tilde{x}} = \frac{d\tilde{T}_m}{d\tilde{x}} = \frac{(q_1'' + q_2'')}{\rho_f c_f \tilde{U}_m H} \tag{9}$$

The dimensionless equations can now be presented as:

$$G + \frac{d^2u}{dy^2} = 0 \qquad -S_1 \le y \le 0 \tag{10}$$

$$G + \gamma^2 \frac{d^2u}{dy^2} - \frac{1}{Da}u - \frac{Re_H F}{Da^{1/2}}u^2 = 0 \qquad 0 \le y \le S_2 \tag{11}$$

$$-\frac{1}{2}\frac{u}{U}\mathrm{Nu}_1\left(1+\frac{q_2''}{q_1''}\right)=\frac{d^2T}{dy^2} \qquad -S_1 \le y \le 0 \qquad (12)$$

$$-\frac{1}{2}\frac{u}{U}\mathrm{Nu}_1\left(1+\frac{q_2''}{q_1''}\right)=\frac{d}{dy}\left[\left(\frac{k_m}{k_f}+C\cdot \mathrm{Pr}\cdot \mathrm{Re}_H\, u\right)\frac{dT}{dy}\right] \qquad 0 \le y \le S_2 \qquad (13)$$

where $S_1 = \delta / H$ and $S_2 = d / H$,

$$\mathrm{Nu}_1 = \frac{2Hq_1''}{k_f(\tilde{T}_1 - \tilde{T}_m)} \qquad (14a)$$

is the Nusselt number at the fixed plate, and

$$\mathrm{Re}_H = \frac{\rho_f \tilde{u}_w H}{\mu_f} \qquad (14b)$$

is the Reynolds number.

The dimensionless boundary conditions which corespond to Eqs. (10)-(13) are:

$$u\big|_{y=-S_1} = 1, \qquad \left.\frac{dT}{dy}\right|_{y=-S_1} = \frac{q_2''}{2q_1''}\mathrm{Nu}_1 \qquad (15)$$

$$u\big|_{y=-0} = u\big|_{y=+0}, \qquad \gamma^2\left.\frac{du}{dy}\right|_{y=+0} - \left.\frac{du}{dy}\right|_{y=-0} = \frac{\beta}{\sqrt{\mathrm{Da}}}u\big|_{y=0} \qquad (16a)$$

$$T\big|_{y=-0} = T\big|_{y=+0}, \qquad \left(\frac{k_m}{k_f}+C\cdot \mathrm{Pr}\cdot \mathrm{Re}_H\, u\right)\left.\frac{dT}{dy}\right|_{y=+0} = \left.\frac{dT}{dy}\right|_{y=-0} \qquad (16b)$$

$$u\big|_{y=S_2} = 0, \qquad T\big|_{y=S_2} = 0 \qquad (17)$$

The Nusselt number at the moving plate is defined as:

$$Nu_2 = \frac{2Hq_2^{"}}{k_f(\tilde{T}_2 - \tilde{T}_m)} \tag{18}$$

The relationship between Nu_1 and Nu_2 is given by:

$$Nu_2 = Nu_1 \frac{q_2^{"}}{q_1^{"}} \frac{1}{1-T(-S_1)} \tag{19}$$

3.3 SOLUTION

3.3.1 Velocity Distribution

The velocity distribution in the clear fluid region $(-S_1 \le y \le 0)$ can be obtained by integrating Eq. (10) subject to boundary conditions given by Eqs. (15) and (16a). This results in:

$$u = u_i - \frac{1}{2}Gy^2 - \frac{1}{2}\frac{(GS_1^2 - 2u_i + 2)y}{S_1} \tag{20}$$

where u_i is the velocity at the clear fluid/porous medium interface.

The exact solution of the velocity distribution in the porous region is not available. Following Vafai and Kim [2, 4, 5], the assumption is made that the two momentum boundary layers in the porous region (the boundary layer near the fixed plate and the boundary layer near the interface) do not overlap in the center of the porous region, at $\tilde{y} = l$. Under this assumption, the following conditions are valid outside the momentum boundary layers:

$$u \to u_\infty \text{ and } \frac{\partial u}{\partial y} \to 0 \text{ as } y = L \tag{21}$$

where L is the y-coordinate of any point in the far-field region. Here L is chosen as $S_2/2$.

From Eq. (21) the momentum equation in the far-field region reduces to:

$$G - \frac{1}{Da} u_\infty - F_D u_\infty^2 = 0 \tag{22}$$

where

$$F_D = \frac{Re_H F}{Da^{1/2}}. \tag{23}$$

From Eq. (22), the velocity in the far-field region is found to be:

$$u_\infty = \frac{-1 + \sqrt{1 + 4F_D G Da^2}}{2DaF_D} \tag{24}$$

Using this approach the velocity distribution in the porous region can be obtained.

In the boundary layer near the interface ($0 \le y \le L$), the velocity distribution is given by the following equation:

$$u = (u_\infty + u_1)\left[\frac{1 - z_1}{1 + z_1}\right]^2 - u_1 \tag{25}$$

where

$$u_1 = 2u_\infty + \frac{3}{2DaF_D} \tag{26}$$

and

$$z_1 = \frac{1-\left[\dfrac{u_i+u_1}{u_\infty+u_1}\right]^{1/2}}{1+\left[\dfrac{u_i+u_1}{u_\infty+u_1}\right]^{1/2}} \exp\left\{-\frac{y}{\gamma}\left[\frac{2}{3}F_D(u_\infty+u_1)\right]^{1/2}\right\} \tag{27}$$

In the boundary layer near the fixed wall ($L \le y \le S_2$), the velocity distribution is given by the following equation:

$$u = (u_\infty + u_1)\left[\frac{z_2-1}{z_2+1}\right]^2 - u_1 \tag{28}$$

where u_1 is given by Eq. (26), and z_2 is given as:

$$z_2 = \frac{1+\left[\dfrac{u_1}{u_\infty+u_1}\right]^{1/2}}{1-\left[\dfrac{u_1}{u_\infty+u_1}\right]^{1/2}} \exp\left\{\frac{1}{\gamma}\left[\frac{2}{3}F_D(u_\infty+u_1)\right]^{1/2}(S_2-y)\right\} \tag{29}$$

The dimensionless velocity at the clear fluid/porous medium interface, u_i, can be found from the jump in the shear stress condition given by Eq. (16a). This results in the following equation for u_i:

$$-\gamma(u_i-u_\infty)\left[\frac{2}{3}F_D(u_i+u_1)\right]^{1/2} + \frac{1}{2}\frac{GS_1^2-2u_i+2}{S_1} = \frac{\beta}{\sqrt{Da}}u_i \tag{30}$$

The dimensionless mean velocity, U, can be found from the following equation:

$$U = \int_{-S_1}^{0} u\,dy + \int_{0}^{L} u\,dy + \int_{L}^{S_2} u\,dy \tag{31}$$

This results in the following equation for U:

$$\begin{aligned} U = {} & \frac{1}{2}u_i S_1 + \frac{1}{12}GS_1^3 + \frac{1}{2}S_1 + u_\infty S_2 + \frac{2\sqrt{6}\gamma\sqrt{\frac{u_\infty + u_1}{F_D}}\left(\sqrt{\frac{u_i + u_1}{u_\infty + u_1}} + 1\right)}{D_1\left(\sqrt{\frac{u_i + u_1}{u_\infty + u_1}} - 1\right) - \left(\sqrt{\frac{u_i + u_1}{u_\infty + u_1}} + 1\right)} \\ & + \frac{2\sqrt{6}\gamma\sqrt{\frac{u_\infty + u_1}{F_D}}\left(1 - \sqrt{\frac{u_1}{u_\infty + u_1}}\right)}{D_2\left(\sqrt{\frac{u_i + u_1}{u_\infty + u_1}} + 1\right) - \left(\sqrt{\frac{u_i + u_1}{u_\infty + u_1}} - 1\right)} + \sqrt{6}\gamma\sqrt{\frac{u_\infty + u_1}{F_D}}\left(\sqrt{\frac{u_i + u_1}{u_\infty + u_1}} + \sqrt{\frac{u_1}{u_\infty + u_1}}\right) \end{aligned} \tag{32}$$

where

$$D_1 = \exp\left(-\frac{S_2\sqrt{F_D(u_\infty + u_1)}}{\sqrt{6}\gamma}\right) \tag{33a}$$

and

$$D_2 = \exp\left(\frac{S_2\sqrt{F_D(u_\infty + u_1)}}{\sqrt{6}\gamma}\right) \tag{33b}$$

3.3.2 Temperature Distribution

With the velocity distribution found, the temperature distribution and the Nusselt number at the fixed plate can be obtained by solving Eqs. (12) and (13) and by utilizing the compatibility condition [14], i.e.

$$\int_{-S_1}^{S_2} uTdy = U \tag{34}$$

In the clear fluid region ($-S_1 \le y \le 0$), the temperature distribution is:

$$T = T_i + Nu_1 y\left[\frac{q_2''}{2q_1''} - \frac{(1+\frac{q_2''}{q_1''})S_1}{4U}\left(\frac{1}{6}GS_1^2 + u_i + 1\right)\right] + \frac{Nu_1(1+\frac{q_2''}{q_1''})y^2}{48U}\left(Gy^2 + 2GS_1 y - 12u_i\right) + \frac{Nu_1(1+\frac{q_2''}{q_1''})y^3}{12S_1 U}(1-u_i) \tag{35}$$

where T_i is the temperature at the clear fluid/porous medium interface.

The exact solution of Eq. (13) (providing the velocity distribution is given by Eqs. (25)-(29)) is not available, but the temperature gradient can be obtained analytically.

In the boundary layer near the interface ($0 \le y \le L$), the temperature gradient is:

$$\frac{dT}{dy} = \left\{-\frac{1}{2}\frac{Nu_1\left(1+\frac{q_2''}{q_1''}\right)}{U}\left[-\frac{4\exp(Ay)\cdot(u_\infty + u_1)}{A(\exp(A_1 y)+B)} + \frac{4(u_\infty + u_1)}{A(1+B_1)} + u_\infty y\right] + (R + C\cdot Pr\cdot Re_H u_i)\left.\frac{dT}{dy}\right|_{y=+0}\right\} \times (R + C\cdot Pr\cdot Re_H u)^{-1} \tag{36}$$

where

$$A = \frac{\sqrt{\frac{2}{3}F_D(u_\infty + u_1)}}{\gamma} \tag{37a}$$

$$B_1 = \frac{1-\sqrt{\frac{u_i + u_1}{u_\infty + u_1}}}{1+\sqrt{\frac{u_i + u_1}{u_\infty + u_1}}} \tag{37b}$$

and

$$\left.\frac{dT}{dy}\right|_{y=+0} = Nu_1 \frac{\frac{1}{2}\frac{q_2''}{q_1''} - \frac{S_1}{4U}\left(1+\frac{q_2''}{q_1''}\right)\left(\frac{1}{6}GS_1^2 + u_i + 1\right)}{R + C\cdot Pr\cdot Re_H\, u_i} \tag{38}$$

In the boundary layer near the fixed wall ($L \le y \le S_2$), the temperature gradient is:

$$\begin{aligned}\frac{dT}{dy} = \Bigg\{ & -\frac{Nu_1}{2}\frac{\left(1+\frac{q_2''}{q_1''}\right)}{U}\frac{1}{A[\exp(Ay) + B_2\exp(AS_2)][\exp(AL) + B_2\exp(AS_2)]} \\ & \{[B_2\exp(A(S_2+y)) + B_2\exp(A(S_2+L)) + \exp(A(L+y)) + B_2^2\exp(2AS_2)] \\ & \times u_\infty A(y-L) + 4B_2(u_\infty + u_1)[\exp(A(S_2+L)) - \exp(A(S_2+y))]\} \\ & + (R + C\cdot Pr\cdot Re_H\, u_\infty)\left.\frac{dT}{dy}\right|_{y=L} \Bigg\} \times (R + C\cdot Pr\cdot Re_H\, u)^{-1}\end{aligned} \tag{39}$$

where

$$B_2 = \frac{1+\sqrt{\frac{u_1}{u_\infty + u_1}}}{1-\sqrt{\frac{u_1}{u_\infty + u_1}}} \tag{40}$$

and

$$\left.\frac{dT}{dy}\right|_{y=L} = \left\{ -\frac{1}{2}\frac{Nu_1\left(1+\frac{q_2''}{q_1''}\right)}{U}\left[-\frac{4\exp(AL)\cdot(u_\infty+u_1)}{A(\exp(AL)+B_1)} + \frac{4(u_\infty+u_1)}{A(1+B_1)} + u_\infty L \right] \right.$$
$$\left. + (R + C\cdot Pr\cdot Re_H\, u_i)\left.\frac{dT}{dy}\right|_{y=+0} \right\} \times (R + C\cdot Pr\cdot Re_H\, u_\infty)^{-1} \qquad (41)$$

3.4 RESULTS AND DISSCUSSION

Figure 7a shows the dimensionless velocity and the temperature distributions in the channel. This figure is computed utilizing the following parameters: $C = 0.1$, $F = 0.1$, $G = 10$, $Pr = 0.7$, $q_2''/q_1'' = 1$, $R = 1$, $Re_H = 10^4$, $S_1 = 0.2$, $\gamma = 1$, and $\beta = 0$. The velocity decreases rapidly as the distance from the moving plate increases and the velocity in the porous region is much smaller than in the clear fluid region. Increasing the Darcy number results in an increase in the permeability of the porous medium and therefore leads to a larger velocity in the porous region. It can be seen that for the cases of $Da = 10^{-2}$ and $Da = 10^{-4}$ there is a region where the velocity does not change with y, which means the momentum boundary layers in the porous region do not overlap. Thus for these cases the boundary layer approximation is valid. The validity of the boundary layer approximation is investigated in detail in Vafai and Kim [5] and in Kuznetsov [16]. These references show that this approximation is valid for most practical porous media and only fails if the Darcy number takes on very large values (of the order of unity). In Nield et al. [17] a novel approach is

suggested that makes it possible to handle the fluid flow problem without utilizing the boundary layer approximation. This novel approach works well for large Darcy numbers, however, it can result in numerical difficulties for small Darcy numbers. Since in this analysis porous media with moderately small Darcy numbers are considered, the boundary layer approximation is more appropriate.

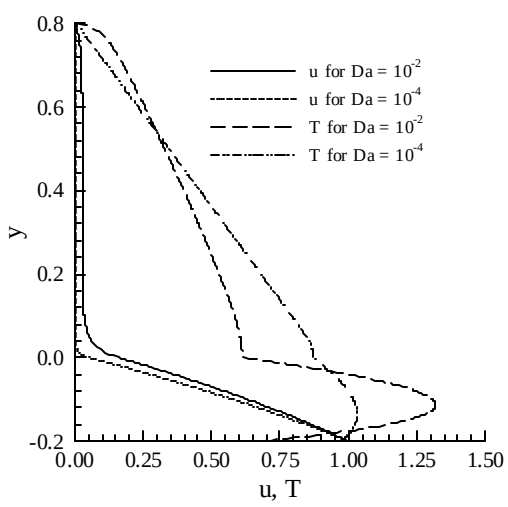

Figure 7a

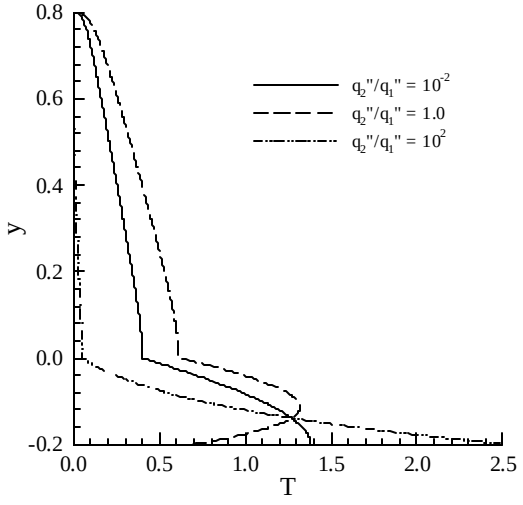

Figure 7b

Figure 7 Velocity and temperature distributions for different values of (a) the Darcy number and (b) heat flux ratio

According to Fig. 7a, the dimensionless temperature distributions are quite different for varing Darcy numbers. There is a visible kink at the porous/clear fluid interface even when $R = 1$. This is because the thermal dispersion in the transverse direction is accounted for in

the computation. Figure 7b gives the dimensionless temperature distributions in the channel at different $q_2^{"}/q_1^{"}$ for $\mathrm{Da} = 10^{-2}$. Other parameter values are the same as those for Fig. 7a. It can be seen that the temperature distribution changes dramatically with $q_2^{"}/q_1^{"}$. For the case of $q_2^{"}/q_1^{"} = 10^{-2}$, the temperature gradient at the lower plate is almost zero, meaning that the lower plate is almost adiabatic. Similarly, when $q_2^{"}/q_1^{"} = 10^{2}$, the temperature gradient at the upper plate is almost zero, meaning that the upper plate is almost adiabatic.

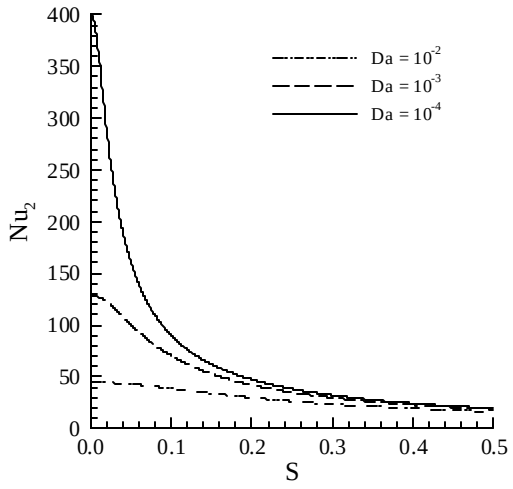

Figure 8 Comparison of the Nusselt number obtained here with Kuznetsov [13]

To test this solution, the comparison of the Nusselt number at the lower plate with the results of Kuznetsov [13] is given in Fig. 8. In this reference the flow is caused by the moving plate alone, the pressure gradient is zero, the transverse thermal dispersion in the porous medium is

not accounted for, and the upper plate is adiabatic. Thus the corresponding parameter values utilized in this computation are: $C = 0$, $F_D = 10^2$, $G = 10^{-6}$, $Pr = 0.7$, $q_2^{''}/q_1^{''} = 10^8$, $R = 1$, $\gamma = 1$, $\beta = 0$. The Nusselt number utilized in Kuznetsov [13] corresponds to the Nusselt number utilized in this chapter divided by a factor of two and the curves depicted in Fig. 8 correspond to the definition of the Nusselt number utilized in this chapter. It can be seen that the Nusselt number at the lower plate computed utilizing Eq. (18) completely coincides with the results of Kuznetsov [13], visually it is not possible to distinguish between the curves computed utilizing the present solution and the curves computed utilizing Kuznetsov [13].

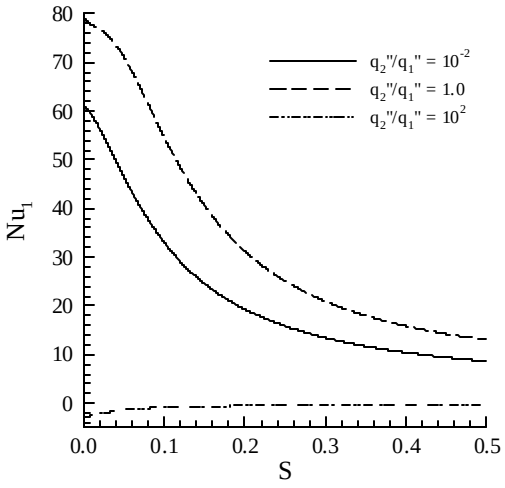

Figure 9a

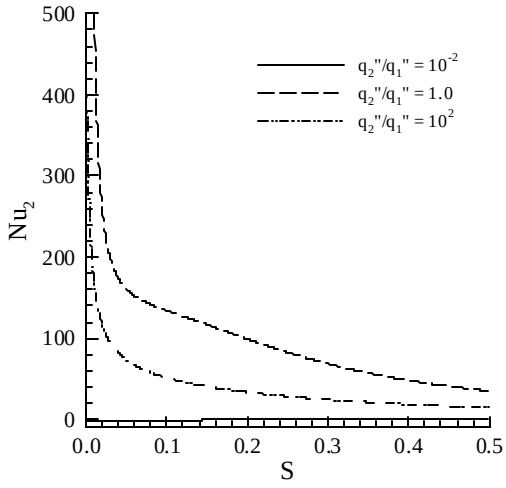

Figure 9b

Figure 9 Nusselt numbers (a) at the fixed plate and (b) at the moving plate varying with the width of the clear fluid region S (= S_1) for different heat flux ratios

Figure 9 depicts the dependence of the Nusselt numbers at both plates on the size of the gap between the porous medium and the moving plate for different $q_2^{''}/q_1^{''}$. The following parameters are utilized in this computation: $C = 0.1,\ Da = 10^{-2},\ F = 0.1,\ G = 10,\ Pr = 0.7,$ $R = 1,\ Re_H = 10^4,\ \gamma = 1$, and $\beta = 0$. For $q_2^{''}/q_1^{''} = 10^{-2}$ and $q_2^{''}/q_1^{''} = 1$, Fig. 9 shows that the Nusselt number of the upper plate (Nu_1) decreases rapidly with an increase in the width of the gap. For $q_2^{''}/q_1^{''} = 10^2$, Fig. 9a shows that Nu_1 is negative. In this case a negative Nusselt number means that the temperature of the upper plate, $\tilde{T}_1$, is lower than the mean flow temperature, $\tilde{T}_m$. This is possible when the lower plate is heated more heavily than the upper plate. Similarly, the Nusselt number at the lower plate (Nu_2) can take on negative values when the temperature at the lower plate, $\tilde{T}_2$, is lower than the mean flow temperature, $\tilde{T}_m$. This can happen when the upper plate is heated more heavily than the lower plate, so that for $q_2^{''}/q_1^{''} = 10^{-2}$ Nu_2 in Fig. 9b is negative.

Figure 10 shows the dependence of the Nusselt numbers on the width of the gap between the porous medium and the moving (lower) plate for different values of the Darcy number when $q_2^{''}/q_1^{''} = 10^2$. The other parameters have the same values as those utilized for Fig. 9. The Nusselt number at the upper plate changes monotonically with the gap for $Da = 10^{-2}$. For $Da = 10^{-4}$ the minimum value of the Nusselt number is obtained at $S_1 = 0.06$. The minimum possessed by the Nu(s) dependence is investigated and explained in Poulikakos and Kazmierczak [1]. The Nusselt number of the lower plate decreases rapidly with an increase in the width of the gap.

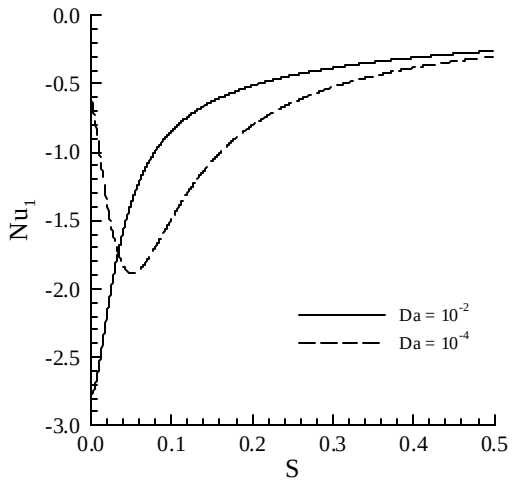

Figure 10a

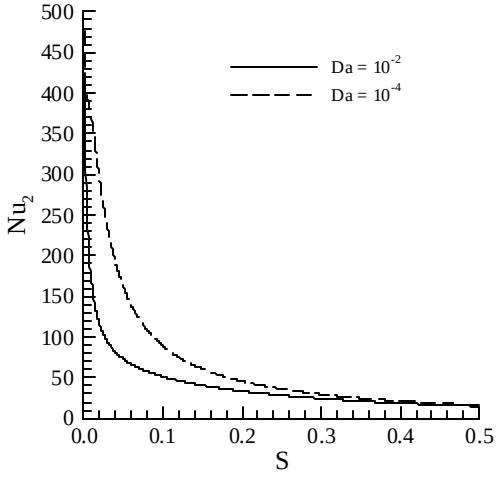

Figure 10b

Figure 10 Nusselt numbers (a) at the fixed plate and (b) at the moving plate varying with the width of the clear fluid region S (= S_1) for different values of Darcy number

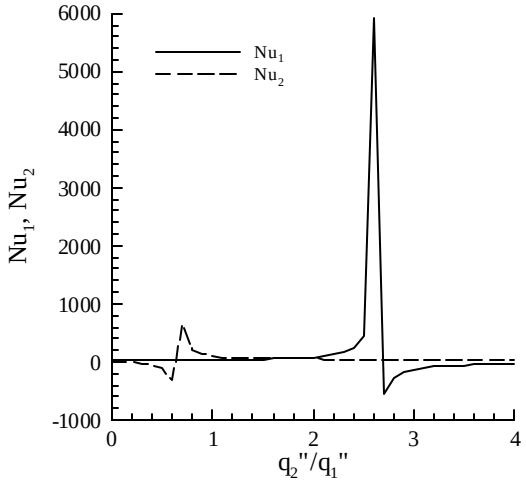

Figure 11a

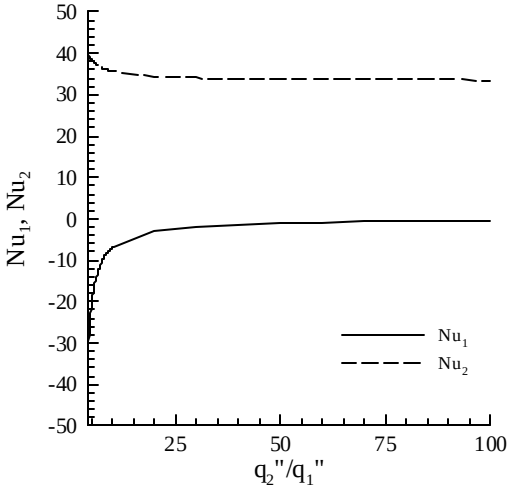

Figure 11b

Figure 11 Nusselt numbers as a function of heat flux ratio

Figure 11 depicts changes in the Nusselt numbers at both plates for $q_2^{''}/q_1^{''}$. The parameter values utilized in this computation are $C = 0.1$, $Da = 10^{-2}$, $F = 0.1$, $G = 10$, $Pr = 0.7$, $R = 1$, $Re_H = 10^4$, $S_1 = 0.2$, $\gamma = 1$, and $\beta = 0$. Fig. 11a shows there is a jump at a certain $q_2^{''}/q_1^{''}$ value for each Nusselt number. This jump in the Nusselt number occurs when the denominators on the right-hand side of Eqs. (14a) and (18), $\tilde{T}_1 - \tilde{T}_m$ for Nu_1 and $\tilde{T}_2 - \tilde{T}_m$ for Nu_2, approach zero. This unexpected behavior of the Nusselt number is actually in good agreement with classical results. According to Kays and Crawford [18], for the Poiseuitte flow of a clear fluid in a parallel-plane duct which is heated from both walls, the Nusselt number can be expressed as:

$$Nu_1 = \frac{2}{\frac{1}{2} - \frac{9}{70}\left(1 + \frac{q_2^{''}}{q_1^{''}}\right)} \tag{41a}$$

$$Nu_2 = \frac{2}{\frac{1}{2} - \frac{9}{70}\left(1 + \frac{q_1^{''}}{q_2^{''}}\right)} \tag{41b}$$

These equations show that for these Nusselt numbers there is a jump when $\frac{9}{70}\left(1 + \frac{q_2^{''}}{q_1^{''}}\right) \to \frac{1}{2}$ or $\frac{9}{70}\left(1 + \frac{q_1^{''}}{q_2^{''}}\right) \to \frac{1}{2}$. Since the jump in the Nusselt number can occur in simple clear fluid flows, it can also happen in a more complex flow, such as the one considered in this chapter. Figure 11b shows that when $q_2^{''}/q_1^{''} \geq 40$, the Nusselt numbers on both plates approach

asymptotic values. This asymptotic case corresponds to the situation when the upper (fixed) plate is adiabatic, and heat flux is imposed only at the lower (moving) plate.

3.5 CONCLUSIONS

The fluid flow and heat transfer in a fully developed Couette flow through a composite channel that is partly filled with a clear fluid and partly with a fluid saturated porous medium are analyzed. Uniform heat fluxes are imposed on both of the plates. In the porous region the Brinkman-Forchheimer-extended Darcy equation is utilized to describe the momentum transport while the thermal dispersion along the transverse direction is accounted for in the energy equation for the porous region. The boundary layer approximation is utilized to analytically solve the momentum equation in the porous region. This approximation is valid for most practical porous media, except when the Darcy number takes on very large values. The dependence of the Nusselt numbers on the width of the gap between the porous medium and the moving plate, on the ratio of heat fluxes on both plates, and on the Darcy number is analyzed. The Nusselt numbers at both plates display a jump if the ratio of heat fluxes imposed at the upper and lower plates change. If the heat flux ratio approaches infinity, the Nusselt numbers at the upper and lower plates approach asymptotic values.

REFERENCES

1. Poulikakos, D. and Kazmierczak, M., Forced convection in a duct partially filled with a porous material, *ASME Journal of Heat Transfer*, 109:653-662, 1987

2. Vafai, K. and Kim, S.J., Fluid mechanics of the interface region between a porous medium and a fluid layer – an exact solution, *International Journal of Heat and Fluid Flow*, 11:254-256, 1990

3. Vafai, K. and Thiyagaraja, R., Analysis of flow and heat transfer at the interface region of a porous medium, *International Journal of Heat Mass Transfer*, 30:1391-1405, 1987

4. Vafai, K. and Kim, S.J., Forced convection in a channel filled with a porous medium: an exact solution, *ASME Journal of Heat Transfer*, 111:1103-1106, 1989

5. Vafai, K. and Kim, S.J., Discussion of the paper by A. Hadim "Forced convection in a porous channel with localized heat sources", *ASME Journal of Heat Transfer*, 117:1097-1098, 1995

6. Beavers, G.S. and Joseph, D.D., Boundary conditions at a naturally permeable wall. *Journal of Fluid Mechanics*, 30:197-207, 1967

7. Beavers, G.S., Sparrow, E.M., and Magnuson, R.A., Experiments on coupled parallel flows in a channel and a bounding porous medium, *Journal of Basic Engineering, Trans. ASME*, 92:843-848, 1970

8. Ochoa-Tapia, J.A., and Whitaker, S., Momentum transfer at the boundary between a porous medium and a homogeneous fluid – I. Theoretical development, *International Journal of Heat Mass Transfer*, 28:2635-2646, 1995

9. Ochoa-Tapia, J.A., and Whitaker, S., Momentum transfer at the boundary between a porous medium and a homogeneous fluid – II. Comparison with experiment, *International Journal of Heat Mass Transfer*, 28:2647-2655, 1995

10. Bhargava, S.K. and Sacheti, N.C., Heat transfer in generalized Couette flow of two immiscible Newtonian fluids through a porous channel: use of Brinkman model. *Indian Journal of Technology*, 27:211-214, 1989

11. Daskalakis, J., Couette flow through a porous medium of a high Prandtl number fluid with temperature-dependent viscosity, *International Journal of Energy Research*, 14:21-26, 1990

12. Nakayama, A., Non-Darcy Couette flow in a porous medium filled with an inelastic non-Newtonian fluid, *ASME Journal of Fluids Engineering*, 114:642-647, 1992

13. Kuznetsov, A.V., Analytical investigation of Couette flow in a composite channel partially filled with a porous medium and partially with a clear fluid, *International Journal of Heat Mass Transfer*, 41(16):2556-2560, 1998

14. Bejan, A., *Convection Heat Transfer, 2nd ed.*, Wiley, New York, p304, 1995

15. Bejan, A., *Heat Transfer*, Wiley, New York, 1993

16. Kuznetsov, A.V., Fluid mechanics and heat transfer in the interface region between a porous medium and a fluid layer: a boundary layer solution, *Journal of Porous media*, 2:309-321, 1999

17. Nield, D.A., Junqueira, S.L.M., and Lage J.L., Forced convection in a fluid saturated porous medium channel with isothermal or isoflux boundaries, *Journal of Fluid Mechanics*, 322:201-214, 1996

18. Kays, W.M. and Crawford, M.E., *Convective heat and mass transfer*, McGraw-Hill, Inc., p152 (problem 9-1), 1993

4 INVESTIGATION OF THE EFFECT OF THERMAL DISPERSION ON FORCED CONVECTION IN A CIRCULAR DUCT PARTLY FILLED WITH A SATURATED POROUS MEDIUM

ABSTRACT

A numerical simulation of the fully developed forced convection in a circular duct partly filled with a fluid saturated porous medium is presented. The Brinkman–Forchheimer-extended Darcy equation is used to describe the fluid flow in the porous region. The energy equation for the porous region accounts for the effect of thermal dispersion. The dependence of the Nusselt number on a number of parameters, such as the Reynolds number, the Darcy number, the Forchheimer coefficient, as well as the thickness of the porous region is investigated. The numerical results obtained in this research are in agreement with published experimental data.

4.1 INTRODUCTION

Considerable attention has recently been paid to the fluid flow and heat transfer in composite systems that are composed of regions filled either with a homogeneous fluid or with a fluid saturated porous medium. This interest is due to the wide use of these systems in engineering

applications such as solar receiver devices, thermal insulation, heat exchangers, energy storage units, ceramic processing and catalytic reactors [1].

Studies in this field gradually progress towards complex models. At the beginning of these studies, a simple Darcy equation was used to describe the fluid flow in a porous medium. However, for high-speed flows it was found that that there is a deviation from the classical linear correlation between the pressure gradient and the filtration velocity, which is given by the Darcy equation. Then the so-called Darcy-Forchheimer equation, which includes a quadratic drag term to account for the deviation from linearity, was introduced. Further development of the model made by Brinkman was stimulated by a desire to impose the non-slip boundary condition at the solid wall [3]. It has recently become very popular to utilize the Brinkman-Forchheimer-Darcy equation, which accounts for both non-linear effects and viscous effects near the boundaries. Now this model is accepted and widely used [3-9]. Moreover, it has been found that thermal dispersion effects play an important role in forced convection in porous media [1, 10-14]. The models used to describe the transport phenomena in porous media are getting more and more sophisticated. The more complex the model is, the more difficult it is to get an accurate general theoretical solution. Poulikakos and Kazmierczak [15] presented analytical solutions for fully developed forced convection in parallel plate channels and circular ducts partly filled with porous media. They utilized the Brinkman flow model and neglected thermal dispersion in the radial and transverse directions. Vafai and Kim [16] obtained a boundary layer solution for a fully developed forced convection problem in a parallel plate channel filled with a Brinkman-Forchheimer porous medium. Nield et al. [2] performed a theoretical analysis and obtained a solution for

the same problem without utilizing the boundary layer approximation. Neither Vafai and Kim [16] nor Nield et al. [2] considered the effect of thermal dispersion. In this chapter the Brinkman-Forchheimer-Darcy equation is used as the momentum equation for the porous region and the radial thermal dispersion in the porous medium is accounted for in the energy equation for the porous region. Because of the geometrical configuration considered in this chapter and the presence of a non-linear term in the momentum equation, it is impossible to obtain an exact analytical solution for this problem. Thus, a numerical solution is adopted. The two cases of a constant heat flux and a constant wall temperature are investigated.

4.2 PROBLEM FORMULATION

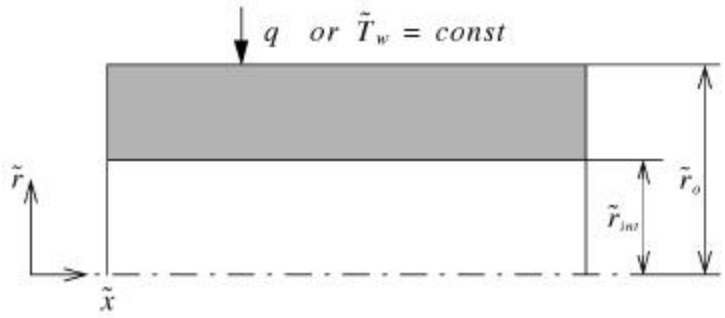

Figure 12 Schematic diagram of the problem

The geometrical configuration considered in this research is displayed in Fig. 12. Forced convection flow occurs in an infinite horizontal circular duct whose wall is subject to a uniform heat flux or a constant temperature. Assuming hydrodynamically and thermally fully developed flow, the governing equations for this problem are:

$$-\frac{d\tilde{p}}{d\tilde{x}} + \mu_f \left(\frac{d^2\tilde{u}_f}{d\tilde{r}^2} + \frac{1}{\tilde{r}} \frac{d\tilde{u}_f}{d\tilde{r}} \right) = 0 \qquad 0 \le \tilde{r} \le r_{int} \qquad (1)$$

$$-\frac{d\tilde{p}}{d\tilde{x}} + \mu_{eff} \left(\frac{d^2\tilde{u}_f}{d\tilde{r}^2} + \frac{1}{\tilde{r}} \frac{d\tilde{u}_f}{d\tilde{r}} \right) - \frac{\mu_f}{K} \tilde{u}_f - \frac{\rho_f c_F}{K^{1/2}} \tilde{u}_f^2 = 0 \qquad r_{int} \le \tilde{r} \le r_o \qquad (2)$$

$$\rho_f c_f \tilde{u}_f \frac{\partial \tilde{T}}{\partial \tilde{x}} = k_f \left(\frac{\partial^2 \tilde{T}}{\partial \tilde{r}^2} + \frac{1}{\tilde{r}} \frac{\partial \tilde{T}}{\partial \tilde{r}} \right) \qquad 0 \le \tilde{r} \le r_{int} \qquad (3)$$

$$\rho_f c_f \tilde{u}_f \frac{\partial \tilde{T}}{\partial \tilde{x}} = \frac{1}{\tilde{r}} \frac{\partial}{\partial \tilde{r}} \left[\left(k_m + C k_f \, Pr \frac{\rho_f \tilde{u}_f d_p}{\mu_f} \right) \tilde{r} \frac{\partial \tilde{T}}{\partial \tilde{r}} \right] \qquad r_{int} \le \tilde{r} \le r_o \qquad (4)$$

where C is the dimensionless experimental constant, c_f is the specific heat capacity of the fluid, c_F is the Forchheimer coefficient, d_p is the average particle diameter, K is the permeability of the porous medium, k_f is the thermal conductivity of the fluid, k_m is the stagnant thermal conductivity of the porous medium, r_o is the radius of the circular duct, r_{int} is the radius of the clear fluid region, $\tilde{T}$ is the temperature, $\tilde{u}_f$ is the filtration velocity, μ_{eff} is the effective viscosity of the porous medium, μ_f is the fluid viscosity, and ρ_f is the fluid density.

The Forchheimer coefficient, c_F, and the permeability, K, can be calculated utilizing formulas that are based on the results of experimental measurements carried out by Ergun [17]:

$$c_F = \frac{1.75}{\sqrt{150}\varepsilon^{3/2}} \tag{5}$$

$$K = \frac{\varepsilon^3 d_p^{\ 2}}{150(1-\varepsilon)^2} \tag{6}$$

where ε is the porosity of the porous region.

The stagnant thermal conductivity of the porous medium, k_m, is calculated as:

$$k_m = \varepsilon k_f + (1-\varepsilon)k_s \tag{7}$$

where k_s is the thermal conductivity of solid phase.

Equations (1) and (2) are the momentum equations for the clear fluid and porous regions, respectively. In the porous region, the Brinkman-Forchheimer-extended Darcy equation is used. Equations (3) and (4) are the energy equations for the clear fluid and porous regions, respectively. The longitudinal heat conduction and longitudinal thermal dispersion are both neglected, which is justified if the Peclet number is large enough. Isotropy and homogeneity of the porous medium and local thermodynamic equilibrium in the porous region are assumed.

4.2.1 Constant Heat Flux

For the constant heat flux situation, Eqs. (1) - (4) must be solved subject to the following boundary conditions:

$$\left.\frac{\partial \tilde{u}_f}{\partial \tilde{r}}\right|_{\tilde{r}=0} = 0 \qquad \left.\frac{\partial \tilde{T}}{\partial \tilde{r}}\right|_{\tilde{r}=0} = 0 \tag{8}$$

$$\tilde{u}_f\big|_{\tilde{r}=r_{int}-0} = \tilde{u}_f\big|_{\tilde{r}=r_{int}+0} \qquad \mu_{eff}\left.\frac{\partial \tilde{u}_f}{\partial \tilde{r}}\right|_{\tilde{r}=r_{int}+0} - \mu_f\left.\frac{\partial \tilde{u}_f}{\partial \tilde{r}}\right|_{\tilde{r}=r_{int}-0} = \beta\frac{\mu_f}{K^{1/2}}\tilde{u}_f\big|_{\tilde{r}=r_{int}} \tag{9a}$$

$$\tilde{T}\big|_{\tilde{r}=r_{int}-0} = \tilde{T}\big|_{\tilde{r}=r_{int}+0} \qquad \left(k_m + Ck_f\,\mathrm{Pr}\frac{\rho_f \tilde{u}_f d_p}{\mu_f}\right)\left.\frac{\partial \tilde{T}}{\partial \tilde{r}}\right|_{\tilde{r}=r_{int}+0} = k_f\left.\frac{\partial \tilde{T}}{\partial \tilde{r}}\right|_{\tilde{r}=r_{int}-0} \tag{9b}$$

$$\tilde{u}_f\big|_{\tilde{r}=r_o} = 0 \qquad \left(k_m + Ck_f\,\mathrm{Pr}\frac{\rho_f \tilde{u}_f d_p}{\mu_f}\right)\left.\frac{\partial \tilde{T}}{\partial \tilde{r}}\right|_{\tilde{r}=r_o} = q'' \tag{10}$$

where β is the dimensionless adjustable coefficient describing the jump in shear stress at the interface between the clear fluid and the porous medium [18, 19].

The governing equations. (1) - (4) and boundary conditions (8) - (10) for the constant heat flux case can be recast into the dimensionless form by introducing the following dimensionless parameters:

$$u = \frac{\tilde{u}_f \mu_f}{Gr_o^{\,2}}, \qquad U = \frac{\tilde{U}_m \mu_f}{Gr_o^{\,2}}, \quad T = \frac{\tilde{T} - \tilde{T}_w}{\tilde{T}_m - \tilde{T}_w}, \qquad r = \frac{\tilde{r}}{r_o}, \tag{11a}$$

$$G = -\frac{d\tilde{p}}{d\tilde{x}}, \qquad \gamma = \left(\frac{\mu_{eff}}{\mu_f}\right)^{1/2}, \quad F = \frac{\rho_f c_F}{K^{1/2}}\frac{r_o^{\,4}}{\mu_f^2}G, \qquad Da = \frac{K}{r_o^{\,2}} \tag{11b}$$

where Da is the Darcy number, F is the scaled Forchheimer coefficient, and G is the applied pressure gradient.

In Eq. (11a), $\tilde{U}_m$ is the mean velocity and $\tilde{T}_m$ is the mean temperature of the flow. They are defined as:

$$\tilde{U}_m = \frac{2}{r_o^{\,2}} \int_0^{r_o} \tilde{u}\tilde{r}\,d\tilde{r} \tag{12}$$

$$\tilde{T}_m = \frac{2}{r_o^{\,2}\tilde{U}_m} \int_0^{r_o} \tilde{u}\tilde{T}\tilde{r}\,d\tilde{r} \tag{13}$$

For the constant heat flux [20], the First Law of Thermodynamics results in the following relationship:

$$\frac{\partial \tilde{T}}{\partial \tilde{x}} = \frac{d\tilde{T}_m}{d\tilde{x}} = \frac{2}{r_o} \frac{q''}{\rho_f c_f \tilde{U}_m} \tag{14}$$

The dimensionless governing equations can now be presented as:

$$1 + \frac{d^2u}{dr^2} + \frac{1}{r}\frac{du}{dr} = 0 \qquad 0 \le r \le R_{int} \tag{15}$$

$$1 + \gamma^2\left(\frac{d^2u}{dr^2} + \frac{1}{r}\frac{du}{dr}\right) - \frac{1}{Da}u - Fu^2 = 0 \qquad R_{int} \le r \le 1 \tag{16}$$

$$-\frac{u}{U}Nu = \frac{d^2T}{dr^2} + \frac{1}{r}\frac{dT}{dr} \qquad 0 \le r \le R_{int} \tag{17}$$

$$-\frac{u}{U}Nu = \frac{1}{r}\frac{d}{dr}\left[\left(\frac{k_m}{k_f} + C \cdot Pr \cdot Re_p\, u\right) r \frac{dT}{dr}\right] \qquad R_{int} \le r \le 1 \tag{18}$$

where Nu is the Nusselt number defined by Eq. (19) below:

$$\mathrm{Nu} = \frac{\mathrm{hD}}{\mathrm{k}} = \frac{2\mathrm{r_o q''}}{\mathrm{k_f}(\tilde{\mathrm{T}}_\mathrm{w} - \tilde{\mathrm{T}}_\mathrm{m})} \tag{19}$$

$\mathrm{Re_p}$ in Eq. (18) is the Reynolds number based on the characteristic velocity scale, $\mathrm{Gr_o}^2/\mu_\mathrm{f}$, given by Eq. (20). An alternative would be to define the Reynolds number based on the mean flow velocity. In that case, however, the Reynolds number would depend on the solution, therefore using a characteristic velocity scale is preferable.

$$\mathrm{Re_p} = \frac{\left(\frac{\mathrm{Gr_o}^2}{\mu_\mathrm{f}}\right)\mathrm{d_p}}{\nu_\mathrm{f}} \tag{20}$$

where ν_f is the kinematic viscosity of the fluid.

The dimensionless form of boundary conditions given by Eqs. (8) - (10) is:

$$\left.\frac{\mathrm{du}}{\mathrm{dr}}\right|_{\mathrm{r=0}} = 0 \qquad \left.\frac{\mathrm{dT}}{\mathrm{dr}}\right|_{\mathrm{r=0}} = 0 \tag{21}$$

$$\mathrm{u}\big|_{\mathrm{r=R_{int}-0}} = \mathrm{u}\big|_{\mathrm{r=R_{int}+0}} \qquad \gamma^2 \left.\frac{\mathrm{du}}{\mathrm{dr}}\right|_{\mathrm{r=R_{int}+0}} - \left.\frac{\mathrm{du}}{\mathrm{dr}}\right|_{\mathrm{r=R_{int}-0}} = \frac{\beta}{\sqrt{\mathrm{Da}}}\mathrm{u}\big|_{\mathrm{r=R_{int}}} \tag{22a}$$

$$\mathrm{T}\big|_{\mathrm{r=R_{int}-0}} = \mathrm{T}\big|_{\mathrm{r=R_{int}+0}} \qquad \left(\frac{\mathrm{k_m}}{\mathrm{k_f}} + \mathrm{C}\cdot\mathrm{Pr}\cdot\mathrm{Re_p}\,\mathrm{u}\right)\left.\frac{\mathrm{dT}}{\mathrm{dr}}\right|_{\mathrm{r=R_{int}+0}} = \left.\frac{\mathrm{dT}}{\mathrm{dr}}\right|_{\mathrm{r=R_{int}-0}} \tag{22b}$$

$$\mathrm{u}\big|_{\mathrm{r=1}} = 0 \qquad \mathrm{T}\big|_{\mathrm{r=1}} = 0 \tag{23}$$

In the energy equations (Eqs. (17) and (18)), the Nusselt number is present as a parameter. Therefore, one more equation is needed to close this problem. This additional equation is given by the compatibility condition obtained from the definition of $\tilde{T}_m$ [20]:

$$\int_0^1 uTrdr = \frac{U}{2} \tag{24}$$

4.2.2 Constant Wall Temperature

The dimensional governing equations and boundary conditions for this case are similar to those for the isoflux case (Eqs. (1) - (4) and (8) – (10)). The difference is that the second equation in Eq. (10) is replaced by:

$$\tilde{T}\Big|_{\tilde{r}=r_o} = \tilde{T}_w \tag{25}$$

The dimensionless governing equations and boundary conditions for the flow velocity are the same as for the isoflux case and are given by Eqs. (15), (16), (21), (22a), and (23). According to Bejan [20], a pertinent relationship between $\frac{\partial \tilde{T}}{\partial \tilde{x}}$ and $\frac{\partial \tilde{T}_m}{\partial \tilde{x}}$ for the isothermal boundary condition is given by the following equation:

$$\frac{\partial \tilde{T}}{\partial \tilde{x}} = T\frac{d\tilde{T}_m}{d\tilde{x}} = T\frac{2}{r_o}\frac{q_w}{\rho_f c_f \tilde{U}_m} \tag{26}$$

This results in the following dimensionless energy equations for the clear fluid and porous regions, respectively:

$$-\frac{u}{U}NuT = \frac{d^2T}{dr^2} + \frac{1}{r}\frac{dT}{dr} \qquad 0 \le r \le R_{int} \qquad (27)$$

$$-\frac{u}{U}NuT = \frac{1}{r}\frac{d}{dr}\left[\left(\frac{k_m}{k_f} + C \cdot Pr \cdot Re_p\, u\right) r \frac{dT}{dr}\right] \qquad R_{int} \le r \le 1 \qquad (28)$$

The dimensionless boundary conditions for the temperature are also the same as those for the isoflux wall case, which are given by Eqs. (21), (22b), and (23). Since the Nusselt number is present in the energy equations (Eqs. (27) and (28)) as an unknown parameter, an additional equation is needed again to close the problem formulation. This additional equation follows from the definition of the Nusselt number:

$$Nu = -2\frac{k_m}{k_f}\frac{dT}{dr}\bigg|_{r=1} \qquad (29)$$

4.3 NUMERICAL PROCEDURE

Since there is a non-linear term in the momentum equation for the porous region, the equations are first written in the finite-difference form while the Newton iteration method is used to obtain the velocity field. Once the velocity distribution is found, it is easy to obtain the temperature distribution. For the isoflux wall, $\frac{T}{Nu}$ can be computed from Eqs. (15) - (18) and (21) - (23). The Nusselt number can then be obtained by substituting the velocity distribution and $\frac{T}{Nu}$ into Eq. (24).

In the case of the isothermal wall, it is important to avoid a trivial solution for the temperature. The same method as in Poulikakos and Kazmierczak [15] and Nield et al. [2] is utilized here. First a value of the Nusselt number is guessed and Eq. (29) is utilized to obtain an expression for the first interior node near the wall. The temperature distribution for this Nusselt number is computed beginning from the wall and proceeding towards the duct center. Then the Newton iteration is used to adjust the Nusselt number and the process is repeated until the boundary condition at the center of the duct is satisfied.

4.4 RESULTS AND DISCUSSION

4.4.1 Constant Heat Flux

Figure 13 shows how the Nusselt number changes in relation to the Reynolds number, Re_d, according to these computations and shows a comparison of the numerical results with the experimental results obtained by Quinton and Storrow [21]. Since the experimental results given by Quinton and Storrow [21] are reported in terms of Re_d, the numerical results obtained here are also given in terms of Re_d, where Re_d is the Reynolds number based on the mean flow velocity and is associated with previously utilized Re_p by the following correlation:

$$Re_d = U Re_p \qquad (30)$$

The parameters utilized in the computation of Fig. 13 are the same as in Quinton and Storrow [21], $Da = 3.3895\times10^{-5}$, $F = 513.7467\times Re_p$, $k_m / k_f = 1.2075$, $Pr = 0.7$, $R_{int} = 0.0$, $\varepsilon = 0.37$, and $\gamma = \frac{1}{\sqrt{\varepsilon}}$. For the constant C, two different values are utilized, $C = 0.08$ and $C = 0.1$ (0.1 is the value suggested in Wakao and Kaguei [22]). When the Reynolds number is very small (of the order of unity), the Nusselt number does not depend on the Reynolds number and has an asymptotic value of 9.31. There is some difference between the numerical results and the experimental data for small Reynolds numbers. This is because longitudinal thermal dispersion is neglected in the computations, which can only be done for large Peclet numbers $(Pe = Pr\cdot Re)$. If the Reynolds number is larger than 100, the Nusselt number increases rapidly with an increase in the Reynolds number and the numerical results agree well with the experimental data, especially in the case of $C = 0.08$.

Figure 14a displays the velocity distributions between the duct center and the wall for different values of the scaled Forchheimer coefficient, F, and the radius of the clear fluid region, R_{int}. As expected, an increase in the Forchheimer coefficient causes a decrease in the velocity distribution. This is because an increase in the Forchheimer coefficient means an increase in the resistance to the flow. It is also noticeable that when R_{int} is 0.25 there is a far-field region in the porous medium where the velocity does not change along the radius. This far-field region is located between the two momentum boundary layers, one of which is located near the solid wall and the other near the porous medium/clear fluid interface [23, 24]. When increasing R_{int} from 0.25 to 0.80, the velocity in the porous region stays nearly

the same, but the velocity in the clear fluid region increases considerably. Since the presence of the porous medium heavily affects the fluid flow in the duct, it can be expected that it will also affect the heat transfer. Figure 14b displays the temperature distributions from the duct center to the wall. There is a kink at the interface, which in this case is caused by thermal dispersion in the porous medium. According to the second Equation in (22b), thermal dispersion results in a discontinuity in the temperature gradient at the interface, even when stagnant thermal conductivity of the porous medium, k_m, is equal to the fluid thermal conductivity, k_f, as was assumed in computing of Fig. 14b.

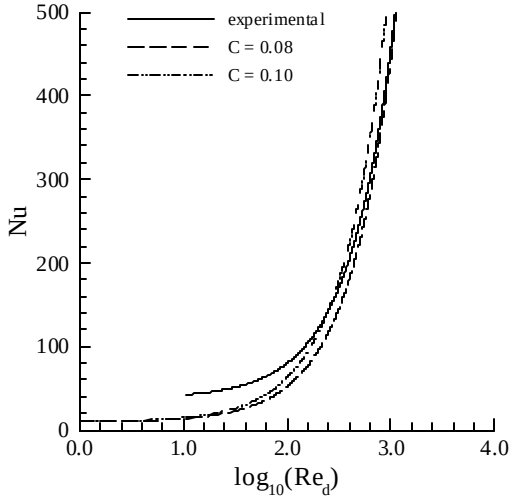

Figure 13 Dependence of the Nusselt number on the particle Reynolds number for the case of an isoflux wall

The effect of the position of the clear fluid/porous medium interface on the Nusselt number is illustrated in Fig. 15 for different values of the Darcy number and the Forchheimer coefficient. The case when $R_{int} = 0$ corresponds to the duct being completely filled with the porous medium. When most of the duct is filled with the porous medium ($R_{int} \leq 0.05$), the Nusselt number has nearly no dependence on R_{int}. When the duct is completely filled with clear fluid region, i.e. $R_{int} = 1$, the Nusselt number approaches 4.36, which coincides with the value given in Bejan [20]. Increasing the Darcy number causes an increase in the Nusselt number while increasing the Forchheimer coefficient causes a decrease in the Nusselt number. This is because a large Darcy number corresponds to a larger permeability of the porous medium, which translates to a larger filtration velocity, while a larger Forchheimer coefficient means a stronger resistance to the flow, which translates to a small filtration velocity. When the Darcy number is of the order of 10^{-3} or less and the Forchheimer coefficient is of the order of 10^{3} or greater, the Nusselt number does not monotonically change with the thickness of the clear fluid region, but has a minimum value. This effect was first shown and explained in Poulikakos and Kazmierczak [15].

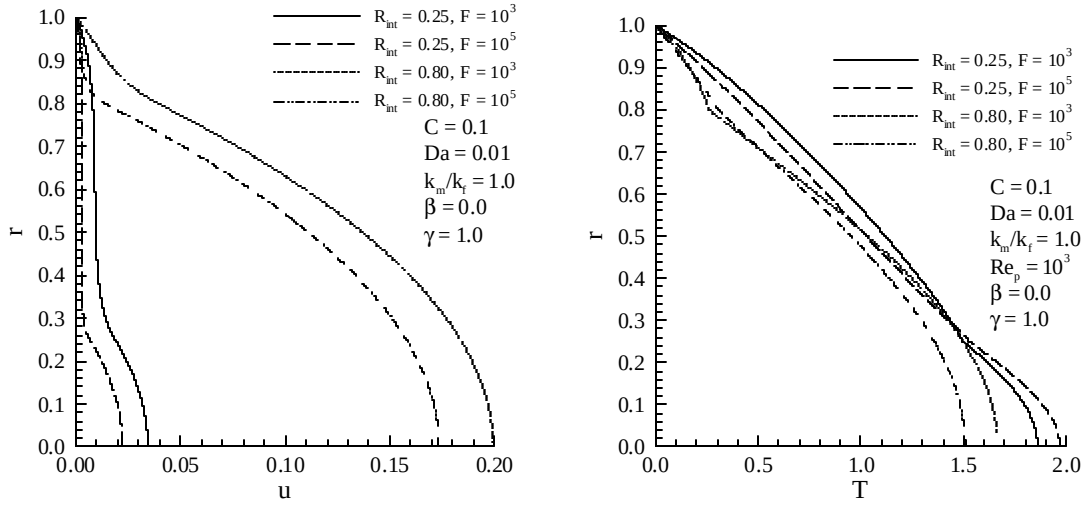

Figure 14a **Figure 14b**

Figure 14 (a) Velocity and (b) temperature distributions for different values of the thickness of porous medium and Forchheimer coefficient for the case of an isoflux wall

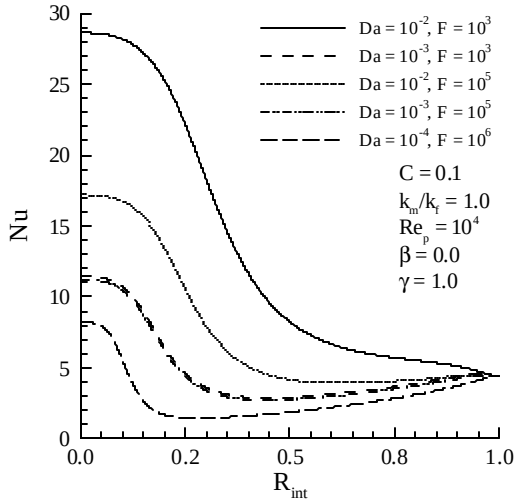

Figure 15 Dependence of the Nusselt number on the thickness of the porous medium for the case of an isoflux wall

4.4.2 Constant Wall Temperature

Figure 16 depicts the change of the Nusselt number with the Reynolds number. To compare the numerical simulations with the experimental data of Verschoor and Schuit [25], the parameter values used in this figure are the same as in Verschoor and Schuit [25]: $\mathrm{Da} = 1.867 \times 10^{-4}$, $\mathrm{F} = 106.27 \times \mathrm{Re}_p$, $\mathrm{k}_m / \mathrm{k}_f = 5.481$, $\mathrm{Pr} = 0.7$, $\mathrm{R}_{int} = 0.0$, $\varepsilon = 0.412$, and $\gamma = \frac{1}{\sqrt{\varepsilon}}$. The results are similar to those for the isoflux case. The numerical results slightly overpredict the rate of increase of the Nusselt number when the Reynolds number is increased.

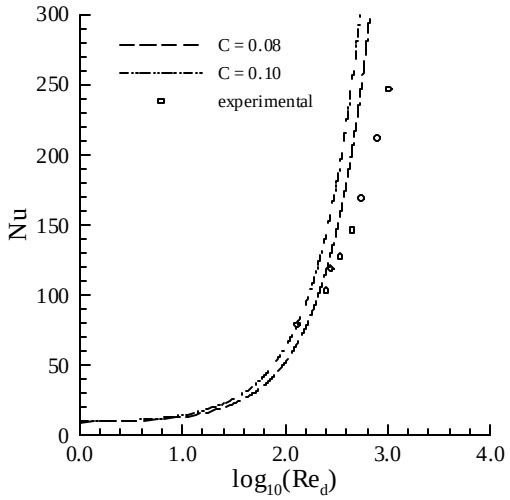

Figure 16 Dependence of the Nusselt number on the particle Reynolds number for the case of an isothermal wall

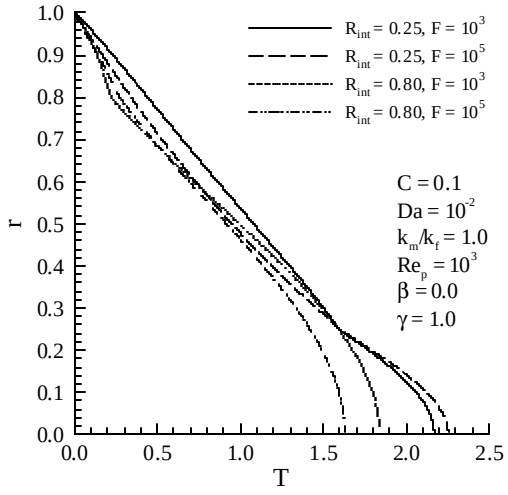

Figure 17 Temperature distributions for different values of the thickness of porous medium and Forchheimer coefficient for the case of an isothermal wall

Figure 17 depicts the temperature distributions in the duct for different values of the Forchheimer coefficient for the isothermal wall. The parameters utilized to compute Fig. 17 are the same as those used to compute Fig. 14 for the isoflux wall case. The velocity distributions corresponding to the temperature distributions shown in Fig. 17 are exactly the same as those for the isoflux wall case, which are shown in Fig. 14a. This is because the velocity distributions do not depend on the boundary condition for the temperature.

The dependence of the Nusselt number on the position of the clear fluid/porous medium interface is shown in Fig. 18. The Nusselt number has the same trend as in the isoflux wall case (Fig. 15), with the only difference being that the value of the Nusselt number in this case is slightly smaller than that in the isoflux case when computing for the same parameter

values. When the whole duct is filled with a clear fluid, the numerically computed value of the Nusselt number is 3.65, which is very close to the value (3.66) given in Bejan [20].

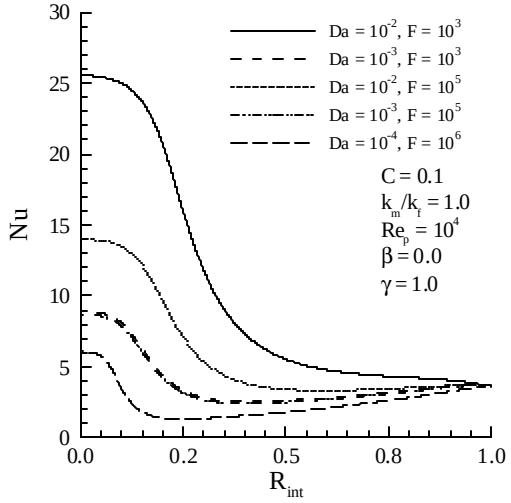

Figure 18 Dependence of the Nusselt number on the thickness of the porous medium for the case of an isothermal wall

4.5 CONCLUSIONS

A numerical simulation of the forced convection in a circular duct partly filled with a Brinkman-Forchheimer porous medium is presented. The thermal dispersion effect is analyzed. Two kinds of thermal boundary conditions (isoflux wall and isothermal wall) are investigated. The trend of the Nusselt number variation with the parameters, such as the

Darcy number, the scaled Forchheimer coefficient, the interface position, and the Reynolds number, is similar for both the isoflux and isothermal boundaries. The Nusselt number increases with an increase of the Reynolds number and does not change monotonically when the Darcy number is of the order of 10^{-3} or less and the Forchheimer coefficient is of the order of 10^{3} or greater. Increasing the Darcy number or decreasing the Forchheimer coefficient causes an increase in the Nusselt number. When the Darcy number is very small, the Forchheimer coefficient has only a weak effect on the Nusselt number.

REFERENCES

1. Amiri, A. and Vafai, K., Analysis of dispersion effects and non-thermal equilibrium, non-Darcian, variable porosity incompressible flow through porous media, *International Journal of Heat and Mass Transfer*, 37:939-954, 1994

2. Nield, D.A., Junqueira, L.M. and Lage, J.L., Forced convection in a fluid saturated porous-medium channel with isothermal or isoflux boundaries, *Journal of Fluid Mechanics*, 322:201-214, 1996

3. Nield, D.A. and Bejan, A., *Convection in Porous Media, 2nd edition*, Springer-Verlag, New York, 1999

4. Vafai, K. and Tien, C.L., Boundary and inertia effect on flow and heat transfer in porous media, *International Journal Heat and Mass Transfer*, 24:195-203, 1981

5. Vafai, K. and Thiyagaraja, R., Analysis of flow and heat transfer at the interface region of a porous medium, *International Journal of Heat and Mass Transfer*, 30:1391-1405, 1987

6. Vafai, K. and Kim, S.J., Fluid mechanics of the interface region between a porous medium and a fluid layer – an exact solution, *International Journal of Heat and Mass Transfer*, 30:1391-1405, 1990

7. Amiri, A., Vafai, K., and Kuzay, T.M., Effects of boundary conditions on non-Darcian heat transfer through porous media and experimental comparisons, *Numerical Heat Transfer, Part A*, 27:651-664, 1995

8. Amiri, A. and Vafai, K., Transient analysis of incompressible flow through a packed bed, *International Journal of Heat and Mass Transfer*, 41:4259-4279, 1998

9. Hsieh, W.H. and Lu, S.F., Heat-transfer analysis of thermally-developing region of annular porous media, *Heat Transfer*, Proceedings of 11th IHTC, 4:447-451, 1998

10. Plumb, O.A., The effect of thermal dispersion on heat transfer in packed bed boundary layers, *Proc. ASME-JSME Thermal Engineering Joint Conference*, 2:17-22, 1983

11. Plumb, O.A. and Whitaker, S., Dispersion in heterogeneous porous media – 1. Local volume averaging and large-scale averaging, *Water Resources Research*, 24:927-938, 1988

12. Plumb, O.A. and Whitaker, S., Dispersion in heterogeneous porous media – 2. Predictions for stratified and two-dimensional spatially periodic system, *Water Resources Research*, 24:927-938, 1988

13. Hong, J.T. and Tien, C.L., Analysis of thermal dispersion effect on vertical – plate natural convection in porous media, *International Journal of Heat and Mass Transfer*, 30:143-150, 1987

14. Hsu, C.T. and Cheng, P., Thermal dispersion in a porous medium, *International Journal of Heat and Mass Transfer*, 33:1587-1597, 1990

15. Poulikakos, D. and Kazmierczak, M., Forced convection in a duct partially filled with a porous material, *ASME Journal of Heat Transfer*, 109:653-662, 1987

16. Vafai, K. and Kim, S.J., Forced convection in a channel filled with a porous medium: an exact solution, *ASME Journal of Heat Transfer*, 111:1103-1106, 1989

17. Ergun, S., Fluid Flow through Packed Columns, *Chem. Engng. Prog.*, 48:89-94, 1952

18. Ochoa-Tapia, J.A. and Whitaker, S., Momentum transfer at the boundary between a porous medium and a homogeneous fluid - I. Theoretical development, *International Journal of Heat and Mass Transfer*, 38:2635-2646, 1995

19. Ochoa-Tapia, J.A. and Whitaker, S., Momentum transfer at the boundary between a porous medium and a homogeneous fluid - II. Comparison with experiment, *International Journal of Heat and Mass Transfer*, 38:2647-2655, 1995

20. Bejan, A., *Convection Heat Transfer*, Wiley, New York, 1984

21. Quinton, J.H. and Storrow, J. A., Heat transfer to air flowing through packed tubes, *Chemical Engineering Science*, 5:245-257, 1956

22. Wakao, N. and Kaguei, S., *Heat and Mass Transfer in Packed Beds*, Gordon and Breach, New York, 1982

23. Kuznetsov, A.V., Analytical investigation of the fluid flow in the interface region between a porous medium and a clear fluid in channels partially filled with a porous medium, *Applied Scientific Research*, 56:53-67, 1996

24. Kuznetsov, A.V., Analytical study of fluid flow and heat transfer during forced convection in a composite channel partly filled with a Brinkman-Forchheimer porous medium, *Flow, Turbulence and Combustion*, 60:173-192, 1998

25. Verschoor, H. and Schuit, G.C.A., Heat transfer to fluids flowing through a bed of granular solids, *Applied Scientific Research*, A2:97-119, 1947

5 INVESTIGATIONS OF SOLIDIFICATION PROCESS OF BINARY ALLOYS -- ALUMINUM-COPPER ALLOY CASTING

ABSTRACT

Segregation and microporosity formation are two important physical phenomena that occur during solidification of binary alloys. The aim of these studies is to investigate the factors influencing microporosity formation and solute redistribution. A three-phase model of the mushy zone which describes the mushy zone as consisting of the solid, liquid, and gas phases is presented to simulate this process. The model accounts for heat, mass, and solute transport as well as microporosity formation. Parametric analyses for different initial hydrogen concentrations, gravity conditions, and values of external pressure at the free surface are carried out. The effects of solute diffusion at both local and global scales are also investigated.

5.1 INTRODUCTION

Solidification of binary alloys has received consistent interest because of its relevance to many fields such as metallurgy, materials processing, purification of metals, crystal growth, and casting [1-14]. In binary alloy solidification, important physical phenomena that determine the quality of castings include solute redistribution and microporosity formation. During this process, solidification occurs within the mushy zone that consists of the liquid,

solid, and gas phases. Solidification shrinkage occurs in the mushy zone because of the density difference between the liquid and solid phases. Interdendritic flow and microporosity formation in the mushy zone compensate for the shrinkage. Interdendritic fluid flow redistributes solute that is rejected by the solidifying dendrites into interdendritic liquid because of the difference in solubility of solute in the liquid and solid phases. This redistribution is called macrosegregation [15]. Modeling this process becomes even more complicated if microporosity formation is taken into account. Microporosity is a common microstructural defect in castings that reduces the mechanical properties of the material. There are two factors leading to microporosity formation in the mushy zone during this process, a local pressure drop due to interdendritic flow and the difference in gas solubility between the liquid and solid phases. With an increase of the volume fraction of solid phase, the gas is expelled into the liquid phase, which leads to increase of thermodynamic pressure of the gas in the liquid phase. When the thermodynamic pressure of the gas is large enough to overcome the local pressure in the mushy zone plus the pressure imposed by surface tension, pore nucleation occurs and the pore grows. This process results in microporosity formation. The appearance of microporosity partially compensates for the shrinkage and thus reduces interdendritic flow [16], which consequently reduces the solute redistribution. In this chapter, an aluminum-rich aluminum-copper alloy is chosen because of the availability of the thermodynamic data needed to construct a microporosity formation model and also because hydrogen is the only gas with noticeable solubility in aluminum and therefore it is the only gas that can contribute to microporosity. The solubility of hydrogen in this alloy heavily

depends on the copper concentration, which means that a microporosity formation model must be coupled with solute transport.

The majority of the models of microporosity formation describe the mushy zone as a two-phase region that consists of the liquid and solid phases. Recent papers by Kuznetsov and Vafai [17, 18] suggest a three-phase model of the mushy zone. These papers were the first that considered the influence of gas bubbles on the transport processes in the mushy zone. The main limitation of [17, 18] was that solidification was assumed to be spatially uniform, which is possible only at a very small cooling rate. Because solidification was assumed to be spatially uniform, no macrosegregation was considered. A recent investigation by Voller and Sundarraj [15] demonstrates that microporosity formation may have a significant effect on inverse segregation because it partially compensates for the shrinkage and thus reduces interdendritic fluid flow, resulting in the reduction of solute transport towards the cooled wall. However, no microporosity formation model was considered in [15]; instead microporosity distributions were obtained by the empirically based friction factor approach.

The major purpose of this chapter is to present a novel three-phase model to simulate the solidification process of binary alloys, which involves a detailed accounting of the coupling of thermodynamics, fluid flow, and solute transport at the local scale of the mushy zone. This makes it possible to theoretically analyze the influence of microporosity formation on the solute redistribution. The effects of several parameters that affect microporosity formation and solute redistribution are investigated.

5.2 PROBLEM DESCRIPTION AND GOVERNING EQUATIONS

5.2.1 Governing Equations

A schematic diagram of the unidirectional solidification process is displayed in Fig. 19. An insulated mold contains the Al-4.1%Cu alloy, initially in the molten state. At the free surface of the alloy a constant pressure of one atmosphere is maintained at all times (Fig. 19a). At the bottom, the constant heat flux is withdrawn, allowing the solidification to proceed unidirectionally from the bottom to the top. Following from Voller and Sundarraj [15], the computational domain is defined by $0 \le x \le X_f$, where X_f is defined as the bottom of the feeder region (Fig. 19b). The region $X_f \le x \le X_{max}$ is occupied by a shrinkage cavity after solidification. During the solidification process this region works as a riser, feeding liquid metal to compensate for the shrinkage. The riser contains macroporosity, whose formation is not considered in this research. This explains why the region $X_f \le x \le X_{max}$ is not included in the computational domain.

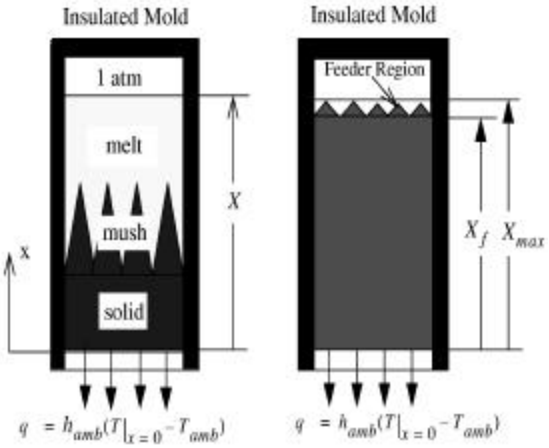

Figure 19 Schematic diagram of the unidirectional solidification process of Al-4.1%Cu

In the formulation of a three-phase model of the mushy zone, the general conservation equations of mass, solute, momentum, and energy, derived in Ganesan and Poirier [19], Poirier et al. [20], and Ni and Beckermann [21] are utilized. These equations express the conservation laws for a local volume in the mushy zone, which in this case contains a mixture of the solid, liquid, and gas phases. For the one-dimensional situation considered here these equations can be simplified as follows.

The mass conservation of the alloy is given by the following:

$$\frac{\partial}{\partial t}(\bar{\rho}) + \frac{\partial(\rho_L u)}{\partial x} = 0 \qquad (1)$$

where t is the time, u is the vertical filtration velocity, x is the vertical coordinate, ρ_L is the density of the liquid phase, and $\bar{\rho}$ is the average alloy density. Equation (1) expresses the mass conservation of the alloy, therefore the expression for $\bar{\rho}$ contains only the terms that account for the densities of the solid and liquid phases:

$$\bar{\rho} = \rho_L \varepsilon_L + \rho_S \varepsilon_S \qquad (2)$$

where ε_L and ε_S are the volume fractions of the liquid and solid phases, respectively, and ρ_S is the density of the solid phase. The term $\rho_g \varepsilon_g$ is not included in the definition of average alloy density. This is because, different from a boiling problem, the gas phase does not consist of aluminum vapor. Instead, the gas phase consists of hydrogen whose density is negligible compared to the density of liquid aluminum. In Eq. (1), it is also assumed that the liquid phase density does not depend on its hydrogen content.

In the definition of the average alloy density, $\overline{\rho}$, as well as in the definitions given below for the average copper density in the mixture, $\overline{\rho C}$, and the average enthalpy per unit volume of the mixture, $\overline{\rho H}$, the equilibrium lever model is utilized, which assumes complete mass diffusion in both the solid and liquid phases in the local averaging volume (at the *local scale*). An alternative formulation could be based on a Scheil model that assumes zero mass diffusion in the solid at the local scale, which will be described in detail later on.

The mass conservation of the solute (copper) is given by the following:

$$\frac{\partial}{\partial t}(\overline{\rho C}) + \frac{\partial(\rho_L u C_L)}{\partial x} = \rho_L D_L \frac{\partial}{\partial x}\left(\varepsilon_L \frac{\partial C_L}{\partial x}\right) \tag{3}$$

where C_L is the mass concentration of copper in the liquid phase, D_L is the diffusivity of copper in the liquid phase (on the *global scale*; between the averaging volumes, the diffusivity of copper in the solid phase is assumed to be zero), and $\overline{\rho C}$ is the average copper density in the mixture. $\overline{\rho C}$, utilizing the lever rule, can be defined as:

$$\overline{\rho C} = \rho_L \varepsilon_L C_L + \rho_S \varepsilon_S C_S \tag{4}$$

where C_S is the mass concentration of copper in the solid phase. Again, Eq. (4) does not contain the gas phase term because there is no copper that is in the gas phase.

The momentum equation is presented as:

$$u = -\frac{K}{\mu_L}\left(\frac{dP}{dx} + \rho_L g\right) \tag{5}$$

where g is the gravitational acceleration, K is the permeability of the mushy zone, P is the local pressure in the mushy zone, and μ_L is the dynamic viscosity of the liquid phase.

The permeability of the mushy zone is calculated, according to the Kozeny-Carman correlation [22], to be:

$$K = \frac{d^2 \varepsilon_L^3}{180(1-\varepsilon_L)^2} \tag{6}$$

where d is the average base diameter of a dendrite. Following from [23], d is assumed to be 10^{-4} m.

Assuming local thermal equilibrium between the liquid, solid, and gas phases in the mushy zone, the conservation of energy for the mixture can be presented as:

$$\frac{\partial \overline{\rho H}}{\partial t} + \frac{\partial(\rho_L c_L u T)}{\partial x} + \frac{\partial(\rho_L u \Delta h)}{\partial x} = \frac{\partial}{\partial x}\left(\overline{k}\frac{\partial T}{\partial x}\right) \tag{7}$$

where $\overline{k}$ is the mixture thermal conductivity, T is the temperature, Δh is the latent heat of solidification, and $\overline{\rho H}$ is the average enthalpy per unit volume of the mixture. $\overline{\rho H}$, for the case of constant specific heats and densities, can be defined as:

$$\overline{\rho H} = (\rho_L c_L \varepsilon_L + \rho_S c_S \varepsilon_S + \rho_g c_g \varepsilon_g)T + \rho_L \varepsilon_L \Delta h \tag{8}$$

where c_L, c_S and c_g are the specific heats at constant pressure of the liquid, solid, and gas phases, respectively, ε_g is the volume fraction of the gas phase (microporosity). Because the term $\rho_g c_g \varepsilon_g$ is much smaller than the two other terms, it is neglected in the computations.

In Eq. (8) ρ_g is the density of the gas phase, which can be determined according to the ideal gas Equation of state:

$$\rho_g = \frac{P_g M_{H_2}}{\tilde{R} T} \tag{9}$$

where M_{H_2} is the molar mass of hydrogen gas, P_g is the pressure of the gas phase, and $\tilde{R}$ is the universal gas constant.

The thermal conductivity of the mixture in Eq. (7) is defined as:

$$\bar{k} = \varepsilon_L k_L + \varepsilon_S k_S + \varepsilon_g k_g \tag{10}$$

where k_L, k_S and k_g are the thermal conductivities of the liquid, solid and gas phases, respectively.

The volume fractions of the liquid, solid, and gas phases must satisfy the following Equation:

$$\varepsilon_L + \varepsilon_S + \varepsilon_g = 1 \tag{11}$$

Because of Eq. (11), the volume fraction of gas phase implicitly influences the continuity equation, Eq. (1). Indeed, as soon as the gas phase appears, the sum $\varepsilon_L + \varepsilon_S$ becomes smaller then unity, which influences the average density of the alloy, $\bar{\rho} = \rho_L \varepsilon_L + \rho_S \varepsilon_S$.

In this model, local thermal and phase equilibrium is assumed in the mushy zone and the equilibrium phase diagram is approximated by the following linear equations:

$$C_L = (T - T_p) / \Gamma \tag{12}$$

$$C_S = \kappa C_L \tag{13}$$

where T_p is the melting temperature of pure aluminum, Γ is the representative liquidus slope on the phase diagram, and κ is the equilibrium partition ratio for copper, C_S / C_L.

Combining Eqs. (4) and (11)-(13), the liquid volume fraction can be defined by the following:

$$\varepsilon_L = \frac{\overline{\rho C} - \rho_S \kappa (1-\varepsilon_g)(T - T_p)/\Gamma}{(\rho_L - \rho_S \kappa)(T - T_p)/\Gamma} \tag{14}$$

The proposed differential governing Eqs. (1), (3), (5), and (7) are valid not only in the mushy zone, but reduce to the correct limits for the liquid and solid regions as well. These equations are thus valid throughout the computational domain. For this reason, no boundary conditions are required for the solid/mushy and mushy/liquid interfaces. Only boundary conditions at the bottom and the top of the computational domain must be specified. These boundary conditions are postulated similarly to [15].

At the bottom of the computational domain, $x = 0$, the boundary conditions are:

$$\overline{k}\frac{\partial T}{\partial x} = q'', \qquad \frac{\partial C_L}{\partial x} = 0, \qquad u = 0 \tag{15}$$

where q'' is the constant heat flux at the bottom;

at the top of the computational domain, $x = X_f$, the boundary conditions are:

$$\frac{\partial T}{\partial x} = 0, \qquad \frac{\partial C_L}{\partial x} = 0, \qquad p = p_{atm} \qquad u = \dot{m}/\rho_L \tag{16}$$

where $\dot{m}$ is the mass flow rate upon entrance to the computational domain from the region occupied by the riser ($X_f \le x \le X_{max}$) that compensates for the shrinkage and p_{atm} is the atmospheric pressure, which is assumed to be 10^5 Pa.

5.2.2 Microporosity Formation Model

There are a number of factors that lead to microporosity formation in aluminum castings. First of all, the solubility of hydrogen in the solid phase is much smaller than that in the liquid phase, so when the volume fraction of the solid phase increases at a given location in the mushy zone, the remaining liquid phase at that location gathers more and more hydrogen as it is being expelled from the solid phase. Therefore, as the volume fraction of the solid phase increases, the pressure of the dissolved hydrogen in the remaining liquid phase also increases. Also, the shrinkage created by a density difference between the liquid and solid must be compensated for by interdendritic fluid flow, whose velocity is proportional to the pressure gradient, according to the Darcy law. The pressure gradient that is required to drive interdendritic fluid flow can be created only by a pressure drop in the mushy zone. Thus the pressure in the mushy zone decreases and does so at a faster rate in the regions of the mushy zone with a large volume fraction of the solid phase because of a smaller permeability.

In summary, as the volume fraction of solid phase increases at a given location in the mushy zone, two processes occur, an increase in pressure of the hydrogen that is dissolved in the liquid phase and a decrease of local pressure in the mushy zone.

The thermodynamic condition for pore nucleation can be expressed by the following:

$$P_g = P + \frac{2\sigma}{r} \tag{17}$$

where P is the local pressure in the mushy zone, obtained from the momentum Eq. (5); P_g is the pressure in the gas phase; r is the radius of the pore; and σ is the surface tension between gas and liquid [24, 25]. The surface tension can be calculated according to the following thermodynamic correlation suggested in [24]:

$$\sigma = 0.868 + 0.721\times10^{-3} C_L + 1.29\times10^{-5} C_L^2 \tag{18}$$

Equation (17) expresses the porosity nucleation condition in terms of pressure. For modeling purposes it is more convenient to express this condition in terms of the hydrogen concentrations in the alloy. Similar to Eq. (4), the average hydrogen density in the mushy zone can be expressed by the following:

$$\overline{\rho C^H} = \rho_S \varepsilon_S C_S^H + \rho_L \varepsilon_L C_L^H + \rho_g \varepsilon_g \times 100 \tag{19}$$

where C_L^H and C_S^H are the mass concentrations of hydrogen in the liquid and solid phases [wt pct], respectively. The factor of 100 is present in the last term of Eq. (19) because the mass concentration of hydrogen in the gas phase is 100 wt pct.

The average mass concentration of hydrogen in the liquid-solid-gas mixture can be then expressed as:

$$\overline{C^H} = \frac{\overline{\rho C^H}}{\rho_S \varepsilon_S + \rho_L \varepsilon_L + \rho_g \varepsilon_g} \tag{20}$$

As long as the amount of hydrogen that can be dissolved in the liquid and solid phases at a given temperature, pressure, and copper concentration is larger than the initial hydrogen concentration (C_{H0}) at this location, no microporosity will form in the mushy zone. This condition is given by the following:

$$\overline{C^{H}_{L+S}} = \frac{\rho_S \varepsilon_S C^{H}_{S} + \rho_L \varepsilon_L C^{H}_{L}}{\rho_S \varepsilon_S + \rho_L \varepsilon_L} > C_{H0} \tag{21}$$

Once the condition given by Eq. (21) is violated, microporosity formation begins in the mushy zone. Following from Huang et al. [26], any hydrogen segregation in the casting is assumed to be negligible. This means that the mass of hydrogen per unit mass of alloy at a given location does not change during the solidification process and that this hydrogen can either remain dissolved in the alloy or be expelled into the gas phase. The volume fraction of microporosity, ε_g, can then be found from the mass balance for hydrogen, which can be expressed as $\overline{C^{H}} = C_{H0}$, or in more detailed form, by the following equation:

$$\frac{\rho_S \varepsilon_S C^{H}_{S} + \rho_L \varepsilon_L C^{H}_{L} + \frac{P_g M_{H_2}}{\approx RT} \varepsilon_g \times 100}{\rho_S \varepsilon_S + \rho_L \varepsilon_L + \frac{P_g M_{H_2}}{\approx RT} \varepsilon_g} = C_{H0} \tag{22}$$

One of the functions involved in Eq. (22) is that of the mass concentration of hydrogen dissolved in the liquid phase, C^{H}_{L}. Poirier et al. [24] suggested to calculate this concentration utilizing the equation for the equilibrium constant (K_{eq}) for the reaction of $\frac{1}{2}H_2(g) = \underline{H}$, which can be presented as:

$$K_{eq} = C_L^H \Big/ \sqrt{P_g} \tag{23}$$

The equilibrium constant can also be expressed in terms of the solubility of hydrogen as:

$$K_{eq} = K_0 S \tag{24}$$

where K_0 has a value of 2.822×10^{-7} and S is the solubility of hydrogen (in cm^3 per 100 g of alloy) in equilibrium with gaseous hydrogen at 1 atm of pressure [24].

The solubility of hydrogen in Al-Cu liquid alloys can be determined using the data published by Opie and Grant [27]. The solubility is thus given by the following:

$$\ln S = -A/T + B \tag{25}$$

where the functions A and B are determined by the local mass concentration of copper in the Al-Cu alloy and are defined by:

$$A = a_0 + a_1 C_L^{1/2} - a_2 C_L + a_3 C_L^{3/2} \tag{26}$$

$$B = b_0 + b_1 C_L^{1/2} - b_2 C_L + b_3 C_L^{3/2} \tag{27}$$

where $a_0 = 5871$, $a_1 = 826.4$, $a_2 = 125.4$, $a_3 = 1.437$, $b_0 = 6.033$, $b_1 = 0.7007$, $b_2 = 0.1859$, $b_3 = 0.01032$.

The mass concentration of the hydrogen that is dissolved in the solid phase (C_H^S, also involved in Eq. (22)) can be related to that in the liquid phase by the equilibrium partition ratio κ_H, which is equal to 0.069 in this case. This relation is given by:

$$C_S^H = \kappa_H C_L^H \tag{28}$$

Solving Eq. (22) for ε_g and accounting for Eqs. (11), (23), (24), and (28), the volume fraction of microporosity can be expressed by the following:

$$\varepsilon_g = \frac{C_{H0}[\rho_L \varepsilon_L + \rho_S(1-\varepsilon_L)] - K_0 S\sqrt{P_g}[\rho_L \varepsilon_L + \rho_S(1-\varepsilon_L)\kappa_H]}{(\rho_S - \frac{P_g M_{H_2}}{\tilde{R}T})C_{H0} + (\frac{P_g M_{H_2}}{\tilde{R}T}\cdot 100 - \rho_S \kappa_H K_0 S\sqrt{P_g})} \qquad (29)$$

where the solubility, S, is given in terms of the mass of the copper concentration in the liquid phase (C_L) by Eqs. (25)-(27).

To complete the model, it is necessary to relate the pressure in the gas phase, P_g in Eq. (29), to the local pressure in the mushy zone, P. This relation is given by Eq. (17). The utilization of Eq. (17) requires a model for the radius of a hydrogen pore in order to evaluate the term that involves the surface tension. It is assumed that once the pore has nucleated it will continue to grow until the solidification is complete. The following linear correlation is assumed between the radius of the pore and the volume fraction of the liquid phase:

$$r = r_b + (r_e - r_b)\frac{\varepsilon_L^0 - \varepsilon_L}{\varepsilon_L^0} \qquad (30)$$

where ε_L^0 is the volume fraction of the liquid phase when the gas pore first appears (which depends on the location in the casting); r_b is the pore nucleation radius; and r_e is the radius of the "grown up" pore, when the alloy at the given location has been completely solidified. According to Eq. (17), the pore nucleation radius (r_b) cannot be infinitely small, otherwise the pressure in the gas phase would never overcome the surface tension and the pore would

never nucleate. Following from Emadi et al. [25], it is assumed that r_b and r_e are $10\,\mu m$ and $70\,\mu m$, respectively.

Since the distribution of microporosity depends on the position, an average microporosity in the casting can be characterized by the following parameter:

$$\overline{\varepsilon_g} = (1/X_f)\int_0^{X_f} \varepsilon_g dx \qquad (31)$$

5.3 EFFECTS OF INITIAL HYDROGEN CONCENTRATION, SURFACE TENSION, AND GRAVITY CONDITIONS ON SOLIDIFICATION

Since microporosity formation during solidification processes is associated with a pressure change in the mushy zone, it is influenced by the metallostatic pressure created by the metal above the mushy zone. Therefore, gravity is one of the factors that influence microporosity formation. In microgravity this factor is absent, simplifying the physical picture of microporosity formation. Another factor that will make the results of experiments carried out in microgravity easier to interpret is the absence of microporosity migration, which is unavoidable in standard gravity because of natural convection. Thus microgravity experiments possess the potential for clarifying the current description of the microporosity formation process and for the testing of theoretical models of this process.

The experiments that have been performed thus far under extended microgravity conditions were done aboard a space shuttle with aluminum alloys, utilizing samples prepared by induction melting in a vacuum to reduce the concentration of hydrogen dissolved in the alloy [28]. Therefore these experiments revealed no considerable microporosity after solidification. To take advantage of a microgravity experiment for testing microporosity formation theories it will be necessary to experiment with a number of alloy samples with different initial hydrogen concentrations. Before planning such an experiment it is necessary to carry out a theoretical investigation aimed at predicting what microporosity distributions will look like in microgravity. This investigation will make it possible to plan an optimal experiment and to make full use of its results. Also, the investigation of microporosity formation under conditions of reduced or increased gravity is important to the development of future processing technologies for human operations on extraterrestrial surfaces such as those on the Moon or Mars.

The major focus of this section is to study how variable gravity will affect the microporosity distribution and macrosegregation in the solidification of binary alloys. Macrosegregation and microporosity formation under different gravity conditions are analyzed.

An implicit finite difference method is utilized on a uniform grid to discretize the governing equation. Computations are performed utilizing 10,001 grid points in the x-direction and the time step of 10^{-3} s. The grid independence of the solution is checked by performing a computation with 20,001 grid points.

The convection terms in the governing equations are discretized using upwind finite differences while the diffusion terms are discretized using centered differences. Computations are performed utilizing 10^4 nodal points. When porosity is not included in the calculations, there is no need to solve the momentum equation and a time step of 10^{-2} is enough to avoid instabilities and oscillations. However, when porosity is included in the calculations, oscillations exist for time steps smaller than even 10^{-3} if the momentum equation is solved in a conventional way, despite the implicit finite-difference formulation that is employed. To avoid this instability problem, the governing equations are modified for the numerical purposes. The continuity equation is substituted into the momentum equation, leading to the following second-order differential equation for the pressure:

$$-\rho_S \frac{\partial \varepsilon_g}{\partial t} - \frac{\rho_L}{\mu_L}\left(\frac{dK}{dx}\right)\left(\frac{dP}{dx}\right) - \frac{\rho_L K}{\mu_L}\left(\frac{d^2P}{dx^2}\right) = -\frac{1}{\mu_L}\rho_L^2 g\left(\frac{dK}{dx}\right) - (\rho_L - \rho_S)\frac{\partial \varepsilon_L}{\partial t} \qquad (32)$$

In Eq. (32) the rate of porosity growth, $\frac{\partial \varepsilon_g}{\partial t}$, is expressed as:

$$\frac{\partial \varepsilon_g}{\partial t} = \begin{cases} \frac{\partial \varepsilon_g}{\partial P_g}\frac{\partial P_g}{\partial t} + \frac{\partial \varepsilon_g}{\partial S}\frac{\partial S}{\partial t} + \frac{\partial \varepsilon_g}{\partial T}\frac{\partial T}{\partial t} + \frac{\partial \varepsilon_g}{\partial \varepsilon_L}\frac{\partial \varepsilon_L}{\partial t} + \frac{\partial \varepsilon_g}{\partial C_L}\frac{\partial C_L}{\partial t} & \varepsilon_g > 0 \\ 0 & \varepsilon_g \le 0 \end{cases} \qquad (33)$$

where the first term can be written in terms of $\frac{\partial P}{\partial t}$, utilizing Eq. (17), and the last four terms are treated as source terms.

Property	Value	Unit	Ref.
c_L	1100	$J kg^{-1} K^{-1}$	[15]
c_S	900	$J kg^{-1} K^{-1}$	[15]
C_0	4.1	wt pct	---
d	10^{-4}	m	[23]
D_L	0 (diffusion is neglected)	$m^2 s^{-1}$	---
k_g	0.423	$W m^{-1} K^{-1}$	[29]
k_L	100	$W m^{-1} K^{-1}$	[15]
k_S	200	$W m^{-1} K^{-1}$	[15]
K_0	2.822×10^{-7}	---	[24]
M_{H_2}	2	$g mol^{-1}$	[29]
q"	10^6	$W m^{-2}$	---
$\tilde{R}$	8314	$Pa m^3 / kmol K$	[29]
T_p	933.2	K	[15]
X_b	0.1323	m	[15]
Γ	-3.73	---	[24]
Δh	3.95×10^5	$J kg^{-1}$	[15]
κ	0.173	---	[24]
κ_H	0.069	---	[24]
μ_L	3.00×10^{-3}	$Kg m^{-1} s^{-1}$	[30]
ρ_S	2580 (constant density model)	$kg m^3$	[15]
	$2564.7 + 1.4023 \times C_L$		[31]
ρ_L	2438 (constant density model)	$kg m^3$	[15]
	$2358.5 + 21.685 \times C_L + 7.2914 \times 10^{-2} \times C_L^2 - 7.2351 \times 10^{-4} \times C_L^3$		[31]

Table 1 Data utilized in computations

Another difficulty experienced in these computations is the appearance of a negative local pressure in the mushy zone. This typically occurs when the volume fraction of the liquid phase, ε_L, becomes smaller than 10^{-3} because of a very small permeability of the mushy zone for this range of ε_L (see Eq. (11)). Because a negative local pressure is impossible in real castings, it is assumed that when the local pressure drops to zero at a certain location in the mushy zone, solidification shrinkage in this location is compensated by porosity growth. This prevents any further drop of the local pressure.

The thermophysical properties of the Al-4.1%Cu alloy along with the geometrical data and test conditions are summarized in Table 1. Figures 20-23 are computed for the condition of standard gravity ($g = 9.81 m/s^2$).

Figure 20 shows the effect of surface tension and the initial hydrogen concentration on the microporosity distribution after the solidification of the alloy has been completed. Computations that neglect the surface tension were performed by utilizing a value of zero for σ in Eq. (17). For the case of a low initial hydrogen concentration ($C_{H0} = 10^{-6}$ wt pct) computations accounting for the surface tension predict no microporosity formation in the casting. If the same computations are repeated assuming no surface tension, they predict a small degree (about 0.05%) of microporosity. For a larger initial hydrogen concentration ($C_{H0} = 4 \times 10^{-5}$ wt pct) the same computations predict a much larger volume percent of microporosity (average microporosity is 2.75% and 3.5% for computations with surface tension and with no surface tension, respectively). This shows that surface tension hinders microporosity formation and results in a smaller degree of microporosity in the casting, as is

physically expected. The volume fraction of microporosity increases slightly with an increase in the distance from the bottom of the chill, comes to a maximum, and decreases close to the feeder region. This decrease is because of the good feeding conditions that exist close to the feeder region. For the case where C_{H0} has a value of 4×10^{-5} wt pct the maximum porosity variation along the height of the casting is less than 0.5%, which indicates a very uniform microporosity distribution. According to Fig. 20, the most important parameter that affects the volume percent of microporosity in aluminum castings is this initial hydrogen concentration in the melt, C_{H0}. Melting in a vacuum can efficiently decrease C_{H0} and thus significantly decrease or completely eliminate microporosity.

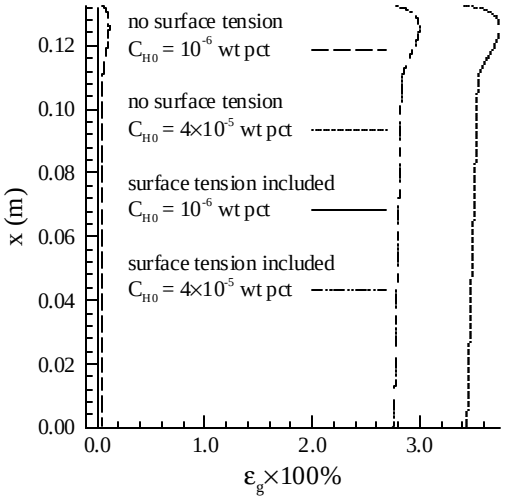

Figure 20 Microporosity distribution for different initial hydrogen concentrations computed accounting for or neglecting the influence of surface tension

The solidification of binary alloys is accompanied by a solute redistribution. In the case of unidirectional solidification, which is considered in this chapter, no natural convection is assumed in the liquid and mushy regions, therefore the solute redistribution is caused solely by the interdendritic fluid flow that compensates for the shrinkage. Microporosity formation compensates for this shrinkage and therefore reduces the interdendritic fluid flow. This logic suggests that the increase in solute concentration at the bottom of the casting (inverse segregation) should be reduced by the formation of microporosity.

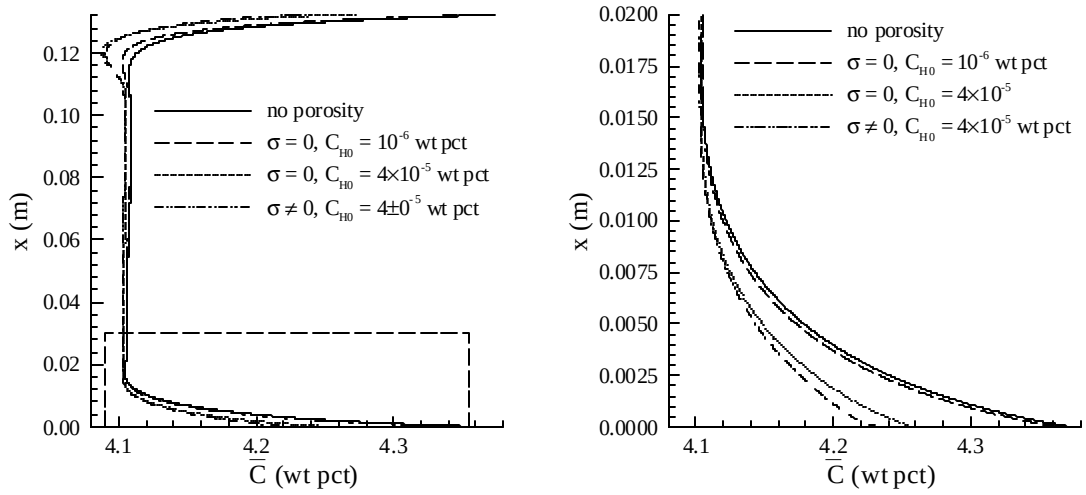

Figure 21a **Figure 21b**

Figure 21 Distributions of the average mass copper concentration with and without microporosity

Figures 21a-b display the distributions of the average mass concentration of copper ($\overline{C} = \overline{\rho C} / \overline{\rho}$) in the casting. The curves displayed in these figures correspond to the microporosity distributions that are displayed in Fig. 20. Figure 21b shows that the maximum copper concentration at x=0 for the case of no microporosity is about 4.38%, while for the case when the degree of microporosity is large ($C_{H0} = 4 \times 10^{-5}$ wt pct, surface tension included) it is only 4.23%. It might seem surprising that for the case of the maximum degree of microporosity ($C_{H0} = 4 \times 10^{-5}$ wt pct, no surface tension) the copper concentration at x=0 is slightly larger than 4.23%. This can be explained, however, by a slight change in solidification dynamics in the mushy zone, which results in larger copper concentration in the liquid phase (C_L) and thus in more copper transport towards the bottom of the casting. Figure 21a shows that the average copper concentration in the computational domain is slightly above the initial copper concentration of 4.1%. This does not mean however, that the mass conservation of copper is violated, because the feeder region (Fig. 19b), which is not included in the computational domain, is heavily depleted of copper at the end of the solidification process. Thus the total mass of copper (in the computational domain plus the feeder region) is conserved.

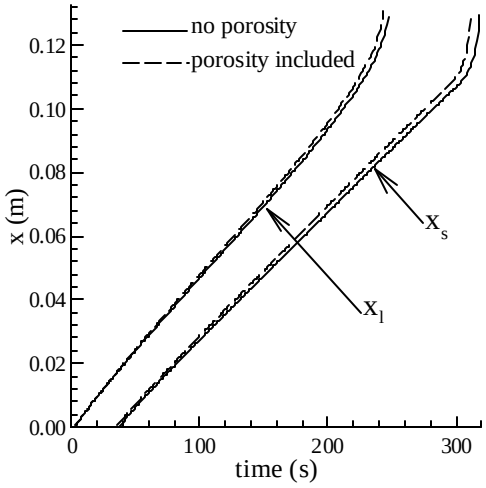

Figure 22 Propagation of the solidus and liquidus fronts with and without microporosity

Figure 22 depicts the effect of microporosity formation on the propagation of the liquidus and solidus fronts. For the dash curve, an initial hydrogen concentration of 4×10^{-5} wt pct was assumed (surface tension effects were accounted for). This figure shows that accounting for the microporosity formation results in slightly faster propagation of the solidus and liquidus fronts. This is because microporosity results in a decrease of the density and specific heat of the alloy per unit volume. Because the heat flux that is removed from the bottom is kept constant, a porous alloy solidifies a little faster than a dense alloy. Figure 22 also shows that the width of the mushy zone remains nearly constant as the solidification process proceeds, except in the upper part of the casting. Once the liquidus line reaches the feeder region, the thickness of the mushy zone decreases until the alloy has been completely solidified. For this reason, feeding conditions in the upper part of the casting are significantly

different from those in the rest of the casting, which explains the differences in the microporosity distribution near the feeder region, displayed in Fig. 20.

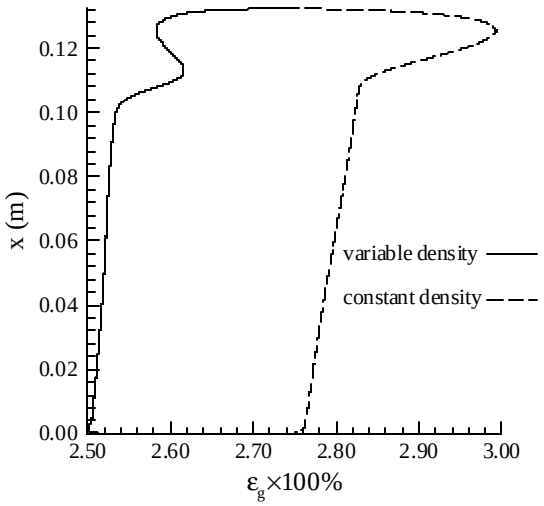

Figure 23 Microporosity distributions computed for constant or variable density models

Figures 20-22 are computed by assuming that the densities of the liquid and solid phases are constant. The experimental investigation by Ganesan and Poirier [31] shows that in practice the liquid and solid densities do change with the solute concentration in an alloy during the solidification process. Figure 23 displays the effect of a variable density model on the microporosity distribution in the casting. Computations are performed for the initial hydrogen concentration of 4×10^{-5} wt pct, accounting for the surface tension effects. From this it is observed that the constant density model overpredicts the degree of microporosity by approximately 0.25 %. The microporosity distribution computed for the variable density

model also displays a different trend at the border with the feeder region. This is because the constant density model assumes that the alloy will always shrink during the solidification process. In the variable density model [31], the liquid density can be larger than that of the solid if the solute concentration in the liquid is large enough, which means that at certain stages of the solidification the shrinkage cannot only be greatly reduced, but the alloy may even expand.

Figures 24a-b depict the porosity and average copper concentration distributions at different gravity conditions for constant densities at the liquid and solid phases. The initial hydrogen concentration utilized for Figs. 24a-b is 4×10^{-5} wt pct. The five different gravitational accelerations utilized in these computations are: 1) $g = 0$ (microgravity); 2) $g = 1.62\,\mathrm{m/s^2}$ (Moon); 3) $g = 3.69\,\mathrm{m/s^2}$ (Mars); 4) $g = 9.81\,\mathrm{m/s^2}$ (Earth, standard gravity); 5) $g = 22.88\,\mathrm{m/s^2}$ (Jupiter). Figures 24a shows that in microgravity the microporosity distribution is very uniform, except in the region close to the feeder. This is because of the changing feeding conditions when the liquidus front approaches the top of the casting. For the greatest gravitational acceleration for which computations were performed ($g = 22.88\,\mathrm{m/s^2}$), the variation of microporosity with the distance from the bottom is very large, which is explained by the large influence of the metallostatic head on the feeding process (see Fig. 29). The effect of gravity is greater for the case with larger initial hydrogen concentration. Figures 24b show that the variations of microporosity caused by changing the gravitational acceleration are not large enough to cause visible changes in the copper redistribution.

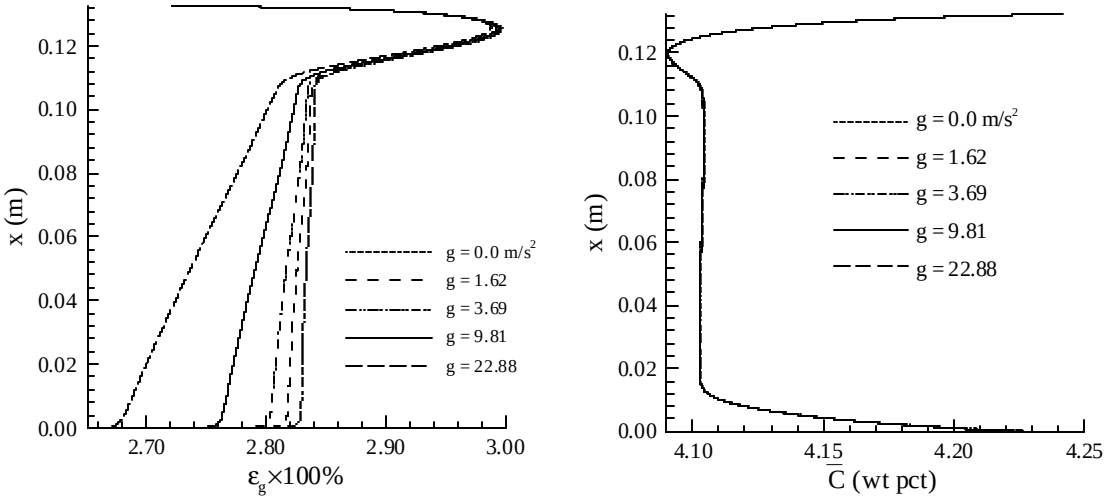

Figure 24a **Figure 24b**

Figure 24 Distributions of (a) microporosity and (b) average copper concentration computed with the initial hydrogen concentration at 4×10^{-5} wt pct

5.4 EFFECTS OF COPPER DIFFUSION AND METALLOSTATIC PRESSURE ON MICROPOROSITY FORMATION

The numerical procedure and parameters utilized in computations are the same as those in the former section. Figures 25-29 are computed assuming constant densities in the solid and liquid phases respectively and an initial hydrogen concentration of $C_{H0} = 4\times10^{-5}$ wt pct. Thermophysical properties of the Al-4.1%Cu alloy along with other parameters utilized in computations are the same as those listed in Table 1.

As mentioned before, the solidification of binary alloys is accompanied by a solute redistribution. Figure 25a shows the computed distributions of the average mass concentration of copper **(** $\overline{C} = \overline{\rho C} / \overline{\rho}$ **)** along the height of the casting as well as a comparison with the experimental data obtained by Kato and Cahoon [32]. In the case of unidirectional solidification considered in this section, the solute redistribution is caused by the interdendritic fluid flow that compensates for the shrinkage and also by the diffusion of copper in the liquid phase (copper diffusion in the solid phase is neglected). Because microporosity formation partially compensates for the shrinkage, it reduces the interdendritic fluid flow. As a result, microporosity can decrease convective solute transport during solidification. Figure 25a shows that the average mass concentration that was computed assuming no microporosity formation is slightly larger than that when microporosity formation is accounted for. In Fig. 25a, there is little difference between the curves computed with and without the diffusion of copper in the liquid phase. The difference is more visible in Fig. 25b, which depicts the average mass concentration of copper near the bottom of the casting. Near the bottom, the average copper concentration is much smaller than the initial value of 4.1 wt pct when diffusion is accounted for. It is interesting to note the difference that accounting for diffusion makes in the mathematical formulation of the problem. When performing computations that do not account for diffusion, the species equation reduces to a first-order differential equation and there is no need to utilize a boundary condition at the bottom; whereas when computations are performed that do account for diffusion, the species equation is a second-order differential equation that requires a boundary condition at the bottom (given by the second equation in Eq. (15)).

Figures 25a-b show that accounting for the diffusion of copper in the liquid phase affects the copper redistribution only near the bottom of the computational domain, in the thin diffusion boundary layer. The mechanism of formation of the diffusion boundary layer was first described in Schneider and Beckermann [33]. When metal in contact with the cooled wall is in the mushy state, intensive cooling from the wall leads to a strong positive temperature gradient in the mushy region. Because the temperature and liquid concentration in the mushy zone are coupled through Eq. (12) and the value of Γ is negative, this positive temperature gradient causes a negative concentration gradient in the interdendritic liquid. Thus copper concentration in the liquid phase decreases from a maximum at the wall to the initial concentration (4.1 wt pct) outside the mushy zone. This concentration gradient in the liquid phase causes solute diffusion from the wall region towards the inner part of the casting. The wall is assumed to be impermeable for copper diffusion. For this reason, the outflow of the solute from the wall region cannot be compensated for and the interdendritic liquid near the wall has a lower copper concentration than if there were no solute diffusion. The solid phase that forms from this interdendritic liquid is also depleted of solute. This results in a lower average copper concentration in a thin layer near the wall. The width of this diffusion boundary layer is small, due to a large value of the Lewis number, $\mathrm{Le} = k_L / (c_L \rho_L D_L)$ (for Al-4.1%Cu alloy Lewis number can be estimated to be 7.610×10^3).

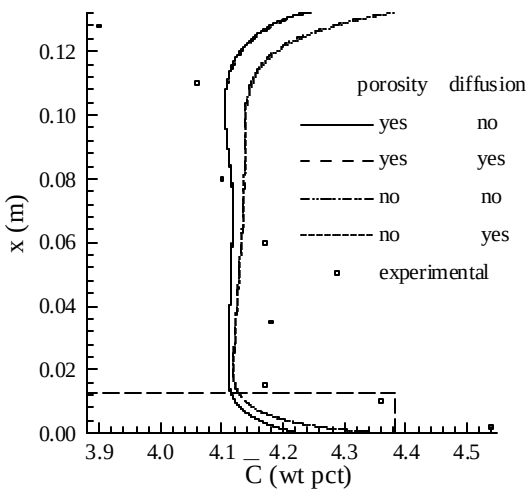

Figure 25a

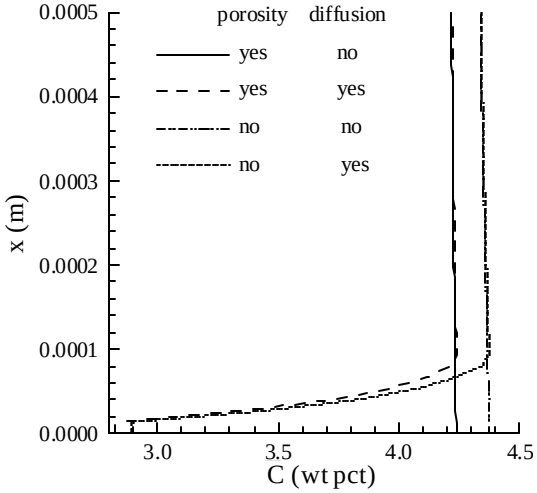

Figure 25b

Figure 25 Distribution of average mass concentration of copper after complete solidification

It should be noted that the computed solute distribution in the upper part of the casting is quite different from that given in experimental data [32]. One possible explanation for this discrepancy is because of the utilization of a lever model to describe the solute redistribution at the local scale. The lever rule predicts that the eutectic fraction will never appear during solidification if the initial solute concentration is below the solid eutectic concentration (5.65 wt pct in the aluminum-copper system). An alternative to lever rule is the so-called Scheil model, which assumes an infinite mass diffusion of the solute in the liquid phase and zero diffusion in the solid phase at the local scale. Voller and Sundarraj [15] have shown that the utilization of the Scheil model results in concentration profiles that are in better agreement with existing experimental data. As mentioned previously, no microporosity formation model

was included in their simulations and microporosity distribution was obtained using an empirically based friction factor approach. Therefore, a combination of the Scheil model with the microporosity formation model will be given later on.

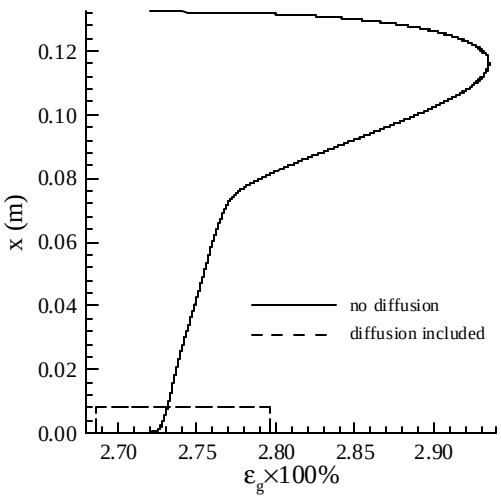

Figure 26a

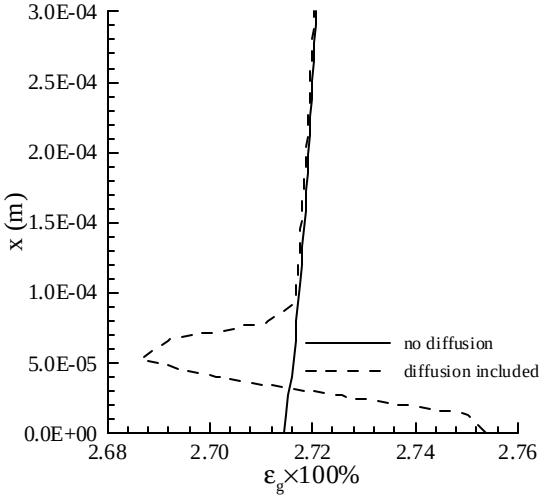

Figure 26b

Figure 26 Microporosity distributions after complete solidification

Figures 26a-b depict the microporosity distributions that were computed accounting for and neglecting copper diffusion in the liquid phase. The porosity distributions are nearly the same for these two cases except in the region very close to the bottom. When diffusion is neglected, the porosity increases smoothly with an increase of the distance from the bottom. When diffusion is accounted for, the porosity distribution goes through a minimum. This is because the solute concentration is one of the factors that have an effect on the porosity (for

example, hydrogen solubility in the liquid phase is a function of C_L, as can be seen from Eqs. (26) and (27)).

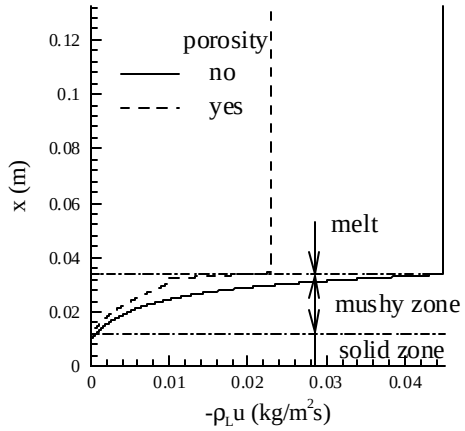

Figure 27 Mass flux distributions at standard gravity at t=80s for accounting for the microporosity formation or neglecting it

Mass transfer during the solidification process is caused by a density difference between the solid and liquid phases. Figure 27 displays the mass flux ($-\rho_L u$) distribution at $t = 80s$, computed with and without microporosity formation. In the region occupied by the melt ($\varepsilon_L = 1$), the mass flux has a constant value. In the mushy zone, the mass flux decreases until it vanishes at the solidus line. The width of the mushy zone for these two cases is about the same. However, the mass flux for the case with no porosity is approximately twice that when porosity formation is accounted for. As mentioned before, solidification shrinkage is

compensated for by interdendritic fluid flow and microporosity growth, therefore the appearance of microporosity reduces the interdendritic fluid flow.

Because the microporosity formation process is associated with a pressure change in the mushy zone, it is affected by metallostatic pressure, created by the metal above the mushy zone. Therefore, gravity is one of the factors that affect microporosity formation. While Figs. 25-27 are computed for conditions of standard gravity, Figure 28 is computed for different values of gravity. Figure 28 shows the local pressure distributions at $t = 80\text{s}$ computed for five different gravitational accelerations: 1) $g = 0$ (microgravity); 2) $g = 1.62\,\text{m/s}^2$ (Moon); 3) $g = 3.69\,\text{m/s}^2$ (Mars); 4) $g = 9.81\,\text{m/s}^2$ (Earth, standard gravity); 5) $g = 22.88\,\text{m/s}^2$ (Jupiter). Figure 28 shows that an increase of gravity increases the gradient of local pressure. In the melt region and in the majority of the mushy zone, the local pressure increases with the distance from the free surface (except in conditions of microgravity). In the part of the mushy zone close to the solid front, the local pressure drops because of a small permeability. The corresponding distributions of microporosity and copper concentration under different gravity conditions are given in Fig. 24.

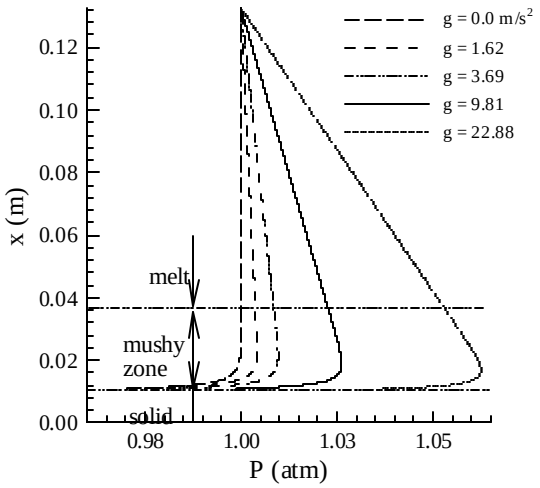

Figure 28 Local pressure distributions at different gravity conditions at t=80s

All of the previous figures are computed accounting for the surface tension term in Eq. (17). Figure 29 depicts the dependence of the average microporosity (defined in Eq. (33)) on gravitational acceleration. Computations are performed both accounting for the surface tension and neglecting it (in the latter case, the zero value for σ was utilized in Eq. (17)). Figure 29 shows that the average microporosity decreases linearly with an increase in the gravitational acceleration for both of these cases. This occurs because of better feeding conditions (larger metallostatic head) for larger gravitational accelerations. When surface tension is neglected however, the predicted degree of microporosity is larger. This is because when there is no surface tension microporosity can nucleate at a smaller pressure drop in the mushy zone. It is interesting that in the range of gravitational accelerations utilized in these computations the two curves depicted in Fig. 29 remain parallel.

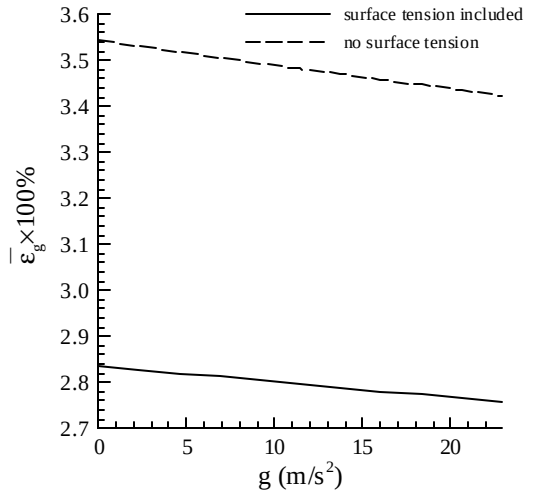

Figure 29 Dependence of average microporosity after complete solidification on gravitational acceleration for accounting for surface tension or neglecting it

5.5 COMPARISON BETWEEN LEVER AND SCHEIL RULES

As mentioned before, microporosity formation is coupled with solute transport. The aim of this section is to investigate the effect of the model of solute diffusion at the local scale (which means at the local scale of the microscopic representative elemental average volume (REV)) on solute transport and microporosity formation during this process. Both the Scheil rule and the lever rule are utilized to describe the solute diffusion at the local scale. The lever rule assumes complete mass diffusion in both the liquid and solid phases. However, the Scheil rule assumes complete mass diffusion in the liquid phase but zero mass diffusion in

the solid phase. Assuming constant properties in the liquid and solid gas, the mixture solute density, utilizing the Scheil and lever rules, can be expressed as, respectively [15]:

$$\overline{\rho C} = \rho_L \varepsilon_L C_L + \int_0^{\varepsilon_S} \rho_S C_S \, d\alpha \tag{34}$$

$$\overline{\rho C} = \rho_L \varepsilon_L C_L + \rho_S \varepsilon_S C_S \tag{35}$$

where C_S is the mass concentration of copper in the solid phase. Equations (34) and (35) do not contain the third term corresponding to the gas phase for the obvious reason (because there is no copper in the gas phase).

In this section, only the region close to the cooling surface is considered. Therefore, the far field boundary condition is utilized at the top. At the bottom, constant heat transfer coefficient is given. The boundary conditions utilized in computations are given as below:

$$\text{At } x = 0, \qquad \bar{k} \left. \frac{\partial T}{\partial x} \right|_{x=0} = h(T|_{x=0} - T_{amb}), \qquad \frac{\partial C_L}{\partial x} = 0, \qquad u = 0 \tag{36}$$

$$\text{At } x = X_b, \qquad T = T_0, \qquad C_L = C_0, \qquad p = p_{ex} \tag{37}$$

where C_0 is the initial copper concentration, h is the heat transfer coefficient at the bottom, P_{ex} is the external pressure imposed at the free surface, T_{amb} is the ambient temperature, and T_0 is the initial temperature of the molten alloy.

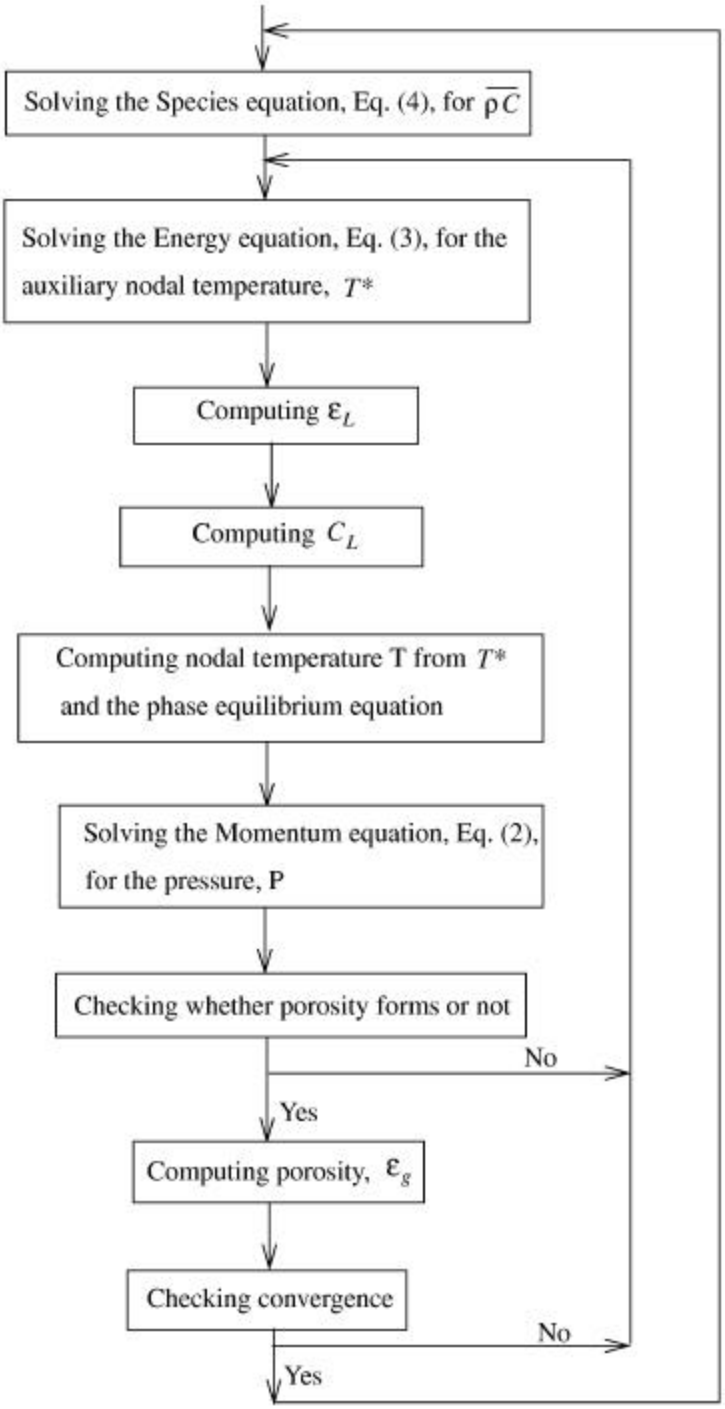

Figure 30 Flow chart of the numerical procedure

The numerical procedure utilized in this section is based on research done by Voller [34] with several modifications introduced because of microporosity formation and three-phase structure of the mushy zone. Since Voller [34] described the scheme in detail, only a flow chart summarizing the procedure is shown in Fig. 30. A grid number of 1000 and a time step of 10^{-2} s are utilized in computations. The height of the computational domain in this section is $X_b = 0.4\text{m}$, the heat transfer coefficient is $h = 5000\text{W}/\text{m}^2\text{s}$, and the initial temperature is $T_0 = 1000\text{K}$. The other thermophysical properties and solidification conditions utilized in the following computations are the same as those listed in Table 1.

Figure 31a depicts distributions of the volume fraction of the liquid phase for different moments of time during the solidification process. The initial hydrogen concentration in these computations is 10^{-5} wt pct. Computations are performed for both the lever and Scheil rules. When the Scheil rule is utilized, some amount of eutectic phase (around 8% in this case) appears. The volume fraction of the liquid phase decreases gradually from unity to 8% as solidification goes on and then the remainder of the liquid phase solidifies at a constant temperature at the eutectic front. This is different from the solidification pattern predicted by the lever rule, in which case the liquid volume fraction decreases smoothly from unity to zero within the mushy zone and no eutectic forms in the alloy with 4.1% initial copper concentration. It can also be observed that the width of the mushy zone is larger if the Scheil rule is utilized when compared to that for the lever rule. This is because the temperature variation over the mushy zone predicted under the Scheil rule is from the eutectic temperature to the liquidus temperature, which is larger than that predicted by the lever rule.

Figure 31b shows distributions of the average copper concentration ($\overline{C} = \overline{\rho C}/\overline{\rho}$) predicted by the Scheil rule and the lever rule, respectively, computed for the same parameter values as Fig. 31a. Both models predict an inverse segregation pattern near the bottom. However, the Scheil rule predicts a heavier inverse segregation and larger average copper concentration in the solidified region than the lever rule. This occurs because the Scheil rule assumes zero mass diffusion of the solute in the solid phase at the local scale. As a result, more copper is rejected by the solidifying dendrites into an interdendritic liquid. The Scheil rule predicts a eutectic concentration of 33.2% once the volume fraction of the liquid phase gets smaller than approximately 8%, while the lever rule predicts no eutectic formation for the initial copper concentration of 4.1%. A jump of the average copper concentration is predicted by the Scheil rule at the eutectic front, which does not exist if the lever rule is utilized. This shows that the diffusion of solute at the local scale has significant effect on solute transport [15]. The effect of this diffusion on microporosity formation is shown in Fig. 31c. When the lever rule is utilized, the predicted microporosity is slightly larger than that predicted under the Scheil rule. This shows that the microporosity formation problem is coupled with solute transport. Microporosity formation partly compensates for the shrinkage and thus reduces the interdendritic flow and inverse segregation. This is the reason for the smaller average copper concentration predicted by the lever rule in Fig. 31b. At the eutectic front, the microporosity distribution predicted under the Scheil rule has an abrupt change, which means microporosity continuously increases after the appearance of eutectic phase until complete solidification. According to the computation, microporosity compensates one fifth of the solidification shrinkage of the eutectic fraction and the rest is compensated by the interdendritic flow.

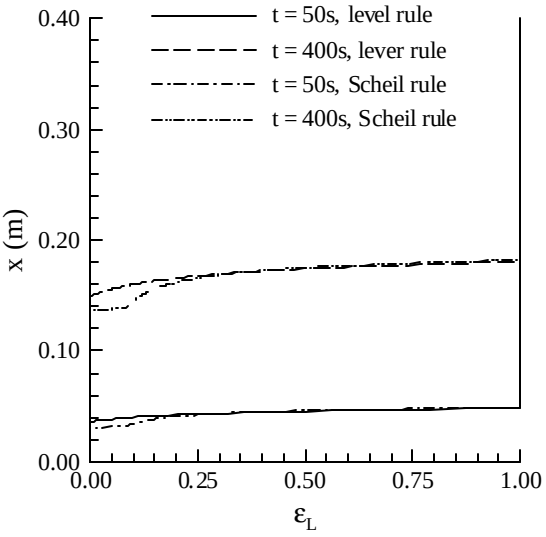

Figure 31a

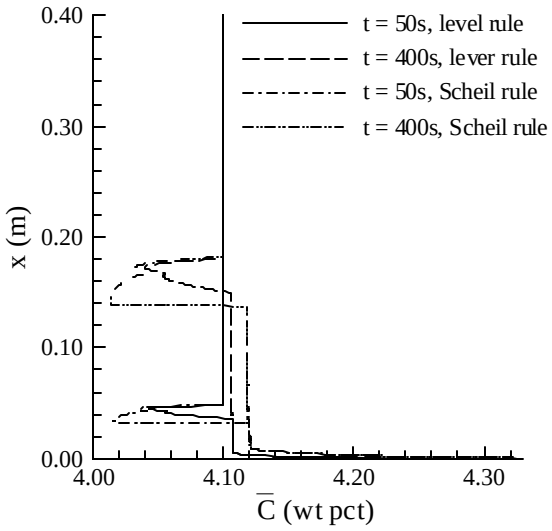

Figure 31b

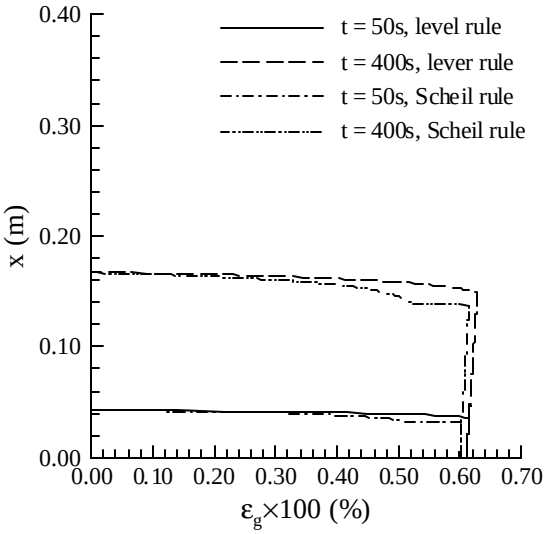

Figure 31c

Figure 31 Distributions of (a) volume fraction of liquid phase, (b) average copper concentration, and (c) microporosity at different moments given by the Scheil and lever models

According to Eq. (15), increased local pressure is one of the factors hindering pore nucleation and growth. There are several ways to influence the local pressure, such as to change the metallostatic head by changing the height of the casting (adding a riser), to change the effective gravitational acceleration (by utilizing the centrifugal force), and to change the external pressure imposed at the free surface. Computations for different effective gravitational accelerations and external pressures are performed and the effect of these factors on microporosity formation is displayed in Figs. 32a and 32b, respectively. The initial hydrogen concentration utilized in computations is 10^{-5} wt pct. Figure 32a shows that the porosity distribution predicted at standard gravity is more uniform and on average it is larger than that predicted for the larger gravitational acceleration corresponding to the gravity on Jupiter. The difference of porosity between $x = 0$ (at the bottom) and $x = 0.07\,\mathrm{m}$ is about 1.7% for standard gravity and about 2.7% for Jupiter gravity. This is because larger gravitational acceleration results in larger metallostatic head, therefore the pressure in the mushy zone stays above critical (critical pressure is the pressure below which microporosity formation occurs) over a larger portion of the mushy zone than for standard gravity. Figure 32b depicts the microporosity distributions at standard gravity for different external pressures. Increasing external pressure significantly decreases porosity, as expected. However, the uniformity of porosity distribution is not affected; increasing external pressure simply shifts microporosity distribution towards smaller values. Therefore, increasing external pressure at the free surface is an effective way to control microporosity formation during the solidification process. It can also be observed that the choice of a particular model

of solute diffusion has a minor effect on predicted microporosity distributions for large external pressures.

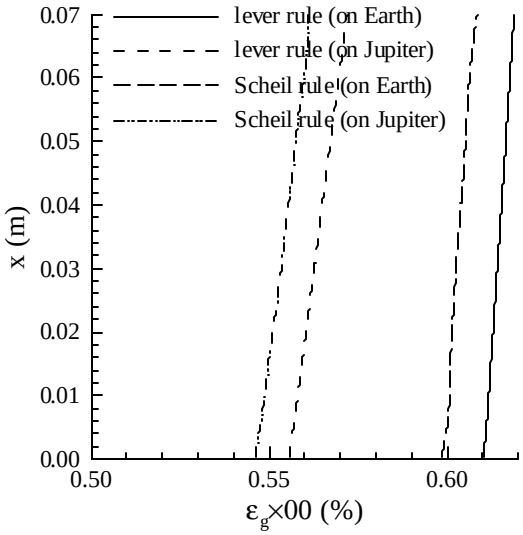

Figure 32a

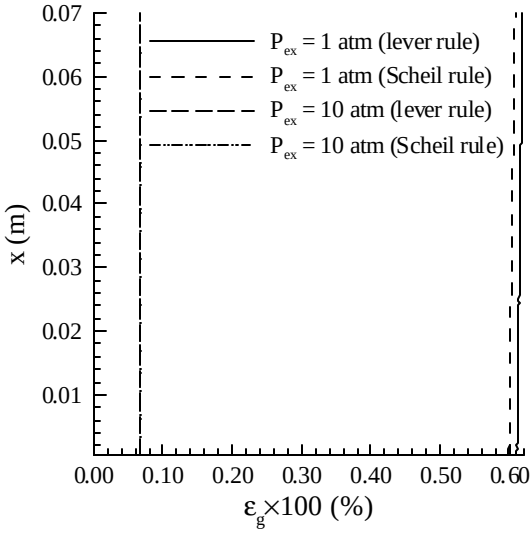

Figure 32b

Figure 32 Effects of (a) gravitational acceleration and (b) external pressure on microporosity distribution

Figure 33a displays the effect of the initial hydrogen concentration in the alloy on microporosity formation. A larger degree of porosity is predicted for larger initial hydrogen concentration, as expected. Therefore, another possible way to control microporosity formation is to control the initial hydrogen concentration in the molten alloy, which can be achieved, for example, by vacuum melting. It can also be seen that the difference between the

predicted degree of microporosity by the Scheil rule and by the lever rule is a little larger for a larger initial hydrogen concentration. This shows that the model of solute diffusion at the local scale has a heavier effect on microporosity formation for larger initial hydrogen concentration. Figure 33b shows distributions of the average copper concentration for different initial hydrogen concentrations predicted by the Scheil and lever rules, respectively. For different initial hydrogen concentrations, distributions of the average copper concentration after complete solidification are almost the same. Comparison of Figs. 33b and 33a indicates that microporosity formation only slightly reduces inverse segregation. However, when comparing the curves obtained by utilizing different models of solute diffusion at the local scale for the same initial hydrogen concentration, the difference is obvious. This shows that the major factors affecting solute transport are the solute diffusion at the local scale as well as solute transport by interdendritic flow. Therefore, choosing a proper model for the solute diffusion at the local scale is crucial for modeling macrosegregation.

Figures 34a-c depict the dependence of the average microporosity in the wall region, $\overline{\varepsilon_g}$, on gravitational acceleration, metallostatic head, and external pressure. Computations are performed for both the Scheil and lever rules for different initial hydrogen concentrations. The average microporosity is computed in the region close to the wall, between $x = 0$ (the bottom) and $x = 0.07\,\mathrm{m}$. Figures 34a-b show that average microporosity decreases linearly with increase in gravitational acceleration and metallostatic head. Compared with Figs. 34a and 34b, Fig. 34c shows that external pressure has heavier effect on average microporosity compared to the metallostatic head and initial hydrogen concentration. The average

microporosity decreases rapidly with increase of external pressure, especially for large initial hydrogen concentration.

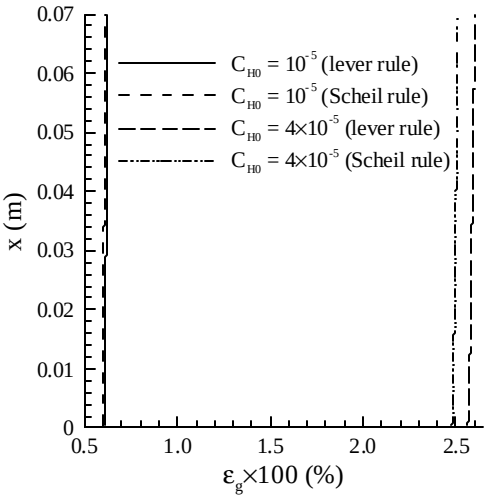

Figure 33a

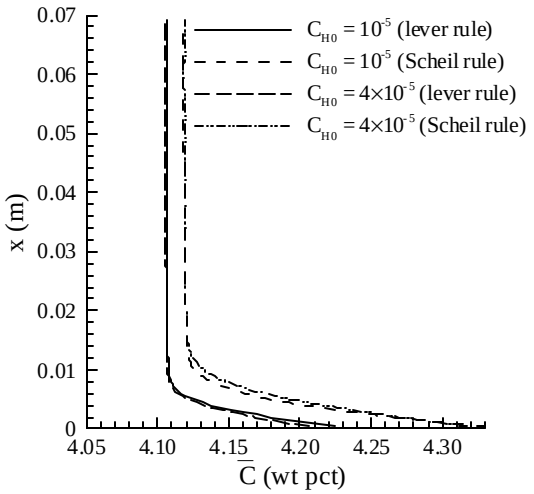

Figure 33b

Figure 33 Distributions of (a) microporosity and (b) average copper concentration for different initial hydrogen concentrations

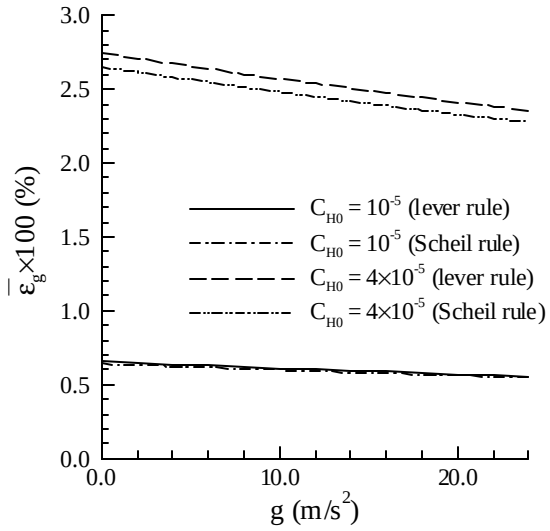

Figure 34a

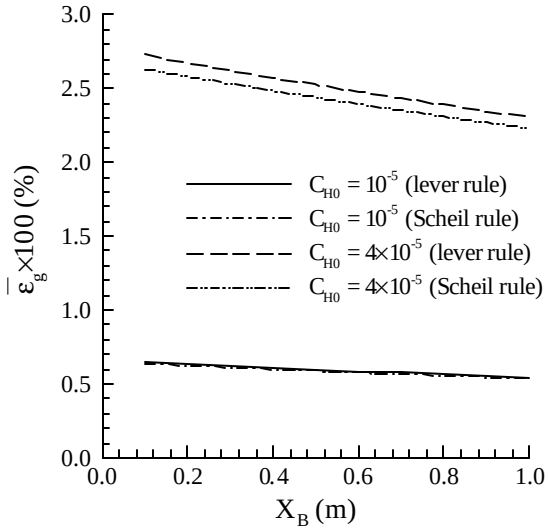

Figure 34b

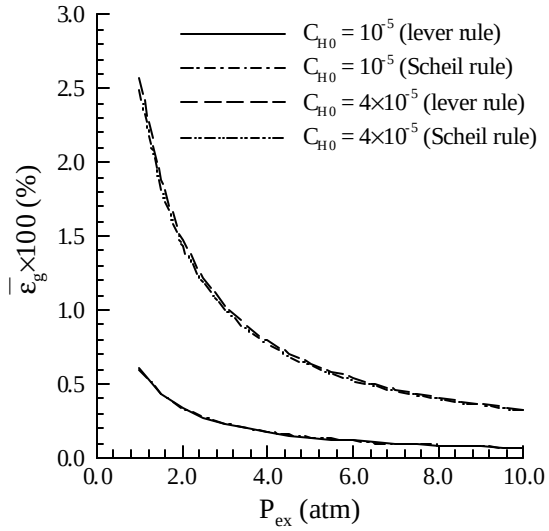

Figure 34c

Figure 34 Dependence of average microporosity on (a) gravitational acceleration, (b) metallostatic head, and (c) external pressure

Figures 31-34 are computed for the initial copper concentration of 4.1%. For alloys with initial copper concentration larger than 5.65%, the eutectic phase appears during solidification even when the lever rule is utilized. Computations with initial copper concentration of 6% are performed to show the effect of the diffusion model on solidification and results are shown in Figs. 35a-c. Figure 35a depicts distributions of the volume fraction of the liquid phase at different moments of time during solidification under the Scheil and lever rules, respectively. The eutectic fraction predicted by the lever rule is around 0.8% for this case, which is much smaller than that predicted by the Scheil rule (around 14%). However, the widths of the mushy zone predicted by these two rules are almost the same. This confirms our explanation of the wider mushy zone predicted by the Scheil rule for initial copper concentration of 4.1% (Fig. 32a). The distributions of average copper concentration and microporosity are shown in Figs. 35b and 35c, respectively. At the eutectic front, an abrupt change in average copper concentration and microporosity is predicted by both the Scheil and lever rules (cf. Figs. 35b and 35c).

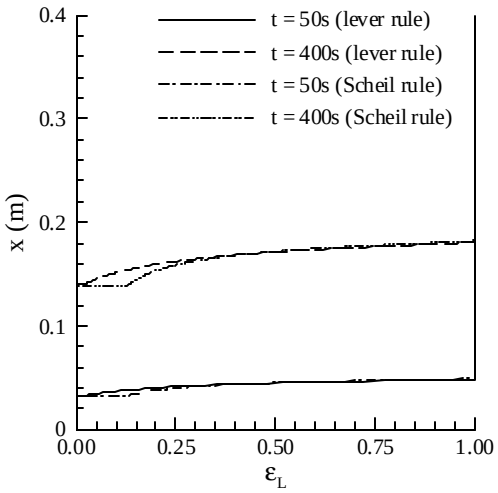

Figure 35a

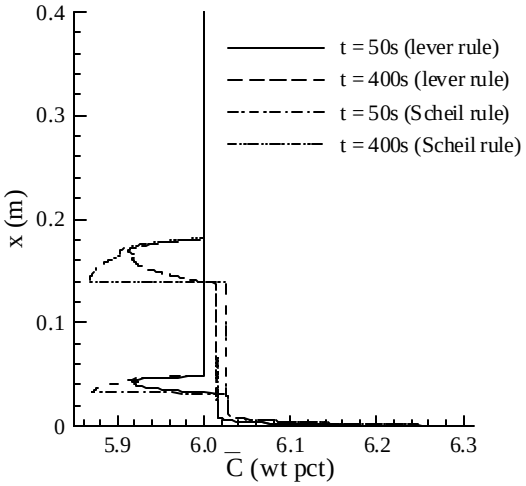

Figure 35b

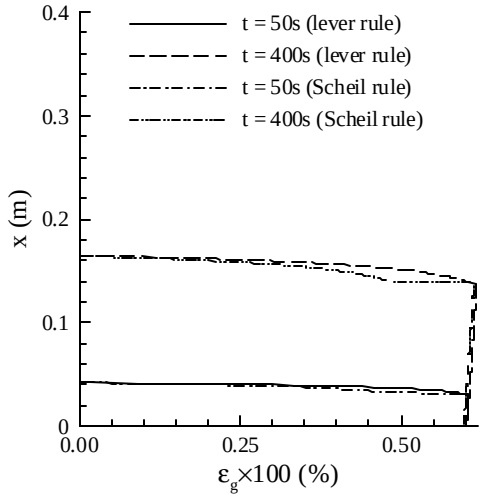

Figure 35c

Figure 35 Distributions of (a) volume fraction of liquid phase, (b) average copper concentration, and (c) microporosity at different moments of time computed utilizing the Scheil and lever rules with initial copper concentration of 6%

5.6 DEPENDENCE OF MICROPOROSITY FORMATION ON THE DIRECTION OF SOLIDIFICATION

Metallostatic head is an important factor in microporosity formation in binary alloys. The aim of this section is to suggest a new approach in the investigation of the effect of gravity on microporosity formation in solidification of binary alloys. Instead of traditional unidirectional solidification from the bottom (cf. Fig. 36(a)), the mold is cooled from the top, as it is schematically shown in Fig. 36(b). In this case solidification proceeds from the top to the bottom. To keep the alloy in contact with the top surface (the chill), the bottom of the mold is designed as a piston that inserts a positive pressure on the liquid alloy from the bottom. The aim of this section is to investigate how, if at all, microporosity formation and solute transport will be affected. If these processes are indeed affected, this new technique can be used in future experimental studies. The comparison of samples solidified "against the gravity" and "along the gravity" can be used as a tool to validate microporosity formation models.

The Scheil model is utilized in this section to model the solute transport on the local scale. The numerical procedure utilized in this investigation is the same as the one used in the former section. From a physical standpoint, the only difference between the processes displayed in Figs. 36a and 36b is the direction of gravity relative to the direction of solidification. Therefore, the same code can be utilized for computing both cases by using different values for gravity, $g = 9.8\,m^2/s$ for the case of Fig. 36a and $g = -9.8\,m^2/s$ for the case of Fig. 36b. Also, solidification in microgravity is modeled, in which case $g = 0$. The

time step of 10^{-2} s and 1,001 nodal points in x direction are utilized. The grid independence of the solution is checked by performing a computation with 2,001 nodal points. The thermophysical properties and geometrical parameters utilized in computations are the same as those in the former section.

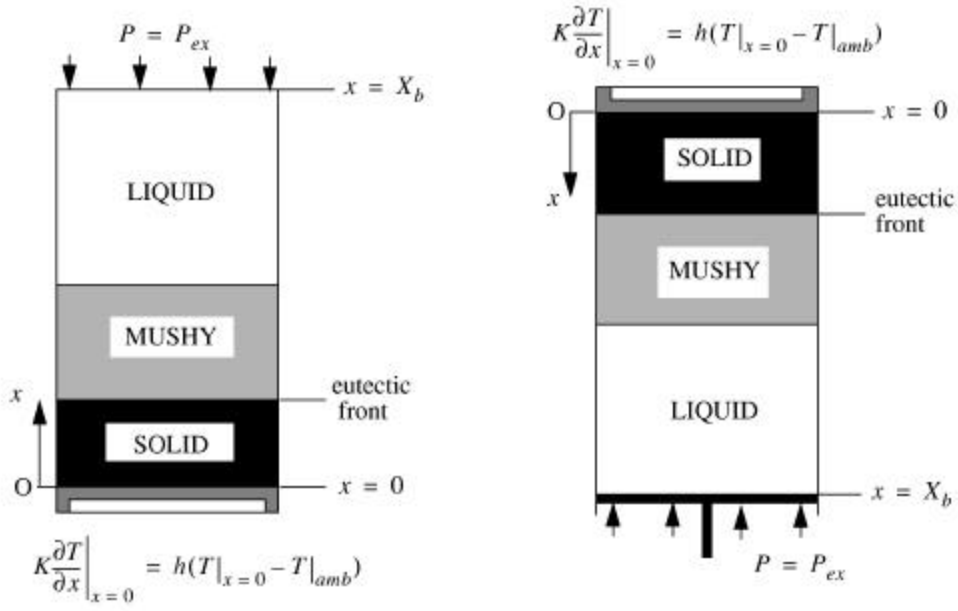

(a) (b)

Figure 36 Schematic diagrams of two methods to carry out unidirectional solidification process: (a) “against the gravity” and (b) “along the gravity”

Figures 37a-d display distributions of the volume fraction of the liquid phase, microporosity, local pressure, and average copper concentration, respectively, at t=300s for three cases:

solidification “against the gravity” (cf. Fig. 36a), “along the gravity” (cf. Fig. 36b), and in microgravity. The initial hydrogen concentration utilized in computations is 10^{-5} wt pct. Figure 37a shows that the distributions of the volume fraction of the liquid phase, for these three different solidification cases computed at the same moment of time, practically coincide with each other. This means that the direction of solidification has almost no effect on solidification rate, as expected. Microporosity distribution, on the contrary, greatly depends on the direction of solidification. For the traditional solidification “against the gravity” (cf. Fig. 36a), microporosity increases with the distance from the chill (from the bottom boundary). For solidification “along the gravity” (cf. Fig. 36b) microporosity decreases with the distance from the chill (from the top boundary). Under microgravity, microporosity distribution is uniform. These trends of microporosity distributions are explained by Fig. 37c, which depicts distributions of the local pressure in the molten region and in the mushy zone. For traditional solidification (cf. Fig. 36a), the local pressure in the molten region increases with the distance from the free surface. This increase continues even in the mushy zone until the volume fraction of the liquid becomes very small. At this point, the local pressure begins to drop to maintain the filtration of interdendritic fluid, which compensates for the shrinkage. Since pressure in the mushy zone is one of the factors that hinders pore nucleation, higher local pressure in the mushy zone corresponds to less porosity. Thus, in the case of traditional solidification, microporosity decreases with the distance from the free surface because larger distance corresponds to larger metallostatic head, which translates to larger pressure in the mushy zone. In the case of solidification “along the gravity” (cf. Fig. 36b), an external pressure of 1 atm is imposed by the piston. The pressure

increases with the distance from the chill until it attains its maximum value of 1 atm at the interface with the piston, therefore microporosity decreases with the distance from the chill. For the microgravity case, the pressure distribution is uniform and this explains the uniform distribution of microporosity. The distributions of the average copper concentration displayed in Fig. 37d show no visible dependence on the direction of solidification. This result is unexpected because, in the case of unidirectional solidification, the copper redistribution is mainly caused by the interdendritic fluid flow, which compensates for the shrinkage. Since microporosity partly compensates for the shrinkage, one would expect that a larger microporosity would correspond to a smaller macrosegregation of copper and vise versa. This paradoxical result of practical independence of macrosegregation on microporosity is explained in Fig. 38. Since the easiest way to influence the degree of microporosity is to change the initial hydrogen concentration, Fig. 38 presents computations performed for traditional solidification method (cf. Fig. 36a) for two different initial hydrogen concentrations, 10^{-5} and 8×10^{-5} wt pct.

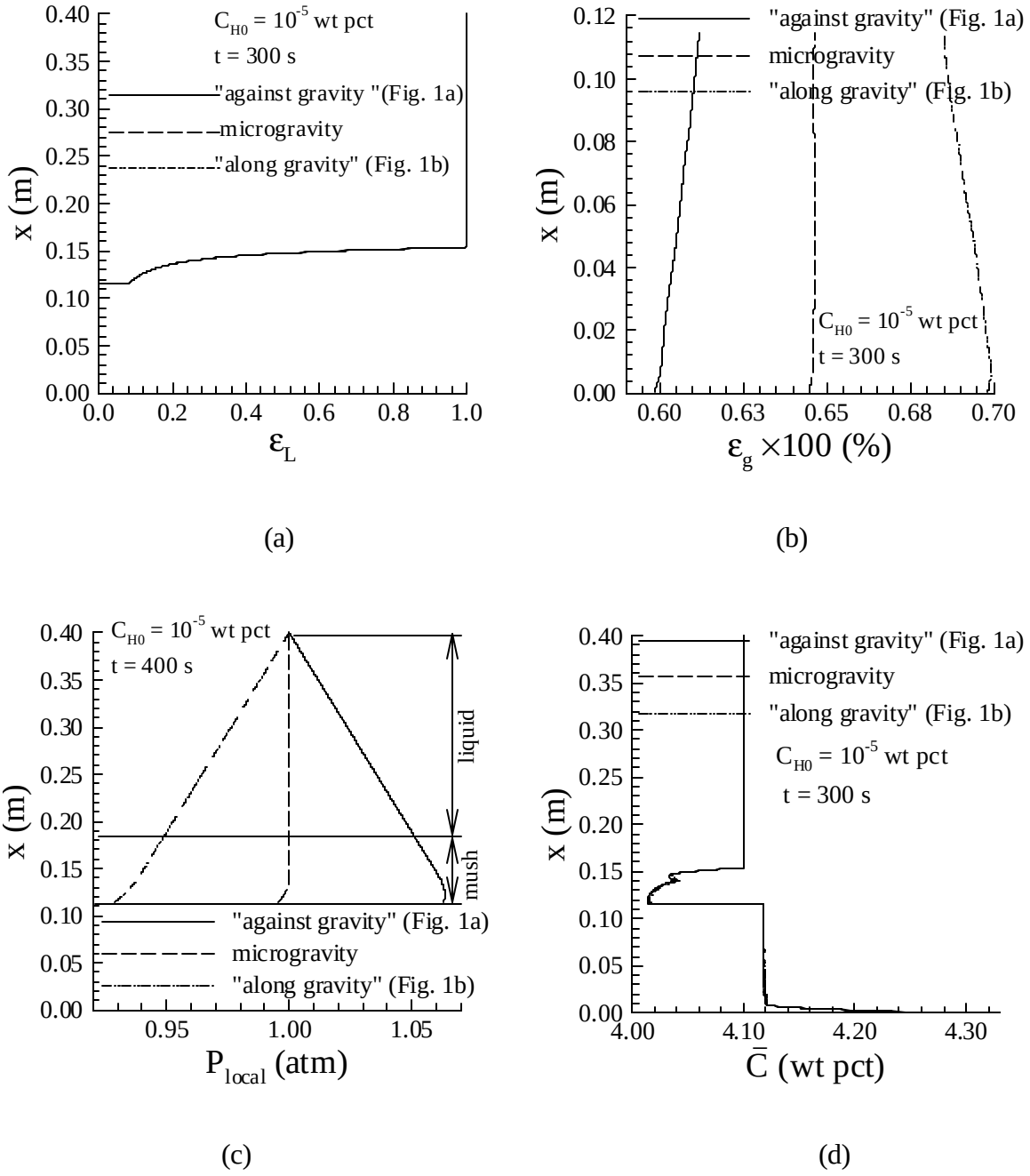

Figure 37 Distributions of (a) volume fraction of liquid phase, (b) microporosity, (c) local pressure, and (d) average copper concentration at t=300s for two opposite directions of solidification and the microgravity case

Figure 38a displays how the volume fraction of liquid phase and microporosity at the bottom (at the chill) change with time. As can be seen, the solidification process is a little faster for a larger initial hydrogen concentration, which is explained by a smaller latent heat of solidification of a REV for a larger degree of microporosity. For a larger initial hydrogen concentration, microporosity nucleation at the bottom occurs at an earlier moment of time. For $C_{H_0} = 10^{-5}$ microporosity nucleation starts when ε_L equals approximately 0.26 while for $C_{H_0} = 8 \times 10^{-5}$ nucleation starts almost simultaneously with the beginning of solidification, quickly attains an almost constant value, and then slightly increases as the eutectic front passes through the REV. The effect of microporosity on the mass flux ($\rho_L u$) and average copper concentration ($\overline{C}$) is shown in Fig. 38b. Since the degree of microporosity for $C_{H_0} = 8 \times 10^{-5}$ is very large (about 5%), it seems logical to expect that for this initial hydrogen concentration microporosity growth will compensate most of the shrinkage (which is about 5.5%). This must lead to almost no macrosegregation of copper and the average copper concentration at the bottom is therefore expected to be close to its initial value in the molten alloy (4.1 wt pct). However, Fig. 38a shows that the shrinkage and microporosity growth are not synchronized. Microporosity grows very fast in the beginning of solidification of the REV (cf. Fig. 38a), while shrinkage is linearly correlated to the change of the volume fraction of the liquid phase. The mass flux for $C_{H_0} = 8 \times 10^{-5}$ is positive in the beginning of solidification, which means that microporosity completely compensates for the shrinkage and even pushes molten alloy upwards, out of the REV. However, after a short period of intensive growth, microporosity comes to a steady state and at a later stage of solidification

shrinkage is compensated by interdendritic fluid flow, which transports copper into the REV. It should be noted that, in the beginning of solidification of the REV, the copper concentration in the interdendritic liquid is still low and, therefore, whether shrinkage is compensated by interdendritic fluid flow or by microporosity growth is not a concern. At a later stage of solidification of REV, when copper concentration in interdendritic liquid becomes large, microporosity has already attained the steady state and therefore does not influence the copper transport. This explains why the average copper concentration at the bottom is about 4.43 wt pct, much larger than its initial value of 4.1 wt pct in the molten alloy, for both small and large initial hydrogen concentrations.

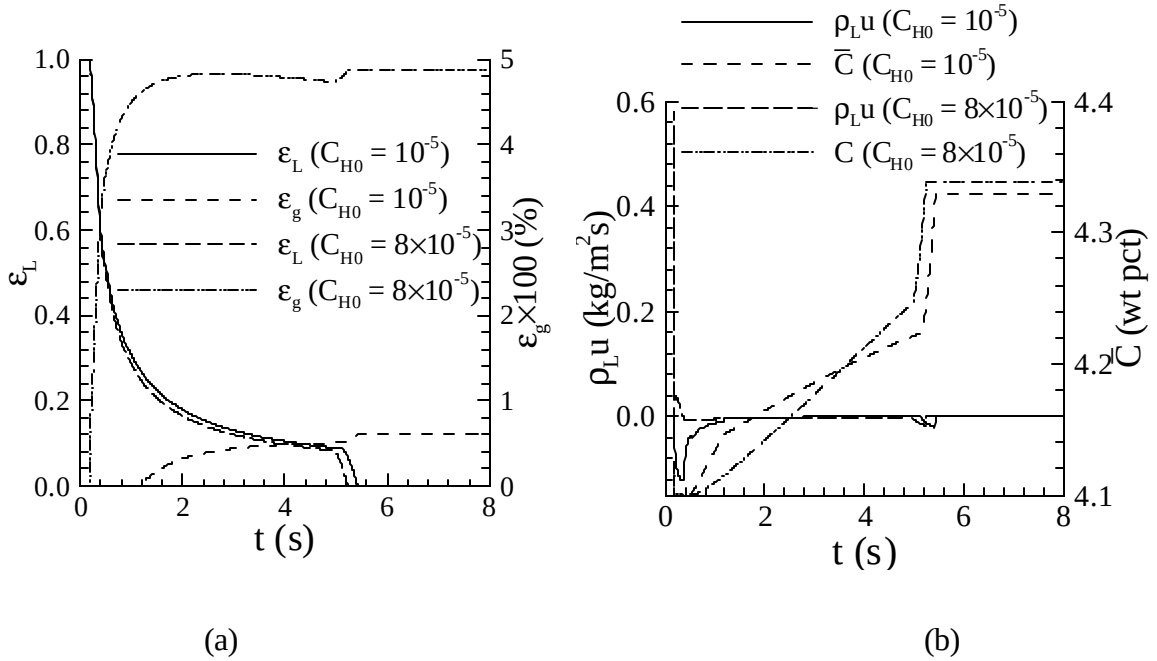

Figure 38 Time dependence of (a) the liquid fraction and microporosity and (b) mass flux and average copper concentration at the bottom for traditional unidirectional solidification

5.7 CONCLUSIONS

A three-phase model of the mushy zone, which accounts for the influence of microporosity on the transport processes in the mushy zone, is suggested. The effects of several factors on microporosity formation and solute transport, such as initial hydrogen concentration, effective gravitational acceleration, external pressure, and models of solute diffusion at the local scale, are investigated. The model of solute diffusion at the local scale has a significant effect on solute transport and microporosity formation. This is because the solubility of hydrogen in an aluminum copper alloy heavily depends on copper concentration and the Scheil rule always predicts some eutectic formation during solidification, but this does not happen with the lever rule if the initial solute concentration is less than 5.65% [15]. However, unless microporosity is very large, microporosity formation has a minor effect on macrosegregation. This is because the degree of porosity formed during this process is typically small and it does not completely compensate for the shrinkage. Therefore, the major factors that influence macrosegregation are the solute diffusion at the local scale and the interdendritic flow. Numerical simulations show that the initial hydrogen concentration is the major parameter that affects the degree of microporosity in aluminum castings. Computational results also reveal that in microgravity conditions microporosity distribution is uniform throughout the casting, except in the region close to the feeder. Under increased gravity, microporosity significantly increases with the distance from the cooled wall, which is explained by the reduction of the metallostatic head and thus worsening feeding conditions in the upper part of the casting. Average microporosity linearly decreases when the gravitational acceleration or the external pressure increases. The obtained results suggest that

effective ways to control microporosity are to increase external pressure at the free surface and to decrease initial hydrogen concentration in the molten alloy.

REFERENCES

1. Bennon, W.D. and Incropera, F.P., A continuum model for momentum, heat and species transport in binary solid-liquid phase changes systems - I. Model formulation, *International Journal of Heat and Mass Transfer*, 30(10):2161-2170, 1987

2. Bennon, W.D. and Incropera, F.P., A continuum model for momentum, heat and species transport in binary solid-liquid phase changes systems - II. Application to solidification in a rectangular cavity, *International Journal of Heat and Mass Transfer*, 30(10):2171-2187, 1987

3. Voller, V.R., Brent, A.D., and Prakash, C., The modeling of heat, mass and solute transport in solidification systems, *International Journal of Heat and Mass Transfer*, 32(9):1719-1731, 1989

4. Lazaridis, A.A., A numerical solution of the multi-dimensional solidification (or melting) problem, *International Journal of Heat and Mass Transfer*, 13:1459-1477, 1970

5. Kuznetsov, A.V., Investigation of the coupled heat transfer, fluid flow and the solute transport during the strip casting process, *International Journal of Heat and Mass Transfer*, 40(12):2949-2941, 1997

6. Pappaz, M. and Voller, V., Modeling of micro-macrosegregation in solidification processes, *Metallurgical Transactions A*, 21A:749-753, 1990

7. Bianchi, Marcus V.A. and Viskanta, R., Gas segregation during solidification processes, *International Journal of Heat and Mass Transfer*, 40(9):2035-2043, 1997

8. Voller, V.R., A similarity solution for the solidification of a multicomponent alloy, *International Journal of Heat and Mass Transfer*, 40(12):2869-2877, 1997

9. Lee, S.L. and Tzong, R.Y., Latent heat method for solidification process of a binary alloy system, *International Journal of Heat and Mass Transfer*, 38(7):1237-1247, 1995

10. Swaminathan, C.R. and Voller, V.R., Towards a general numerical scheme for solidification system, *Int. J. Heat Mass Transfer*, Vol. 40, No. 12, pp. 2859-2868, 1997

11. Huang, H., Suri, V.K., Hill, J.L. and Berry, J.T., Issues in thermal contact and phase changes in porosity prediction, *Journal of Engineering Materials and Technology*, 115:2-7, 1993

12. Viswanathan, S., Sikka, V.K., and Brody, H.D., Using solidification parameters to predict porosity distributions in alloy casting, *Jom-Journal of the Minerals Metal and Materials Society*, 44(9):37-40, 1992

13. Piwonka, T.S. and Flemings, M.C., Pore formation in solidification, *AMS-AIME Trans.*, 236:1157-1165, 1966

14. Devies, V. de L., Feeding range determined by numerically computed heat distribution, *AFS Cast Metals Research Journal*, 11:33-44, 1975

15. Voller, V.R. and Sundarraj, S., A model of inverse segregation: the role of microporosity, *International Journal of Heat and Mass Transfer*, 38(6):1009-1018, 1995

16. Xiong, M. and Kuznetsov, A.V., Numerical modeling of microporosity formation in aluminum-rich aluminum-copper alloys in microgravity conditions, *Proceedings of ASME Heat Transfer Division 2000,* ASME International Mechanical Engineering Congress and Exposition, Orlando, Florida, November 5-10, 2000, HTD, 366(1):167-177

17. Kuznetsov, A.V. and Vafai, K., Development and investigation of three-phase model of the mushy zone for analysis of porosity formation in solidifying castings, *International Journal of Heat and Mass Transfer*, 38:2557-2567, 1995

18. Kuznetsov, A.V. and Vafai, K., Comparison between the two- and three-phase models for analysis of porosity formation in aluminum-rich castings, *Numerical Heat Transfer, Part A*, 29:859-867, 1996

19. Ganesan, S. and Poirier, D.R., conservation of mass and momentum for the flow of interdentritic liquid during solidification, *Metallurgical Transactions B*, 21:173-181, 1990

20. Poirier, D.R., Nandapurkar, P.J., and Ganesan, S., The energy and solute conservation equations for dendritic solidification, *Metallurgical Transactions B*, 22:889-900, 1991

21. Ni, J. and Beckermann, C., A volume averaged two-phase model for transport phenomena during solidification, *Metallurgiccal Transactions B*, 22:349-361, 1991

22. Beckermann, C. and Viskanta, R., Double-diffusive convection during dendritic solidification of a binary mixture, *PhysicoChemical Hydrodynamics*, 10:195-213, 1988

23. Asai, S. and Muchi, I., Theoretical analysis and model experiments on the formation mechanism of channel-type segregation, *Trans. Iron Steel Inst. Japan*, 18:90-98, 1978

24. Poirier, D.R., Yeum, K., and Maples, A.L., A thermodynamic prediction for microporosity formation in aluminum-rich Al-Cu alloys, *Metallurgical Transactions*, 18A:1979-1988, 1987

25. Emadi, D, Gruzleski, J.E., and Toguri, J.M., The effect of Na and Sr modification on surface tension and volumetric shrinkage of A356 alloy and their influence on porosity formation, *Metallurgical Transactions*, 24B:1055-1063, 1993

26. Huang, J., Mori, T., and Conley, JG, Simulation of microporosity in modified and unmodified A356 alloy castings, *Metallurgical Transaction*, 29B:1249-1260, 1998

27. Opie, W.R. and Grant, N.J., Hydrogen solubility in aluminum and some Aluminum alloys, *Trans. AIME., Journal of Metals*, 188:1237-1241, 1950

28. Stefanescu, D.M., Juretzko, F.R., and Dhindaw, B.K., Particle engulfment and pushing by solidifying interfaces: Part II. Microgravity experiments and theoretical analysis, *Metallurgical Transactions*, 29A:1697-1706, 1998

29. Mills, A.F., *Heat Transfer (2nd ed.)*, Prentice Hall, Upper Saddle River, 1999

30. Iida, T. and Guthrie, R.I.L., *The Physical Properties of Liquid Metals*, Clarendon Press, Oxford, 1988

31. Ganesan, S. and Poirier, D.R., Densities of aluminum-rich aluminum-copper alloys during solidification. *Metallurgical Transactions*, 18A:721-723, 1987

32. Kato, H. and Cahoon, J.R., Inverse segregation in directionally solidified Al-Cu-Ti Alloys with equiaxed grains, *Metallurgical Transactions*, 16A:579-587, 1985

33. Schneider, M.C. and Beckermann, C., A numerical study of the combined effects of microsegregation, mushy zone permeability and flow, caused by volume contraction and thermosolutal convection, on macrosegregation and eutectic formation in binary alloy solidification, *International Journal of Heat and Mass Transfer*, 28:3455-3473, 1995

34. Voller, V.R., A numerical scheme for solidification of an alloy, *Canadian Metallurgical Quarterly*, 37(3-4):169-177, 1998

6 NUMERICAL INVESTIGATION ON DIP COATING WITH LIQUID CARBON DIOXIDE

ABSTRACT

A numerical investigation of a novel high-pressure dip coating process with liquid carbon dioxide utilized as a solvent is presented. A mathematical model of this dip coating process is obtained by extending the classical free meniscus theory to account for the effect of evaporation on the free surface profile and on the final thickness of the coating layer. A finite difference method is utilized to predict the dynamic response of meniscus profiles and the thickness of the film. The effects of evaporation rate, initial solute concentration, withdrawal velocity, and viscosity on the film thickness are investigated. The theory is validated by extensive comparisons with experimental results. Limitations and possible future improvements in the theory are discussed.

6.1 INTRODUCTION

Liquid coating techniques are widely used in industrial processes to produce thin films. Modeling the formation of these films is important to control the deposition process [1]. Commonly either an organic or water based solvent is utilized in these processes. The use of organic solvents in liquid coating processes results in the emission of volatile organic

compounds (VOC), which are harmful to the environment. Similarly, when water based solvents are used large quantities of wastewater are generated, whose cleaning requires complicated and expensive separation equipment [2]. A sensible alternative is the utilization of liquid carbon dioxide in these coating processes [3]. The advantages of using carbon dioxide as a solvent arises from its physical properties near the critical point including sensitivity to temperature and pressure variations. Low viscosity and low surface tension of liquid carbon dioxide is advantages for deposition of thin films. Also, carbon dioxide is easier to separate from coating formulations and it is more environmentally acceptable than organic solvents.

Liquid coating techniques include several different methods, such as free meniscus, spin, pre-metered, and self-metered coating process [2, 4, 5]. Dip coating is one of the most common free meniscus coating techniques. It is used in many industrial processes, such as producing chocolate covered foods, photographic films, galvanization of steels, coating glass plates, and deposition of thin lubricant films on magnetic disks [6-9]. In this chapter, the dip coating process with liquid carbon dioxide is investigated by means of numerical modeling. There are three different schemes of the dip coating process: withdrawal, drainage, and continuous processes. For the purpose of modeling, the withdrawal process is the same as the drainage process. Here the withdrawal/drainage process is considered. The schematic diagram of the process is shown in Fig. 1. From a hydrodynamic standpoint, this is a free surface problem. Considerable work has been done on modeling problems involving free surface [1, 6, 7, 11-21]. However, most of them considered both liquid and gas phases matching at the interface to account for evaporation, which is very complex and time-consuming. Some papers utilized

a quasi-one-dimensional model to describe this problem but neglected evaporation. Hurd and Brinker [19, 20] started from experimental measurements to discuss physical aspects of sol-gel film formation in dip coating process. The effect of evaporation on film thickness was analyzed qualitatively. Effects of solute concentration on properties of the solution were neglected. No detailed numerical procedure and free surface profiles were presented in [19-21].

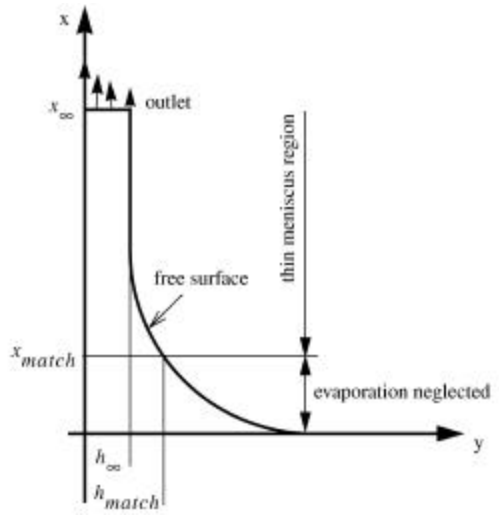

Figure 39 Schematic diagram of dip coating process

6.2 PROBLEM DESCRIPTION

6.2.1 Numerical Model

The governing equations for the dip coating process are obtained assuming a quasi-steady two-dimensional problem. If the thin layer approximation is utilized, the parabolized governing equations can be presented as:

Continuity
$$\frac{\partial(\rho u)}{\partial x}+\frac{\partial(\rho v)}{\partial y}=0 \tag{1}$$

x-momentum
$$\rho\left(u\frac{\partial u}{\partial x}+v\frac{\partial u}{\partial y}\right)=-\frac{dp}{dx}+\frac{\partial}{\partial y}\left(\mu\frac{\partial u}{\partial y}\right)-\rho g \tag{2}$$

Energy
$$\rho c_p\left(u\frac{\partial T}{\partial x}+v\frac{\partial T}{\partial y}\right)=u\frac{dp}{dx}+\frac{\partial}{\partial y}\left(k\frac{\partial T}{\partial y}\right) \tag{3}$$

Utilizing the low curvature approximation, the capillary pressure is determined by the curvature of the free surface [10], therefore, its gradient can be expressed as:

$$\frac{dp}{dx}=-\frac{d}{dx}\left(\sigma\frac{d^2h}{dx^2}\right) \tag{4}$$

Substituting Eq. (4) into Eq. (2) results in:

$$\rho\left(u\frac{\partial u}{\partial x}+v\frac{\partial u}{\partial y}\right)=\frac{d}{dx}\left(\sigma\frac{d^2h}{dx^2}\right)+\frac{\partial}{\partial y}\left(\mu\frac{\partial u}{\partial y}\right)-\rho g \tag{5}$$

The continuity equation, Eq. (1), can be used to eliminate v:

$$\rho v=-\int\frac{\partial(\rho u)}{\partial x}dy \tag{6}$$

Substituting Eq. (6) into the x-momentum equation, Eq. (5), results in:

$$\rho u\frac{\partial u}{\partial x}-\left(\int\frac{\partial(\rho u)}{\partial x}dy\right)\frac{\partial u}{\partial y}=\frac{d}{dx}\left(\sigma\frac{d^2h}{dx^2}\right)+\frac{\partial}{\partial y}\left(\mu\frac{\partial u}{\partial y}\right)-\rho g \qquad (7)$$

For small withdrawal velocities the quadratic terms on the left-hand side of Eq. (7) can be neglected, and this equation can be simplified as:

$$\frac{d}{dx}\left(\sigma(x)\frac{d^2h}{dx^2}\right)+\mu(x)\frac{\partial^2u}{\partial y^2}-\rho(x)g=0 \qquad (8)$$

Here $\sigma(x)$, $\mu(x)$, and $\rho(x)$ are the surface tension, viscosity, and density of the solution (the polymer dissolved in liquid CO_2), respectively. They are functions of the mass fractions of the polymer (C_{pol}) and liquid CO_2 (C_{CO_2}) in the solution:

$$\sigma(x)=\sigma_{pol}C_{pol}+\sigma_{CO_2}C_{CO_2} \qquad (9a)$$

$$\rho(x)=\rho_{pol}C_{pol}+\rho_{CO_2}C_{CO_2} \qquad (9b)$$

$$\mu(x)=\mu_{CO_2}\left(1+\frac{5}{2}\phi_{pol}\right) \qquad (9c)$$

Two models are utilized to describe the solution surface tension. One is the linear model given by Eq. (9a). Another assumes it to be constant which is independent with solute concentration. Eq. (9c) for effective viscosity of the solution follows from Einstein's formula [22]. In eq. (9c), ϕ_{pol} is the volume fraction of the polymer, which can be related to the mass fraction by the following equation:

$$\phi_{pol} = \frac{\rho_{pol} C_{pol}}{\rho_{pol} C_{pol} + \rho_{co_2} C_{co_2}} \qquad (9d)$$

The mass fractions of the polymer and liquid CO_2 can be related by the following equation:

$$C_{pol}(x) = 1 - C_{CO_2}(x) \qquad (10)$$

Equation (8) can be integrated twice with respect to y utilizing the following boundary conditions:

at y=0: $u = U$ (11a)

at y=h(x): $\mu \frac{\partial u}{\partial y} = 0$ (11b)

where U is the withdrawal velocity of the plate.

Integration of Eq. (8) with boundary conditions (11a) and (11b) results in:

$$u = U - \frac{1}{\mu(x)} \left[\frac{d}{dx} \left(\sigma(x) \frac{d^2 h}{dx^2} \right) - \rho(x) g \right] \left(\frac{y^2}{2} - hy \right) \qquad (12)$$

For a steady-state problem, the mass flow rate of polymer through any cross-section must be constant (because polymer does not evaporate). This results in the following requirement:

$$Q_{pol} = \rho(x) \int_0^{h(x)} C_{pol}(x) u dy = \text{ constant} \qquad (13)$$

where Q_{pol} is the mass flow rate of the polymer.

Substituting Eq. (12) into Eq. (13) and integrating it results in:

$$Q_{pol} = \rho(x) C_{pol}(x) \left\{ Uh + \frac{h^3}{3\mu(x)} \left[\frac{d}{dx} \left(\sigma(x) \frac{d^2 h}{dx^2} \right) - \rho(x) g \right] \right\} \qquad (14)$$

Equation (14) must be solved subject to the following boundary conditions:

$$x \to x_\infty \qquad h = \frac{Q_{pol}}{\rho_\infty U C_{pol,\infty}} \qquad (15a)$$

$$x \to x_\infty \qquad \frac{dh}{dx} = -\frac{E}{\rho_\infty U} \qquad (15b)$$

$$x \to x_\infty \qquad \frac{d^2 h}{dx^2} = 0 \qquad (15c)$$

where E is the evaporation rate of CO_2 expressed per unit surface area $\left[\frac{kg}{s\,m^2} \right]$, ρ_∞ and $C_{pol,\infty}$ are the average density of the solution and the polymer concentration at a large height when the flow in the thin film becomes hydrodynamically fully developed, and x_∞ is the vertical position where the flow becomes hydrodynamically fully developed. For very thin films at x_∞, back flow due to gravitational draining can be neglected and Eq. (15b) can be obtained by considering mass balance of carbon dioxide [23]. The choice of x_∞ is discussed later on.

An additional equation is needed to determine the unknown mass flow rate of polymer, Q_{pol}. This condition follows from matching the curvature of the entrained meniscus region with that of the static meniscus region, as was suggested by Landau and Levich [10]. According to Landau and Levich, the matching condition can be expressed as [10]:

$$x \to x_{match} = \sqrt{2}\left(\frac{\sigma_0}{\rho_0 g}\right)^{1/2} \qquad \frac{d^2h}{dx^2} \to \sqrt{2}\left(\frac{\rho_0 g}{\sigma_0}\right)^{1/2} \tag{15d}$$

where σ_0 and ρ_0 are the surface tension and the density of the solution at initial polymer concentration (before the evaporation started), respectively.

For a dip coating process with no evaporation from the free surface, Eqs. (15a-d) provide all boundary conditions that are needed to determine the thickness of the coating layer deposited during this process. This is because for the case with no evaporation this thickness is independent of the choice of x_∞, as long as x_∞ is at least twice as large as the coordinate of the matching point, $x_{match} = \sqrt{2}\left(\frac{\sigma_0}{\rho_0 g}\right)^{1/2}$. However, if evaporation is accounted for, the solution exhibits a heavy dependence on the choice of x_∞. The choice of x_∞ uniquely determines the thickness of the meniscus region at the matching point, h_{match}. Therefore, instead of prescribing a certain value to x_∞, it is more physically sound to prescribe a definite value to the thickness of the meniscus at the matching point. Prescribing this thickness effectively prescribes the size of the thin meniscus region (the region where a thin layer approximation is applicable, cf. Fig. 39). For computational purposes, instead of prescribing the physical size of the meniscus, we will prescribe the ratio of the thin meniscus size to the thickness of the wet coating layer deposited during this process, $\psi = h_{match}/h_\infty$. It should be noted that the size of the meniscus region, h_{match}, can be computed numerically from the model based on full Navier-Stocks equations. However, the theory presented in this

chapter is based on parabolized equations resulting from the thin layer approximation, therefore, this theory requires a value of the parameter ψ as an input parameter.

The dimensionless coordinate and dimensionless film thickness can be introduced as:

$$\hat{x} = \left(\frac{3\mu_0}{\sigma_0} \right)^{1/3} \frac{U^{4/3} \rho_\infty C_{pol,\infty}}{Q_{pol}} x \tag{16}$$

$$\hat{h} = \frac{U \rho_\infty C_{pol,\infty} h(\hat{x})}{Q_{pol}} \tag{17}$$

where μ_0 is the viscosity of the solution before the evaporation started.

Utilizing these dimensionless variables, Eq. (14) can be recast into its dimensionless form as:

$$\frac{\mu_0}{\mu(\hat{x})} \frac{\rho(\hat{x})}{\rho_\infty} \frac{d}{d\hat{x}} \left(\frac{\sigma(\hat{x})}{\sigma_0} \frac{d^2 \hat{h}}{d\hat{x}^2} \right) - \frac{C_{pol,\infty} - \hat{h} \frac{\rho(\hat{x})}{\rho_\infty} C_{pol}(\hat{x})}{\hat{h}^3 C_{pol}(\hat{x})} - \frac{\rho^2(\hat{x}) g}{3\mu(\hat{x})} \frac{Q_{pol}^2}{U^3 \rho_\infty^3 C_{pol,\infty}^2} = 0 \tag{18}$$

Since Q_{pol} is proportional to the withdrawal velocity U to the power $5/3$ (cf. Eq. (22)), the last term in Eq. (18) is small compared to other terms in this equation for small withdrawal velocity U, and this equation can be recast as:

$$\frac{\mu_0}{\mu(\hat{x})} \frac{\rho(\hat{x})}{\rho_\infty} \frac{d}{d\hat{x}} \left(\frac{\sigma(\hat{x})}{\sigma_0} \frac{d^2 \hat{h}}{d\hat{x}^2} \right) - \frac{C_{pol,\infty} - \hat{h} \frac{\rho(\hat{x})}{\rho_\infty} C_{pol}(\hat{x})}{\hat{h}^3 C_{pol}(\hat{x})} = 0 \tag{19}$$

Boundary conditions for Eq. (19) are given by the dimensionless form of equations (15a-c):

$$\hat{x} \to \hat{x}_\infty \qquad \hat{h} = 1 \tag{20a}$$

$$\hat{x} \to \hat{x}_{\infty} \qquad \frac{d\hat{h}}{d\hat{x}} = -\frac{E}{\rho(x)U}\left(\frac{\sigma_0}{3\mu_0 U}\right)^{1/3} \tag{20b}$$

$$\hat{x} \to \hat{x}_{\infty} \qquad \frac{d^2\hat{h}}{d\hat{x}^2} = 0 \tag{20c}$$

where $\hat{x}_{\infty} = \left(\frac{3\mu_0}{\sigma_0}\right)^{1/3} \frac{U^{4/3}\rho_{\infty} C_{pol,\infty}}{Q_{pol}} x_{\infty}$.

Also, at the matching point between the dynamic and steady meniscus regions, the matching condition that represents the dimensionless form of Eq. (15d) can be expressed as:

$$\hat{x} \to \hat{x}_{match} = \left(\frac{3\mu_0}{\sigma_0}\right)^{\frac{1}{3}} \frac{U^{\frac{4}{3}}\rho_{\infty} C_{pol,\infty}}{Q_{pol}} \sqrt{2}\left(\frac{\sigma_0}{\rho_0 g}\right)^{\frac{1}{2}} \tag{21a}$$

$$\frac{d^2\hat{h}}{d\hat{x}^2} \to \left(\frac{\sigma_0}{3\mu_0}\right)^{\frac{2}{3}} \frac{Q_{pol}}{U^{\frac{5}{3}}\rho_{\infty} C_{pol,\infty}} \sqrt{2}\left(\frac{\rho_0 g}{\sigma_0}\right)^{\frac{1}{2}} \tag{21b}$$

According to Eq. (21b), Q_{pol} can be expressed as

$$Q_{pol} = \left(\frac{3\mu_0}{\sigma_0}\right)^{2/3} U^{5/3}\rho_{\infty} C_{pol,\infty} \frac{1}{\sqrt{2}}\left(\frac{\sigma_0}{\rho_0 g}\right)^{1/2} \alpha \tag{22}$$

where

$$\alpha = \left.\frac{d^2\hat{h}}{d\hat{x}^2}\right|_{\hat{x}=\hat{x}_{match}} \tag{23}$$

α must be found from the numerical solution of Eq. (19) with boundary conditions given by Eqs. (20a)-(20c).

Combining Eqs. (16) and (22), an equation for the dimensionless variable $\hat{x}$ can be recast as

$$\hat{x} = \frac{\sqrt{2}\left(\frac{\rho_0 g}{\sigma_0}\right)^{1/2}}{\alpha\left(\frac{3\mu_0}{\sigma_0}U\right)^{1/3}}x \tag{24}$$

According to Eq. (15a) and Eq. (22), the thickness of the wet coating layer deposited during the process can be found as:

$$h_\infty = \frac{\alpha}{\sqrt{2}}\left(\frac{\sigma_0}{\rho_0 g}\right)^{1/2}\left(\frac{3\mu_0}{\sigma_0}U\right)^{2/3} \tag{25}$$

The mass conservation of carbon dioxide for an elementary volume between x and x+dx can be written as:

$$\rho(x)C_{co_2}(x)\int_0^{h(x)} u dy - \rho(x+dx)C_{co_2}(x+dx)\int_0^{h(x+dx)} u dy = E dx \tag{26}$$

The evaporation rate E can be obtained from the Hertz-Knudsen equation [25] as:

$$E = \frac{M_{co_2}\alpha_v \Delta P}{N_a^{1/2}\left(2\pi M_{co_2} kT\right)^{1/2}} \tag{27}$$

where k is the Boltzman constant ($1.3805\times10^{-23}\,J/K$), M_{co_2} is the molar mass of carbon dioxide (44 kg/kmol), N_a is the Avogadro constant ($6.02\times10^{26}\,kmol^{-1}$), T is the temperature, α_v is the evaporation coefficient, and ΔP is the pressure drop, which acts as

the driving force for evaporation. According to experimental measurements, α_v equals 5×10^{-5} for liquid carbon dioxide.

Utilizing the Taylor expansion, Eq. (26) can be recast as:

$$\frac{\partial\rho(x)}{\partial x}C_{co_2}(x)\int_0^{h(x)}udy+\rho(x)\frac{\partial C_{co_2}}{\partial x}\int_0^{h(x)}udy+\rho(x)C_{co_2}(x)\frac{\partial}{\partial x}\left[\int_0^{h(x)}udy\right]=-E(x) \qquad (28)$$

According to Eq. (13):

$$\int_0^{h(x)}udy=\frac{Q_{pol}}{\rho(x)C_{pol}(x)} \qquad (29)$$

Substituting Eq. (29) into Eq. (28), the following is obtained:

$$\frac{\partial\rho(x)}{\partial x}C_{co_2}(x)\frac{Q_{pol}}{\rho(x)C_{pol}}+\rho(x)\frac{\partial C_{co_2}}{\partial x}\frac{Q_{pol}}{\rho(x)C_{pol}}+\rho(x)C_{co_2}\frac{\partial}{\partial x}\left(\frac{Q_{pol}}{\rho(x)C_{pol}}\right)=-E(x) \qquad (30)$$

Equation (30) must be solved subject to the following boundary condition imposed at the border between the entrainment and static meniscus regions:

$$x\to x_{match}=\sqrt{2}\left(\frac{\sigma_0}{\rho_0 g}\right)^{1/2} \qquad C_{co_2}=C_0 \qquad (31)$$

where C_0 is the initial mass fraction of CO_2 (before evaporation started). Imposing this boundary condition implies that the effect of evaporation on polymer concentration in the solution when $x<x_{match}$ is negligible. This is a reasonable assumption because for $x<x_{match}$ the thickness of the meniscus is very large, and evaporation of carbon dioxide does not have significant effect on polymer and CO_2 concentrations.

Utilizing the same dimensionless variables, the dimensionless form of Eq. (30) can be recast as:

$$\frac{\partial C_{co_2}}{\partial \hat{x}} = -\frac{E(1-C_{co_2})^2}{\rho_\infty C_{pol,\infty} U\left(\frac{3\mu_0 U}{\sigma_0}\right)^{1/3}} \tag{32}$$

Equation (31) contains a yet undetermined parameter, $C_{pol,\infty}$, which is the polymer concentration at the height when the flow in the liquid film becomes hydrodynamically fully developed.

The appropriate boundary condition for Eq. (32) is

$$\hat{x}_{match} = \frac{2}{\alpha\left(\frac{3\mu_0}{\sigma_0} U\right)^{1/3}}, \qquad C_{co_2} = C_0 \tag{33}$$

It is convenient to recast Eq. (32) in terms of C_{pol}:

$$\frac{\partial C_{pol}}{\partial \hat{x}} = \frac{E C_{pol}^{\ 2}}{\rho_\infty C_{pol,\infty} U\left(\frac{3\mu_0 U}{\sigma_0}\right)^{1/3}} \tag{34a}$$

Corresponding boundary conditions for Eq. (34a) then are:

$$\hat{x}_{match} = \frac{2}{\alpha\left(\frac{3\mu_0}{\sigma_0} U\right)^{1/3}}, \qquad C_{pol} = 1 - C_0 \tag{34b}$$

$$\hat{x} = \hat{x}_\infty, \qquad C_{pol} = C_{pol,\infty} \tag{34c}$$

The analytical solution of Eq. (34a) with boundary condition (34b) can be obtained as:

$$C_{pol} = \frac{1}{\frac{1}{1-C_0} - \frac{E(\hat{x} - \hat{x}_{match})}{\rho_\infty C_{pol,\infty} U \left(\frac{3\mu_0}{\sigma_0} U \right)^{1/3}}} \tag{35}$$

Substituting Eq. (34c) into Eq. (35), the following quadratic equation for $C_{pol,\infty}$ is obtained:

$$C_{pol,\infty} = \frac{1}{\frac{1}{1-C_0} - \frac{E(\hat{x}_\infty - \hat{x}_{match})}{\rho_\infty C_{pol,\infty} U \left(\frac{3\mu_0}{\sigma_0} U \right)^{1/3}}} \tag{36}$$

where $\rho_\infty = \rho_{pol} C_{pol,\infty} + \rho_{CO_2} C_{CO_2,\infty} = \rho_{pol} C_{pol,\infty} + \rho_{CO_2} (1 - C_{pol,\infty})$.

The solution of Eq. (36) is

$$C_{pol,\infty} = \frac{-B + \sqrt{B^2 + 4AC}}{2A} \tag{37}$$

where

$$A = (\rho_{pol} - \rho_{CO_2}) U \left(\frac{3\mu_0}{\sigma_0} U \right)^{1/3} \tag{38a}$$

$$B = \left[\rho_{CO_2} - (1 - C_0)(\rho_{pol} - \rho_{CO_2}) \right] U \left(\frac{3\mu_0}{\sigma_0} U \right)^{1/3} \tag{38b}$$

and

$$C = (1 - C_0)\left[E(\hat{x}_\infty - \hat{x}_{match}) + \rho_{CO_2} U \left(\frac{3\mu_0}{\sigma_0} U \right)^{1/3} \right]. \qquad (38c)$$

If no evaporation is considered during dip coating process, i.e. E = 0, Eq. (19) can be simplified as

$$\frac{d^3\hat{h}}{d\hat{x}^3} - \frac{1-\hat{h}}{\hat{h}^3} = 0 \qquad (39)$$

which is exactly the same as the original Landau and Levich's equation [10].

6.2.2 Numerical Procedure

The numerical procedure can be divided into three steps:

(1) Solve Eq. (35) to obtain the distribution of $C_{CO_2}(\hat{x})$.

(2) Utilizing the obtained distribution of $C_{CO_2}(\hat{x})$, calculate $C_{pol}(\hat{x})$, $\mu(\hat{x})$, and $\sigma(\hat{x})$, substitute them into Eq. (19), and then solve this equation to obtain $\hat{h}(\hat{x})$.

(3) Compute α according to Eq. (23) and evaluate whether the convergence criterion $\left|\alpha^{n+1} - \alpha^n\right| \le 5\times10^{-8}$ is satisfied. If it is not satisfied, return to step (1) and iterate until convergence.

When solving Eq. (19), the numerical integration may lose stability near the remote point $\hat{x}_\infty$. To avoid this difficulty, Eq. (19) is linearized in the neighborhood of $\hat{x}_\infty$. When $\hat{x}$ is

close to $\hat{x}_\infty$, a Taylor expansion can be used for the dimensionless thickness of the layer, density of the fluid, and the concentration of polymer, respectively:

$$h = 1 + \varepsilon(x) \tag{40}$$

$$\rho(\hat{x}) = \rho_\infty(1 + \gamma(\hat{x})) \tag{41}$$

$$C_{pol}(\hat{x}) = C_{pol,\infty}(1 + \delta(\hat{x})) \tag{42}$$

where $\varepsilon(x)$ is the unknown small function, $\gamma(\hat{x}) = \frac{1}{\rho_\infty}\frac{\partial\rho(\hat{x})}{\partial\hat{x}}\bigg|_\infty(\hat{x} - \hat{x}_\infty)$, and $\delta(\hat{x}) = \frac{1}{C_{pol,\infty}}\frac{\partial C_{pol}(\hat{x})}{\partial\hat{x}}\bigg|_\infty(\hat{x} - \hat{x}_\infty)$.

Substituting Eqs. (40)-(42) into Eq. (19), and neglecting higher powers of small terms, Eq. (19) can be linearized as:

$$\frac{\mu_0}{\mu(\hat{x})}\frac{\rho(\hat{x})}{\rho_\infty}\frac{d}{d\hat{x}}\left(\frac{\sigma(\hat{x})}{\sigma_0}\frac{d^2\varepsilon}{d\hat{x}^2}\right) + \gamma + \varepsilon + \delta = 0 \tag{43}$$

Equation (43) must be solved subject to the following boundary conditions:

$$\hat{x} = \hat{x}_\infty \qquad \varepsilon = \varepsilon_0 \tag{44a}$$

$$\hat{x} = \hat{x}_\infty \qquad \frac{d\varepsilon}{d\hat{x}} = 0 \tag{44b}$$

and

$$\hat{x} = \hat{x}_\infty \qquad \frac{d^2\varepsilon}{d\hat{x}^2} = 0 \tag{44c}$$

where ε_0 is a small positive number (of the order of 10^{-10}) utilized to avoid the trivial solution.

After linearization, it is possible to investigate the behavior of the solution near $\hat{x}_\infty$ in detail.

The linearized equation, Eq. (43), can be solved analytically if it is assumed that the properties of the polymer solution are the same as those of liquid carbon dioxide. In this case, Eq. (43) can be simplified as:

$$\frac{d^3\varepsilon}{d\hat{x}^3} + \varepsilon + \delta = 0 \tag{45}$$

which must be solved subject to boundary conditions given by Eqs. (44a)-(44c). Since the solution for $C_{pol}(\hat{x})$ is given by Eq. (35), the analytical solution of Eq. (45) can be obtained as:

$$\varepsilon(\hat{x}) = -D(\hat{x} - \hat{x}_\infty) + c_0 \exp(\hat{x}_\infty - \hat{x}) + c_1 \exp\left(\frac{\hat{x} - \hat{x}_\infty}{2}\right)\cos\left(\frac{\sqrt{3}}{2}(\hat{x} - \hat{x}_\infty)\right)$$

$$+ c_2 \exp\left(\frac{\hat{x} - \hat{x}_\infty}{2}\right)\sin\left(\frac{\sqrt{3}}{2}(\hat{x} - \hat{x}_\infty)\right) \tag{46}$$

where

$$D = \frac{E}{\rho_\infty C_{pol,\infty} U\left(\frac{3\mu_0}{\sigma_0}U\right)^{1/3}} \tag{47a}$$

$$c_0 = \frac{\varepsilon_0}{3} - \frac{D}{3} \tag{47b}$$

$$c_1 = \frac{3\varepsilon_0}{3} + \frac{D}{3} \tag{47c}$$

and

$$c_2 = \frac{\sqrt{3}\varepsilon_0}{3} \tag{47d}$$

The polymer considered in this chapter is Fomblin® Z-DOL 2000. The properties used in the computations are given in Table 2.

Properties	$\rho(kg/m^3)$	$\sigma(N/m)$	$\mu(Pa\ S)$
CO_2	703	0.69×10^{-3}	15.02×10^{-6}
Fomblin® Z-DOL 2000	1810	2.4×10^{-2}	0.15385

Table 2 Physical properties of carbon dioxide and polymer

6.3 RESULTS AND DISCUSSION

A number of computations are performed by utilizing two different models for the surface tension of the solution. For the linear model the surface tension is computed according to Eq. (9c). The second model assumes that surface tension of the solution remains constant equal to that of pure liquid carbon dioxide. Figures 40-42 are computed for the initial polymer concentration of 0.61 wt pct, withdrawal velocity of 1.5 mm/s, and parameter ψ of 4×10^3.

Figure 40a displays a comparison of the free surface profiles computed for different evaporation driving forces (ΔP) between the system pressure and thermodynamic pressure at the liquid/gas interface. The pressure difference drives the evaporation and for relatively small values of evaporation rate is linearly proportional to ΔP, as given by Eq. (27). The case of $\Delta P = 0$ corresponds to no evaporation from the free surface. Free surface profiles computed utilizing the same model for surface tension of the solution (either linear or constant) exhibit larger curvature near x_∞ for larger evaporation rate (larger ΔP) than for the case of no evaporation ($\Delta P = 0$). For the curves computed assuming no evaporation the thickness of the layer at x_∞ is larger. Comparing the curves computed utilizing different models of surface tension, it can be seen that the linear model predicts larger dynamic meniscus region than the constant surface tension model. Figure 40b displays the polymer concentration distribution along the plate. These computation distributions correspond to the free surface profiles displayed in Fig. 40a. When there is no evaporation ($\Delta P = 0$), the polymer concentration does not change along the height of the plate, as expected. For the case with evaporation, the polymer concentration increases along the height of the plate. The rate of polymer concentration increase becomes large as the polymer layer gets thinner. This is because according to Eq. (27) for constant ΔP the evaporation rate from the unit surface is constant, but the volume of the solution is smaller if the layer thickness is smaller.

Figure 41 depicts a comparison of theoretical predictions of the effect of the evaporation driving force ΔP on dry film thickness with experimental data. The numerical predictions show that the dry film thickness depends almost linearly on the pressure drop no matter which model for the solution surface tension is utilized. The theoretical predictions agree

well with experimental results, except for large values of ΔP. The discrepancy can be explained by a number of different factors. First, in computations a constant pressure drop is assumed during the whole process, which results in a constant evaporation rate. However, during the experiment, only the system pressure is controlled and kept constant. The thermodynamic pressure at the liquid/gas interface may change because of the interface cooling during evaporation. This may result in the failure of constant ΔP assumption for larger evaporation rates. Second, the evaporation rate is related to ΔP by the Hertz-Knudsen equation (Eq. (27)), which utilizes a constant value of α_v. The assumption that α_v is constant may fail for large values of ΔP.

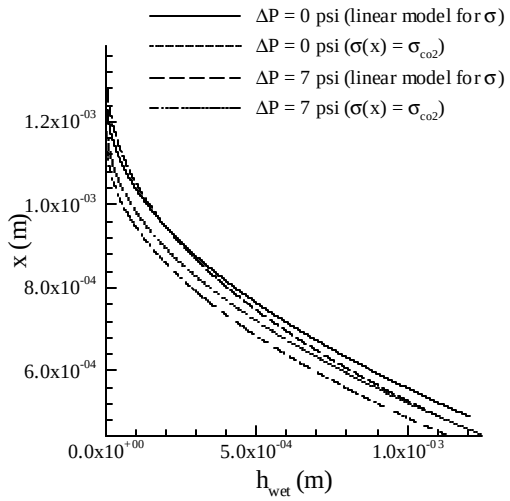

Figure 40a

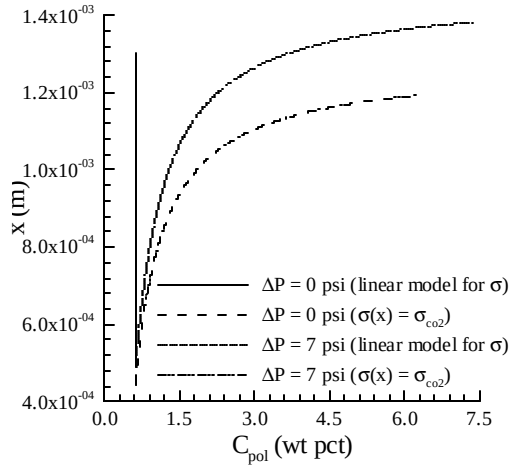

Figure 40b

Figure 40 (a) Comparison of free surface profiles and (b) polymer concentration distributions for different evaporation rate

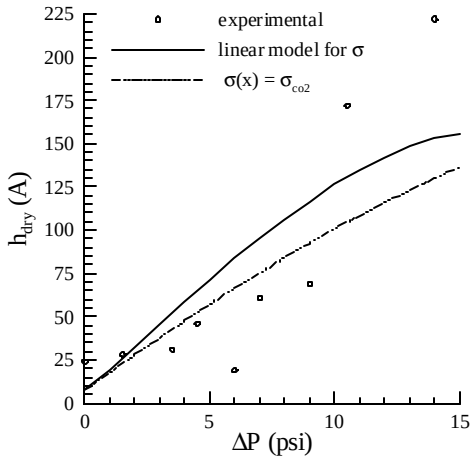

Figure 41 Effect of the evaporation driving force on dry film thickness

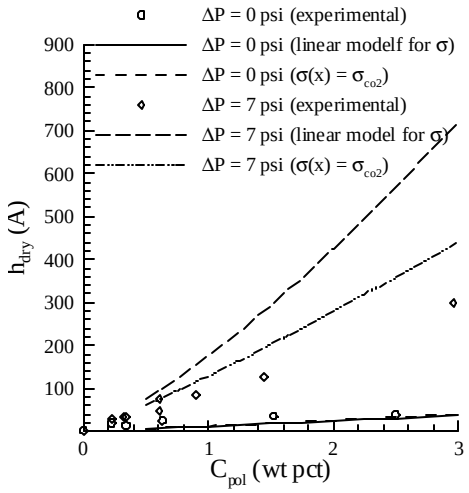

Figure 42 Effect of initial polymer concentration on dry film thickness

Figures 42 shows theoretical predictions of the effect of initial polymer concentration on the dry layer thickness and their comparison with experimental data. Computations are

performed for two different evaporation rates. It can be observed that the dry layer thickness increases with an increase of the initial polymer concentration. The numerical results are in good agreement with experimental data. Also, the initial polymer concentration has heavier effect on the layer thickness if evaporation occurs. Theoretical predictions agree well with experimental data obtained by Novick et al. [26] if constant surface tension model is utilized. However, current theory slightly but consistently overpredicts the dry film thickness even for the constant surface tension model. This can be attributed to neglecting the cooling effect by evaporation from the free surface.

The dependence of the dry film thickness on the withdrawal velocity is displayed in Fig. 43. These computations are performed assuming that the solution surface tension equals to that of carbon dioxide, the pressure difference is $\Delta P = 3$ psi, and the initial polymer concentration is 0.51 wt pct. Two cases are computed: (1) the parameter ψ is kept constant, equal to 4×10^{3}; (2) the parameter ψ changes with the withdrawal velocity, as $\log\psi = 694.431U_w + 2.829$. Physically, the second case is more realistic because there are experimental indications that the size of the meniscus region, h_{match}, depends on the capillary number, $Ca = \frac{\mu U_w}{\sigma}$. The numerical predictions obtained by assuming constant ψ show that the dry film thickness decreases with an increase of withdrawal velocity, which contradicts experimental results. This is obviously because the parameter ψ depends on the withdrawal velocity. The numerical prediction obtained by utilizing variable ψ agrees very well with experimental data.

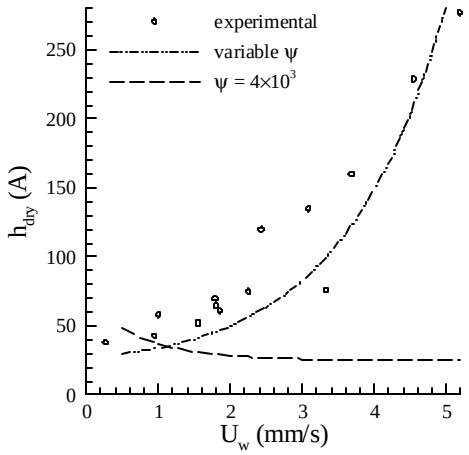

Figure 43 Dependence of dry film thickness on withdrawal velocity

6.4 CONCLUSIONS

The major novel feature of the theory developed in this chapter is accounting for the evaporation from the free surface. Because of the physical properties of carbon dioxide, accounting for evaporation is crucial to obtain reliable predictions of the film thickness deposited in this process. This investigation shows that the dry film thickness increases with the increase of evaporation rate and with the increase of initial solute concentration. The initial solute concentration has larger effect on film thickness when evaporation is accounted for than when it is neglected. Numerical predictions agree well with experimental results.

REFERENCES

1. Spiers, R.P., Subbaraman, C.V., and Wilkinson, W.L., Free coating of a Newtonian liquid onto a vertical surface, *Chemical Engineering Science*, 29:389-396, 1974

2. Kistler, S. and Schweizer, P.M., *Liquid Film Coating*, 1ed. Chapman and Hall: London, 1973.

3. Yeckel, A., Tools for parameter studies in fluid dynamics, *International Journal for Numerical Methods in Fluids*, 28:1199-1216, 1998

4. Deryagin, B.M. and Levi, S.M., *Film Coating Theory*, New York: The Focal Press, 1964

5. Scriven, L.E. and Suszynski, W.J., Take a closer look at coating problems, *Chemical Engineering Progress*, 86(9):24-29, 1990

6. Tallmadge, J.A. and Gutfinger, C., Entrainment of liquid films drainage, withdrawal, and removal, *Industrial and Engineering Chemistry*, 59(11):19-35, 1967

7. Tallmadge, J.A. and Lee, C.Y., Dynamic meniscus profiles in free coating III, predictions based on two dimensional flow fields, *AIChE Journal*, 20(6):1079-1086, 1974

8. Scriven, L.E., Physics and applications of dip coating and spin coating, *Better Ceramics through Chemistry III*, C.J. Brinker and D.E. Clark, Editors, Materials Research Society: Pittsburgh. pp. 717-729, 1988

9. Gellman, A.J., Lubricants and overcoats for magnetic storage media, *Current Opinion in Colloid and Interface Science*, 3:368-372, 1998

10. Landau, L. and Levich, B., Dragging of a liquid by a moving plate, *ACTA PHYSICOCHIMIC URSS.*, 17:42-54, 1942

11. Cerro, R.L. and Scriven, L.E., Rapid free surface film flows: an integral approach, *Industrial and Engineering Chemistry Fundamentals*, 19(1):40-50, 1980

12. Carvalho, M.S. and Scriven, L.E., Multiple states of a viscous free surface flow: transition from pre-metered to a metering inflow, *International Journal for Numerical Methods in Fluids*, 24:813-831, 1997

13. Higgins, B.G. and Scriven, L.E., Interfacial shape and evolution equations for liquid films and other viscocapillary flows, *Industrial and Engineering Chemistry Fundamentals*, 18(3):208-215, 1979

14. Schunk, P.R. and Rao, R.R., Finite element analysis of multicomponent two-phase flows with interphase mass and momentum transport, *International Journal for Numerical Methods in Fluids*, 19:821-842, 1994

15. Westerberg, K.W., McClelland, M.A., and Finlayson, B.A., Finite element analysis of flow, heat transfer, and free interfaces in an electron-beam vaporization system for metals, *International Journal for Numerical Methods in Fluids*, 26:637-655, 1998

16. Verros, G.D. and Malamataris, N.A., Finite element analysis of polymeric membrane and coating formation by solvent evaporation, *Computational Mechanics*, 27:332-340, 2001

17. Song, B., Inaba, H., Horibe, A., and Ozaki, K., Heat, mass and momentum transfer of a water film flowing down a tilted plate Exposed to solar irradiation, *International Journal of Thermal Sciences*, 38(5):384-397

18. Lee, C.Y. and Tallmadge, J.A., Dynamic meniscus profiles in free coating III predictions based on two-dimensional flow fields, *AIChE Journal*, 20(6):1079-1086, 1974

19. Hurd, A.J. and Brinker, C.J., Ellipsometric imaging of drying sol-gel films, In *Better Ceramics Through Chemistry III*, eds Brinker, J.C., Clark, D.E., and Ulrich, D.R., Materials Research Society, Pittsburgh, pp731-742, 1988

20. Hurd, A.J. and Brinker, C.J., Sol-gel film formation by dip coating, In *Better Ceramics Through Chemistry IV*, eds Zelinski, B.J.J., Brinker, C.J., Clark, D.E., and Ulrich, D.R., Materials Research Society, Pittsburgh. pp.575-581, 1990

21. Schunk, P.R., Hurd, A.J., and Brinker, C.J., Free-meniscus coating processes, In *Liquid Film Coating*, eds Kistler, S.F. and Schweizer, P.M., Chapman & Hall, London, pp. 673-708, 1997

22. Adamson, A.W., *Physical Chemistry of Surfaces, Fifth Edition*, John Wiley and Sons, Inc., New York, 1990

23. Hurd, A.J., Evaporation and surface tension effects in dip doating, *The Colloid Chemistry of Silica*, 234:433-450, 1994

24. Lee, C.Y. and Tallmadge, J.A., Description of meniscus profiles in coating II-analysis expression, *AIChE Journal*, 19(2):403-407, 1973

25. Maissel, L. and Glang, R., *Handbook of Thin Film Technology*, McGraw-Hill Book Company, New York, 1970

26. Novick, Brian J., Free meniscus coatings from liquid carbon dioxide, Ph. D. proposal, NCSU, 2000

7 CONCLUSIONS

In this dissertation transport phenomena in three processes that involve interfaces are investigated. These processes include forced convection in composite porous/fluid domains, solidification of binary alloys during which the mushy region appears, and meniscus formation in dip coating processing. Different theoretical and numerical approaches are utilized in modeling these processes.

7.1 REMARKS ON FORCED CONVECTION IN COMPOSITE POROUS/FLUID DOMAINS

Convection in composite domains partly filled with a homogeneous (clear) fluid and partly with a fluid saturated porous medium is of permanent interest to researchers because of its wide relevance to engineering applications. Starting from the nineteenth century, a considerable amount of work has been done in the field of porous media, when multiple theories have been developed, and different approaches have been suggested. In this dissertation the validity of the single-domain approach is investigated by comparing the numerical and exact solutions for forced convection flow in a composite porous/fluid channel. It is found that utilization of this approach results in implicitly imposing the continuity conditions for filtration velocity and its first order derivative with respect to the transverse coordinate at the interface. This implies that this approach is applicable to the fluid

flow problems in composite configurations only if there is no jump in the shear stress at the interface and if the effective viscosity of the porous medium is equal to the fluid viscosity.

An attempt to analytically solve a fully developed Couette flow problem in a composite porous/fluid channel is conducted by utilizing the boundary layer approximation. In the porous region the momentum transport is described by the Brinkman-Forchheimer-extended Darcy equation and the thermal dispersion along the transverse direction is taken into account in modeling energy transport. The results obtained predict a discontinuity in the Nusselt number when certain parameters, such as the heat flux ratio at the upper and lower plates, are varied.

A numerical simulation of forced convection in a circular porous/fluid duct is presented because it is currently impossible to obtain analytical solution for this problem. It shows that the Nusselt number increases when increasing Reynolds and Darcy numbers, while decreases when increasing the Forchheimer coefficient.

7.2 REMARKS ON SOLIDIFICATION OF BINARY ALLOYS

Microporosity formation and solute redistribution are two important phenomena present in solidification of binary alloys, more specifically, in the mushy region. Most of the previous work in this area treated the mushy zone as a two-phase mixture consisting of only solid and liquid phases. This approach neglects pore nucleation and growth in the mushy zone. Previous literature did not consider in detail the effect of microporosity formation on solute

transport. This work presents a three-phase model to describe the mushy zone as consisting of liquid, solid, and gas phases. The Scheil and lever rules are utilized to describe solute transport at the local scale. The physical aspects of microporosity formation and macrosegregation are analyzed based on numerical investigations. Parametric analyses of the factors influencing microporosity formation are performed. It is found that increasing the external pressure, decreasing gravitational acceleration, and utilizing vacuum melting are efficient ways to control microporosity formation during this process. The possibility of extending this technology to extraterrestrial surfaces and microgravity environment is also investigated.

7.3 REMARKS ON DIP COATING PROCESS

Dip coating with carbon dioxide as solvent is a very new technology developed in recent years. This technology is of great interest to industry. This interest originates from the physical properties of carbon dioxide as well as its friendliness to the environment. Accounting for evaporation is crucial in modeling this process because carbon dioxide is highly evaporable. A mathematical model based on the extension of the classical free meniscus theory is developed. Several factors affecting the final film thickness such as evaporation rate, initial solution concentration, and withdrawal velocity, are investigated. The dry film thickness is found to increase with the increase of evaporation rate and initial solute concentration. Comparisons between experimental data and numerical results show good

agreement between them and suggest that further studies are needed to take into account the effect of gravity. Also, evaporation rate given by currently available experimental data is the average one and assumed to be uniform at any height. However, there is experimental evidence that in reality it deviates from the uniformity. Further studies accounting for evaporation rate should take into account the dependence of evaporation rate on the position along the wafer.